Multifractal Objective Analysis, Rain and Clouds

by

Yves Tessier

A thesis submitted to the Faculty of Graduate Studies and Research in partial fulfillment of the requirements for the degree of Doctor of Philosophy

Department of physics

McGill University

Montréal, Canada

April 1993

ISBN 0-315-91670-2

Abstract

The study of rain and clouds, even after centuries of research, is still a subject whose theoretical basis is obscure. A major cause of this problem is the extreme variability. The multiplicative cascade models employed in the study of turbulence lead to fields presenting the desired variability over wide range of scales. The fields produced with these models have scale invariant properties expressed by a function specifying the way each statistical moment is transformed from one scale to the other; they are multifractal. It was proposed to consider rain and clouds as turbulent fields, thus providing a physical basis to statistical modeling of these fields. During this work, we wanted to empirically establish the applicability of these models. We established the range of scales where scale invariance is observed, we determined the transformation functions and established the limits of the model for various fields related to atmospheric water.

This verification is further complicated by the inhomogeneity of the measuring networks employed to gather data. In fact, the positions of landmasses, topography and economic constraints have resulted in networks which are not distributed on regular grids (as it might seem desirable) but on the contrary which presents holes at all scales. In fact, it has been shown that such networks are fractals. Rather, we will consider the station density as a multifractal. Multifractal fields analyzed by multifractal networks, this brings us to review the problem of removing the effect of the network from the measured data (the problem of Objective Analysis). The method that we propose (Multifractal Objective Analysis) replaces the homogeneity and regularity hypothesis more or less implicit in usual methods like Kriging by inhomogeneity and scaling hypothesis. It is then possible to develop corrections which allow us to study the multifractal properties of the analyzed field from the measured field.

Résumé

L'étude de la pluie et des nuages demeure malgré des siècles de recherches, un des domaines que la science a des difficultés à cerner. Une cause majeure de ce problème est l'extrême variabilité des phénomènes physiques impliqués. Les modèles de cascade multiplicative employé pour l'étude de la turbulence conduisent à des champs présentant la variabilité désirée. Les champs produits par ces modèles ont des propriétés d'invariance d'échelles qui sont exprimés par une fonction spécifiant la façon dont chaque moment statistique se transforme d'une échelle à l'autre; c'est-à-dire qu'il sont multifractals. Il fut proposé de considérer la pluie et les nuages comme des champs turbulents, ce qui fournit une base physique à la modélisation statistique de ces champs. Au cours de nos travaux nous avons voulus vérifier l'applicabilité de ces modèles. Nous avons entrepris d'établir la gamme d'échelles où se manifeste l'invariance, de déterminer les fonctions de transformations et d'établir les limites du modèle pour divers champs reliés à l'eau atmosphérique.

La poursuite de cette vérification est compliquée davantage par l'inhomogénéité des réseaux de mesures employés pour recueillir les données. En effet, la position des continents, la topographie de même que les contraintes économiques donne lieu à des réseaux qui loin d'être distribués sur des grilles régulières, comme il peut paraitre souhaitable, présentent plutot des lacunes à toutes les échelles. En fait, il a déja été démontré que de tels réseaux ont un comportement de type fractal. Nous considérons que la densité de stations de ce dernier est plutot multifractale. Des champs multifractals analysés par des réseaux multifractals, ceci nous amène à revoir le problème de retirer l'effet du réseau sur les mesures (le problème de l'analyse objective). La méthode que nous proposons (analyse objective multifractale) remplace les hypothèses d'homogénéité et de régularité plus ou moins implicites dans les méthodes usuelles comme le Kriging par les hypothèses d'inhomogénéité et d'invariance d'échelles. Il nous est alors possible de developper des corrections nous permettant d'étudier les propriétés multifractales du champ analysé à partir du champ mesuré.

Acknowledgments

A very special thanks to my thesis supervisor Dr Shaun Lovejoy from McGill physics department for understanding the chaotic evolution this work and its author have followed in the years it took to complete. He provided great inspiration for key issues. I am also grateful to Dr Daniel Schertzer (LMD, Univ. P&M Curie, Paris, France), who provided a lot of necessary questions... and answers that made this work possible.

My gratitude to Dr P. Hubert and Dr J.P. Carbonnel of the URA CNRS-1367, lab. de géologie appliquée, univ. P&M Curie, Paris (France), who allowed me to go beyond this thesis.

I acknowledge fruitful discussions with D. Lavallée, A. Davis, C. Hooge, G. Sarma, K. Pflug, G. Salvadori and F. Schmitt. Thanks also to P. Mercure and L. Jorgensen for helping me with the computer system.

I would like to thank F. Fabry and M. Duncan of the McGill radar for providing me some excellent data files and helping me understand them.

F. Francis and P. Silas contributed to the analysis of the satellite pictures. V. Sahakian, J. Wilson, F. Begin and S. Pecknold developed the multifractal simulation code and J.F. Malouin produced some figures, I am grateful to them.

I wish to express my deepest feelings to my parents Y. Perreault and C. Tessier for their support and affection that are so needed. The encouragements and patience of C. Fournier has been deeply appreciated.

Contribution to original knowledge

The main originality of this work is to explore several sources of information related to atmospheric water in search of properties invariant under a change of scale. When this thesis began virtually the only relevant analyses were monofractal (oriented toward geometrical sets). I am among the first to systematically investigate rain and cloud data for these properties. Now with the evolution of the theory and analysis methods more and more publications are appearing on the subject.

Another important contribution is that this thesis develop a new technique "multifractal objective analysis". This is a method for removing the bias introduced by the presence of an inhomogeneous (multifractal) network from the field measured by this network. Two major advances were required to develop this method. First, we considered the density of stations as a multifractal field, and demonstrated this empirically. This is better than considering the locations of stations as a fractal set of points because monofractals are a particular case of multifractals and for such fields a single fractal dimension is insufficient for their characterization. The second important point is to consider the measured field as the product of two multifractal fields (i.e. the density of stations and the analyzed field). It brings up the possibility of making statistical corrections on the measured field. I have thus replaced the assumptions of homogeneity and regularity implied by usual objective analysis methods such as Kriging by scaling assumptions. We also adapted many of the multifractal analysis techniques to the spherical geometry of the earth.

Using a significant number of satellite pictures from NOAA-9 AVHRR sensor I concentrated my study on the critical range of scales (1-512 km) where the standard model of atmospheric motions predicts a scaling break (≈10 km) due to a dimensional transition ("the mesoscale gap") between two and three dimensional regimes of turbulence. Since I observed no such break, this is a new and strong support of the alternative unified scaling model. I extended the range of scales of this study with some images from other sources (LANDSAT MSS and METEOSAT), so that an overall range of 160m to 4000 km was investigated with still no sign of a break. This analysis covered one of the widest range of scales explored to yet and was more systematic than any others that I know of.

We also provided the first reliable estimates of the universal scaling parameters α (the degree of multifractality) and C_1 (the sparseness of the mean) for cloud radiances. The methods previously used to make these estimations where not specifically designed for universal multifractal contrary to the new double trace moments technique used in this study. The new methodology results in a more direct estimate (linear instead of problematic non-linear regressions) and a greater accuracy. We also had a larger dataset to perform the estimates.

We performed the first real test of scaling and universality for radar reflectivities. We have to mention however that some indications of scaling behavior and other preliminary analyses showing the possible compatibility with universal multifractals were presented in the past. We are the first to attempt an estimate of the universal multifractal parameters for radar reflectivities (from a scanning and a fixed vertical radar) in the horizontal and vertical directions as well as along the time axis. We were also the first to invoke the semi-empirical Marshall-Palmer relation to explain the agreement between the estimated values of the parameter α for radar reflectivities and for daily rainfall accumulations from gages.

We provided the first evidence that the universal multifractal parameter α could be different in time and in space. This was observed for the rainfield and for radar reflectivity fields. In both cases for the temporal scaling we observed $\alpha \approx 0.5$ and for the spatial scaling we observed $\alpha \approx 1.4$. This shows that the generators of the cascade processes are qualitatively different in space and in time.

Table of Contents

List of Tables

List of Figures

Chapter I

Introduction

I.1 General Introduction

Strong non-linearities and wild variability have always been both basic geophysical problems. They have generally been postponed or ignored both because of the lack of conviction that they were important and due to the absence of adequate theoretical and numerical tools to face them. It is no longer possible to ignore these issues. The tools have undergone rapid development, they are called chaos, multifractals, self-organized criticality and many other names that are becoming increasingly familiar to scientists.

Rain and clouds are certainly among the most variable fields we experience in everyday life. It's very hard to describe the shape of a cloud because it is so irregular. In fact quite often when we see something with a very irregular shape we will tend to say it has a cloud shape. At the level of intuitive notions, if we look at cloud images, and there are no other reference object in the picture (such as a plane or some recognizable part of land) it is virtually impossible to estimate the size of the cloud, thus suggesting that some (statistical) symmetry principle must be obeyed when we change scales. The search for such a symmetry and its use is at the very basis of this thesis. One place to start such a search is certainly the basic Navier-Stokes equations governing atmospheric motions. It has been known for quite some years that this set of equations lacks of characteristic scales thus leading to scaling dynamics. Scaling or scale invariance indicates that some properties -- geometrical or statistical-- are preserved at different length scales. Transformation from one scale length to another will only involve scaling exponents. A simple illustration of scaling are sets, such as the Cantor set, characterized by a unique scaling exponent, its (mono)fractal dimension (see Mandelbrot [80]). However more complex fields will have in general their scaling properties characterized by a collection of scaling exponents, a dimension function or multifractal dimension.

The standard model of atmospheric dynamics (e.g., Monin [84]) divides the atmosphere into two fundamentally distinct regimes: a small scale three-dimensional turbulent regime and a large scale two-dimensional turbulent regime. Both regimes are scaling (scale invariant, power law spectra) and both are considered self-similar (the combination of scaling with statistical isotropy). Unlike turbulence in three dimensions, in two dimensions, vortex stretching is inhibited and vorticity is conserved. The standard model assumes that these different regimes are separated by a "mesoscale gap" whose scale is expected to be of the order of the scale height of the atmosphere ($\approx$10 km). The existence of the "gap" has been periodically questioned on empirical grounds since the late sixties. However, we believe that an equally significant source of doubt concerns its theoretical underpinnings that now appear to be quite ad hoc. This change in perception is possible due to the remarkable progress in scaling ideas that occurred during the 1980's and a better understanding of the nonlinear effects and strong variability.

According to this model both regimes of turbulence should be scaling but with different spectral slope (k^{-3} in 2D and $k^{-5/3}$ in 3D) and they should be separated by a sharp transition. This debate on the dimensionality of atmospheric turbulence took a new direction. Schertzer and Lovejoy [105] proposed a new "unified scaling" model in which the atmosphere is never isotropic (3-D) nor completely flat (2-D), but anisotropic and scaling throughout. During this period, scaling ideas were extended beyond the restrictive bounds of the fractal geometry of sets to directly deal with the multifractal statistics (and dynamics) of fields. Multifractals are increasingly understood as providing the natural framework for scale-invariant non-linear dynamics. Furthermore, due to the existence of stable attractive multifractal generators (Schertzer and Lovejoy [109, 111, 113, 115], Fan [31], Brax and Peschanski [11]) they provide attractive physical models. This implies that many of the details of the dynamics are irrelevant and lead to new and powerful multifractal simulation and analysis techniques.

Although these concepts are very attractive from a theoretical point they need extensive confrontation with real data. In the last few years such verification has gained interest in almost every field of geophysics. This thesis concentrates on the multiscaling properties of many fields related to atmospheric water: satellite pictures, radar reflectivity and ground rainfall accumulations. An attempt is made to cover the widest range of temporal and spatial scales. We determined the range of scales where scaling was observed in the available data, and established the multifractal properties and their limitations for the different fields. For the raingage accumulations, sensed by a global network we had to develop a new method to perform this analysis.

I.2 About Objective Analysis

The analysis of ground rainfall accumulations raises a problem that many geophysical disciplines are forced to deal with: the inhomogeneity of the measuring networks. The position of the stations is influenced by the position of landmasses, the topography and economic imperatives. Topography and landmasses distributions are among the first domains where fractals were recognized. All the nice images (in spite of their unrealistic monofractal nature) illustrating Mandelbrot's book [80]) showing impressive mountains imitations and the multifractal improvements of Wilson et al [137] are certainly a good example. It seems logical that geographic multifractality is reflected in the distribution of stations. Some attempts have been made in the past to characterize this sparseness by the fractal dimension of the set of points representing the physical location of the stations. This was the first time measuring network scaling properties were recognized. We will improve on this by considering that the density of stations is the basic field with multifractal properties.

The inhomogeneity of the measuring network certainly introduces bias in various estimates of the measured field. Considering this field as regular and representable by analytic functions leads us to reduce the problem of removing the bias to a simple problem of interpolation. Techniques for filling the holes in the data are called Objective Analysis. Various techniques were designed to perform this task: polynomial curve fitting, spline, nearest neighbor, Kriging etc... These methods did not consider that the network and the analyzed field have different dependencies on the resolution of the measurements. For many geophysical fields, such as rainfall, there is growing evidence that they are multifractal (in the case of rain and clouds a significant part of this thesis will be devoted to adding to this evidence). We addressed the problem of removing the network bias differently. The method proposed ("Multifractal Objective Analysis") replaces the assumptions of homogeneity and regularity (resolution independence) implicit in other methods by inhomogeneity and resolution dependencies. The network and the analyzed field have different dependence on the resolution and both fields have to be considered at the same time since the measured field is the product of the two. The technique we develop extracts the scaling properties of the analyzed multifractal field from the measured field.

I.3 Scaling of rain

In 1962, Lamperti [56] introduced the simplest scaling hypothesis under the name "semistable" (later renamed "self-similarity" by Mandelbrot and Van Ness in 1968 [77]). This hypothesis that is related to fractals could be defined for the rain rate as:

$$\Delta R(\lambda^{-1}\Delta x) \overset{d}{=} \lambda^{-H}\Delta R(\Delta x) \tag{1.1}$$

where the small scale difference $\Delta R(\lambda^{-1}\Delta x) = R(x_1 + \lambda^{-1}\Delta x) - R(x_1)$ and the large scale difference is $\Delta R(\Delta x) = R(x_2 + \Delta x) - R(x_2)$ where x_1 and x_2 are arbitrary, λ is a reduction ratio, and H is the (unique) scaling parameter, the equality $\overset{d}{=}$ means equality in probability distribution viz. $a \overset{d}{=} b$ if and only if $\Pr(a > q) = \Pr(b > q)$ for all q. When the process is a Brownian motion and the probability distribution is Gaussian $H = 1/2$. The previous findings by Hurst [50] of H = 0.7 in some river flow records raised the question of type of what type of probability distributions and processes were relevant in hydrology.

In 1981, Lovejoy [62] in relation with fractal[1] geometry (Mandelbrot, [78, 79]) hypothesized that simple scaling hold but with highly nongaussian probability distributions required to account for the intermittency of rain. He used probability distributions of radar rain data to test the simple scaling and the "fatness" of the probability tail. The term "fat tail" was introduced by Waymire [135] to indicate that due to the extreme variability of rain the probability distribution has algebraic tails instead of gaussian tails. The conclusion was that simple scaling was reasonably well respected in space with a value of $H \approx 0.5$. In time, estimates of the area integrated rainrate of isolated storms every five minute for 100 minutes also gave satisfactory results with $H \approx 0.7$.

Fat tailed distributions also implied that the probability of a rainfall fluctuation Δr exceeding a fixed threshold ΔR (generally expressed in mm/hr) for hyperbolic tail is given by:

$$\Pr(\Delta r > \Delta R) \approx \Delta R^{-q_D} \quad (\Delta R >> 1) \tag{1.2}$$

where the subscript D emphasizes the depence of the exponent q_D on the dimension of the space used for averaging (a point that we will develop further in chapter III). Various estimates of this exponent were performed. For example Segal [124] using 5-15 years time series of tipping bucket raingages records in Canada came to the conclusion that among the various functional forms he tested for 1 minute averages of rain rates greater than 3 mm/hr a power law provided the best fit with $q_D = 2.5 \pm 0.5$ (as shown in fig. 1-1). Ladoy et al [55] (fig. 1-2) using daily rain accumulations at Nîmes-Courbessac for 40 years observed hyperbolic behavior with $q_D \approx 2.6$. In multifractals, this hyperbolic behavior can now be associated with multifractal phase transitions. A point that we will develop later.

[1] For review textbook on fractal geometry consult Mandlebrot [80], Feder [32], Falconer [30] and Barsley [4].

Other early tests of scaling came from geometrical characterization of cloud fields (from radar and satellite). Typical analyses involved comparing the area and the perimeter of clouds defined as region exceeding a certain level of black body IR emission. Such analyses were performed by: Cahalan [14], Come [16], Lovejoy [63], Lovejoy et al [64], Lovejoy and Schertzer [65], Rhys and Waldvogel [101], Welch et al [136], Yano and Takeuchi [140]. An example of this type of analysis is shown in fig. 1-3. In these analyses the perimeter P was defined by regions exceeding a threshold. It was compared to the area of a cloudy region in a relation of the form $P \propto \left(\sqrt{A}\right)^{D}$ where D is the fractal dimension of the perimeter. Sometimes, the scaling was not too evident, or breaks in the scaling were inferred, and much variation was observed in the value of the dimension. Small databases, poorly adapted (e.g. monofractal) methods influenced these results. Most of these analyses where examined in Lovejoy and Schertzer [74] to build convincing evidence toward scaling of cloud radiances.

Geometric approaches have also been made on the fractal sets associated with thresholded time series of rain (Bocquillon and Moussa [9], Hubert and Carbonnel [45, 46, 47], Olsson et al. [90] and Sen et al. [125]). In all these analyses good scaling was observed but great variations in the value of the exponent D were found. The reason for this variation is that fields had to be converted to geometrical sets before any analysis could proceed and geometrical sets are characterized with only one dimension exponent (D). Multifractals are the proper framework for fields. In this approach, an infinity of exponents is needed (one for each moment of the field) thus the unique exponent D has to be replaced by a scaling function which tells how each statistical moment scales.

Scaling could also be searched for in Fourier space. The energy spectrum E(k). k being the modulus of the wavevector ($k = |\bar{k}|$) is of the form $|\bar{k}|^{-\beta}$ for statistically isotropic scaling fields, β is called the "spectral slope". Ladoy et al [55] found $\beta \approx 0.3$ with daily raingage accumulations for periods of 1 to 4 years at a station in Nîmes (shown in fig. 1-4). While Rodriguez-Iturbe et al [104] found $\beta \approx 1.3$ over periods of 1 minute to 2 hours with 15 seconds averaged rainrates. Using the log of radar reflectivity Crane [18] obtained $\beta \approx 5/3$ over the range of 1 minute to 2 hours. With (mono)fractals the exponent H is simply related to the spectral slope β by $\beta = 2H+1$ and the fractal dimension with $D = (5-\beta)/2$. This relation has often been used to evaluate the fractal dimension of field, but it does not hold for multifractals. For the more general multifractals, alternative relations will be exposed in the next chapter where relations between the scaling exponent for the second order moment, β and H will be given.

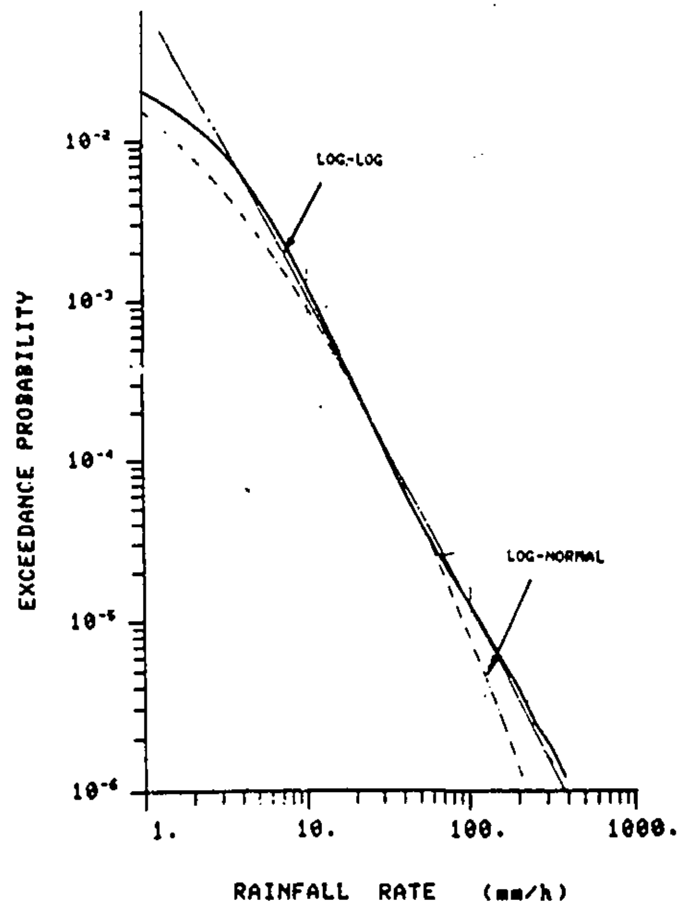

Figure 1-1: An example (from 10 years of tipping bucket raingage data at St. John, New Brunswick) of the extreme rainrate end of one minute resolution rainrate probability distributions from Segal [124]. Best fitting curve for the log-normal and the hyperbolic (log-log) distributions are shown.

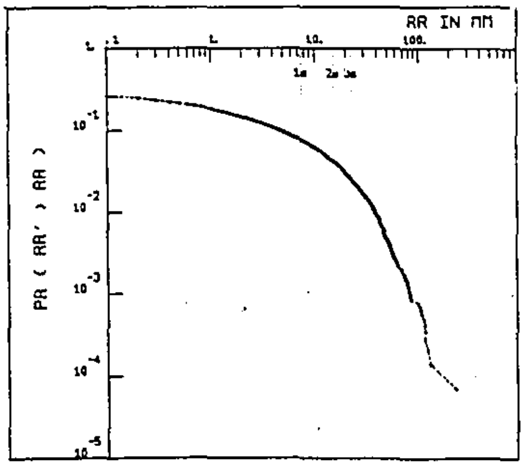

Figure 1-2: The probability ($\Pr(\Delta r > \Delta R)$) of a random (absolute) rain rate difference Δr, exceeding a fixed ΔR for daily rain accumulations at Nîmes-Courbessac (France) from 1949-1988 (14245 days). The tail is nearly straight with exponent $q_D \approx 3.5$. From Ladoy et al. [55].

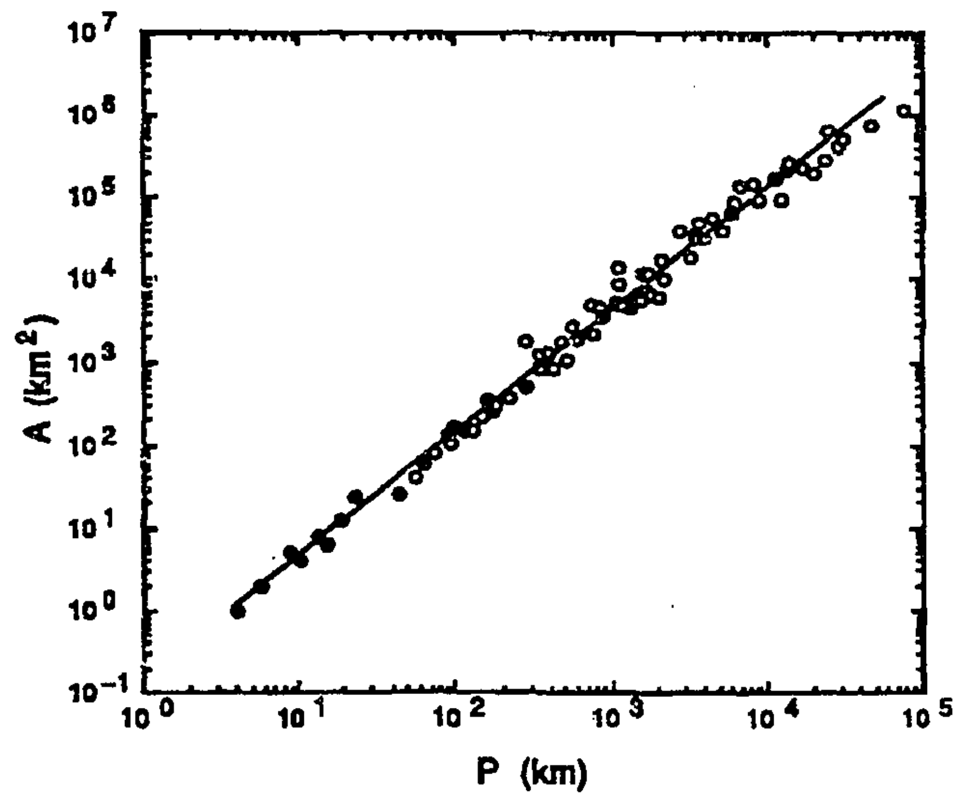

Figure 1-3: Area plotted against perimeter of rain and cloud areas determined from radar (filled circles) and satellite data (empty circles). From Lovejoy [63].

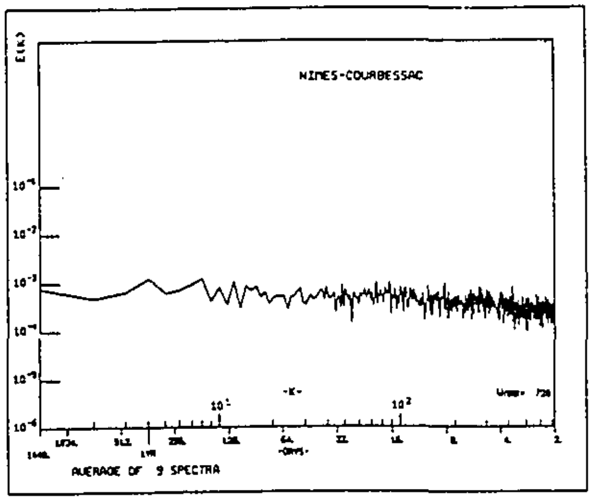

Figure 1-4: The average of six consecutive 4 year spectra of the daily rainfall accumulations at Nîmes-Courbessac. The annual peak is fairly weak, the scaling holds over most of the regime with slope (=-β)≈-0.3. There is no clear evidence for the "synoptic maximum" (i.e. a break at periods of a few weeks). From Ladoy et al [55].

I.4 Turbulent Cascades and Rain; beyond simple scaling

Since the intuition of Richardson, 1922 [103] and the first concrete model (Novikov and Stewart, 1964 [86]), many cascade models were elaborated to provide a phenomenological description of turbulence. These models are based on the following observations and hypotheses.

1) The dynamics are invariant under a change of scale over a wide range of scales. This comes from the Navier-Stokes equations for a range of scales between the energy injection (at large scale) and its dissipation (on scales typically of the order of 1 mm).

2) The existence of fluxes conserved by the non-linear dynamics such as the energy flux and the passive scalar flux in passive scalar clouds[2].

3) The interactions take place mainly between neighboring scales (the dynamic is local in Fourier space). This is also a property of Navier-Stokes equations.

---

[2] A passive scalar is a scalar quantity (e.g the concentration of pollutants) that does not influence the velocity field.

Taken together, these three properties are the basis of cascade models. In 1987, Schertzer and Lovejoy [109] proposed that rain and non-passive scalar clouds could share some basic scaling properties that could be modeled by the simpler but already complex turbulent cascade processes, thus providing a physical basis to stochastic modeling. Such models have the interesting property that in general they produce multifractal fields. Furthermore, in the same manner that gaussian noises are generally produced by a linear sum of random variables, the cascade processes generally produce universal multifractals by a non-linear mixing of scale invariant noises. The resulting fields belong to stable and attractive universality classes for which many of the details of the models are "washed out". The analysis and simulation of such fields are greatly simplified since only three parameters are needed to characterize the infinity of scaling exponents (e.g. the scaling function). We established the region of the scaling function that respects universality and determined the universal parameters for the different fields we studied.

I.5 Confronting models and experience

The direct determination of the spatial and/or temporal distribution of water in any of its phases in the atmosphere is difficult and limited to in situ measurements. Many of the current measurement difficulties could be overcome if we were able to model the extreme variability of the water in the atmosphere because then we would be able to infer and simulate what different (both remote and in situ) sensors would measure. For example, one could simulate the estimation of aerial rainfall from sparse raingage networks, and one could perform proper radiative transfer calculations to model (Davis et al [23]) what would be seen from a satellite at various wavelengths or what a weather radar would measure[3] (Duncan et al [27]). A primary goal of multifractal analysis is precisely to provide the information necessary to calibrate such models. Contrary to direct measurement of liquid water many of the fields dynamically coupled with the latter are relatively easy to measure.

[3] See Lovejoy and Schertzer [71, 72] for discussion over various fractal and multifractal effects on radar reflectivities.

This thesis investigates the multiscaling properties of some of these fields. The purpose of this work is to verify the existence of multiscaling properties, analyze them, find their regions of applicability and the limitations of the available data.

The next chapter presents new analyses of satellite cloud radiances which we believe are particularly strong endorsements of the unified scaling model. From the perspective of distinguishing 2D/3D from unified scaling model, it has several unique strengths:

-large samples of satellite pictures spanning wide range of scales are readily available.

-The pictures from NOAA-9 cover the critical range 1-512 km, i.e. much smaller to much larger than the ≈ 10 km scale height where 2D/3D break is expected. This analysis is supplemented by a more limited number of LANDSAT and METEOSAT images so that the overall range covered by this study is from 160m to 4000 km.

-The raw radiances are sampled on a near rectangular grid so that minimal reprocessing is required.

We then look at radar reflectivities which complement this study in many ways:

-Even though a narrower range of scale is investigated (≈100 m to 10 km) still minimal reprocessing is required since the raw reflectivities are analyzed.

-The interaction mechanism between the electromagnetic radiation emitted by a radar and the water vapor of clouds is different from the interaction of clouds with the incoming solar radiation that is reflected in the visible and infra-red portion of the spectra that sensed the satellites. Different scaling behavior will result.

-It is possible to separately study the scaling in the horizontal, in the vertical and along the time axis. This is not the case with satellite images (except with GOES, but with a temporal resolution of 1/2 hour).

Chapter 3 is devoted to the spatial distribution of daily global rainfall accumulations. It is the test case for the new multifractal objective analysis technique. This dataset has many special interests to us:

-It was gathered on one of the largest geophysical networks. It consists of nearly 8000 stations that reported daily rainfall accumulations in 1983.

-It covers the planet, so the largest earthly scales could be studied with this dataset. However it has the drawback of being distributed on a sphere, thus the method has to be adapted to the geometry of the situation.

Chapter II

Multifractal theory and Analyses of Remotely Sensed Atmospheric Water Fields

According to the unified scaling model, the dynamics are governed by anisotropic (differentially stratified and rotating) cascade processes yielding highly variable multifractal fields. Just as gaussian random variables are associated with (linear) sums of random variables, these (nonlinear) multiplicative processes are generically associated with (special) universal multifractals in which many of the details of the dynamics are irrelevant. In the first sections, we outline[1] these arguments in a widely accessible form to provide the context and motivation of this work. Next we test these ideas empirically with remotely sensed data. This is done using LANDSAT, NOAA-9, and METEOSAT satellite cloud radiances at visible, near infrared and thermal infrared wavelengths with length scales spanning the range ≈166m-4000 km, radar reflectivities of rain (in the vertical and time), and global daily rainfall accumulations. We apply spectral analysis as well as the new Double Trace Moment data analysis technique. In each case, rather than the sharp dimensional transition predicted by the standard model, we find the scaling to be relatively well respected right through the mesoscale. We then estimate the three fundamental universal multifractal exponents and go on to outline how these exponents (with the help of appropriate space-time transformations) can be used to make dynamic multifractal models.

[1]This summary follows closely Tessier et al [129].

II.1 Multifractal Phenomenology of atmospheric turbulence

II.1.1 Multifractal Processes

The multifractal processes discussed here were first developed as phenomenological models of turbulent cascades. In hydrodynamic turbulence the governing nonlinear dynamical ("Navier Stokes") equations have three properties which lead to the cascade phenomenology: a) scaling symmetry (invariance under dilations (zooms)), b) a quantity conserved by the cascade (energy fluxes from large to small scale), c) localness in Fourier space (this means that the dynamics are most effective between neighboring scales, direct transfer of energy from large to small scale structures is inefficient). Cascade models are relevant in the atmosphere in general and in rain and hydrology in particular since (as argued in Schertzer and Lovejoy [109]), although the full nonlinear partial differential equations governing the atmosphere will be more complex than those of hydrodynamic turbulence, they are nonetheless still likely to respect properties a, b, c. To understand this, consider the simplest strongly nonlinear model of rain, the passive scalar model, which ignores the effect of rain on the dynamics and assumes that cloud water is simply advected with the wind. Virtually the same assumptions are used in numerical weather prediction models. In these models of passive advection of water by a velocity field (v) the dynamical equations conserve the flux of energy and of scalar variance (with respective densities ε and χ). The injection of these quantities at large scale is assumed constant (or at least to be a stationary random process) and then there is transfer of these to smaller scales (hence cascade). By considering statistically stationary fields of these quantities, dimensional arguments lead to the laws of Kolmogorov [53], Obukhov [87] and Corrsin [17]

$$\begin{aligned} E_v(k) &\approx \varepsilon^{2/3} k^{-5/3} \\ E_p(k) &\approx \xi^{2/3} k^{-5/3} \end{aligned} \tag{2.1}$$

where $\xi \approx \chi^{3/2}\varepsilon^{-1/2}$, and $E_v(k)$ and $E_\rho(k)$are the power spectra for the velocity and passive scalar fields, respectively and k is a wavenumber ($k \approx 1/\ell$). Here ξ is the flux resulting from the nonlinear interactions of the velocity and water. In real space the equivalent relations are:

$$\begin{aligned} \Delta V(\ell) &\approx \varepsilon^{1/3}\ell^{1/3} \\ \Delta\rho(\ell) &\approx \xi^{1/3}\ell^{1/3} \end{aligned} \tag{2.2}$$

where $\Delta v(\ell)$ and $\Delta\rho(\ell)$ are the characteristic fluctuations of the fields v and ρ at the scale ℓ. These equations should be understood statistically. A straightforward interpretation useful in modeling is to view the scaling $\ell^{1/3}$ as a power law filter ($k^{-1/3}$) of $\varepsilon^{1/3}$ (Schertzer and Lovejoy [109], Wilson et al [138]). These equations are the result of treating passive scalar advection as a nonlinearly coupled cascade process (for ξ and ε). As we add in more and more coupled equations to account for other interacting fields (such as radiation or water in its various phases), more and more coupled cascades will be obtained. The turbulent and multifractal results presented here continue to be valid.

There are now a whole series of such phenomenological models: the "pulse in pulse" model (Novikov and Stewart [86]), the "lognormal" model (Kolmogorov [54], Obukhov [89], Yaglom [139]), "weighted curdling" (Mandelbrot [78]), the "β model" (Frisch et al. ([33]), "the α model" (Schertzer and Lovejoy [105]), the "random β model" (Benzi et al [7]), the "p model" (Meneveau and Sreenivasan [83]) and the "continuous" and "universal" cascade models (Schertzer and Lovejoy [109]). It is now clear that scale invariant multiplicative processes generically give rise to multifractals and -- due to the existence of stable and attractive multifractal generators -- to universal multifractals in which many of the details of the dynamics are unimportant. These results are important in hydrology and geophysics since they show that while geometrical fractals are sufficient to study many aspects of scaling sets, that multifractals (with their statistical exponents) provide the general framework for scaling fields (measures).

In contrast to the well-studied case of hydrodynamic turbulence, the dynamical equations responsible for the distribution of rain and cloud radiances are not known[2]; the best we can do at present is to speculate on the appropriate fundamental dynamical quantities analogous to ξ. Since a priori, there is no obvious reason why the rain rate or cloud radiance fields themselves should be conservative, in analogy with turbulence, we introduce a fundamental field φ_λ which has the conservation property $<\varphi_\lambda>$ = constant (independent of scale). The observable (non conserved) rainfall (or cloud radiance) fluctuations (ΔR_λ) are then given by:

$$\Delta R_\lambda \approx \varphi_\lambda^a \lambda^{-H} \tag{2.3}$$

Since we have as yet no proper dynamical theory for rain or cloud radiances, we do not know the appropriate fields φ_λ nor the corresponding values of *a*. In the following discussion, we therefore make the simplifying assumption that a = 1 (changing the value of a corresponds essentially to changing the parameter C_1; see below). With this in mind, the scaling parameter H has a straightforward interpretation: it specifies how far the measured field R is from the conserved field φ : $\langle|\Delta R_\lambda|\rangle \approx \lambda^{-H}$. H therefore specifies the exponent of the power law filter (the order of fractional integration) required to obtain R from φ.

II.1.2 Some properties of φ_λ

We now focus our attention on the conserved quantity φ_λ. Early scaling ideas were associated with additive (linear) processes, and unique scaling exponents H (which --only in these special cases-- were related to unique fractal dimensions by simple formulae). The properties of φ_λ were quite straightforward, and were usually understood implicitly.

[2]We exclude here the essentially ad hoc parametrizations employed by numerical cloud and weather models.

Turning our attention to (nonlinear) multiplicative processes we can consider some of the properties of φ_λ which will generically result from cascades. Fig. 2-1a,b illustrates such a discrete multiplicative process for φ_λ: a large structure of characteristic length l_0 with an initial uniform density φ_0, is broken up (via non-linear interactions with other structures or through internal instability) into smaller sub-structures of characteristic length $l_1 = l_0/\lambda_0$ ($\lambda_0 = 2$ is the scale ratio between two construction steps in this particular example), multiplicatively modulating by a (random) factor the flux on each sub-structure. When the process is repeated (the overall ratio λ is increased; after n iterations, $\lambda=\lambda_0^n$, $l_n=l_0/\lambda_0^n$) larger and larger values of φ_λ appear, concentrated on smaller and smaller volumes. In the small scale limit, the result is a highly intermittent multifractal measure with singularities of all orders γ distributed on fractal sets with codimension $c(\gamma)$ (Schertzer and Lovejoy [109], see the schematic illustration, fig. 2-2). In the range of scales λ between the injection and dissipation of Energy (i.e. the scaling regime) the measures on φ_λ have the property:

$$\Pr(\varphi_\lambda \geq \lambda^\gamma) \approx \lambda^{-c(\gamma)} \tag{2.4}$$

(equality is within slowly varying functions of λ such as logs). $c(\gamma)$ is therefore the scaling exponent of the probability distribution. However, when the process is observed on a low dimensional cut of dimension D (such as the D=1 dimensional simulation shown in fig. 2-2) it can often be given a simple geometric interpretation. When $D>c(\gamma)$, we may introduce the (positive) dimension function $D(\gamma)=D-c(\gamma)$ which is then the fractal dimension of the set with singularities γ.

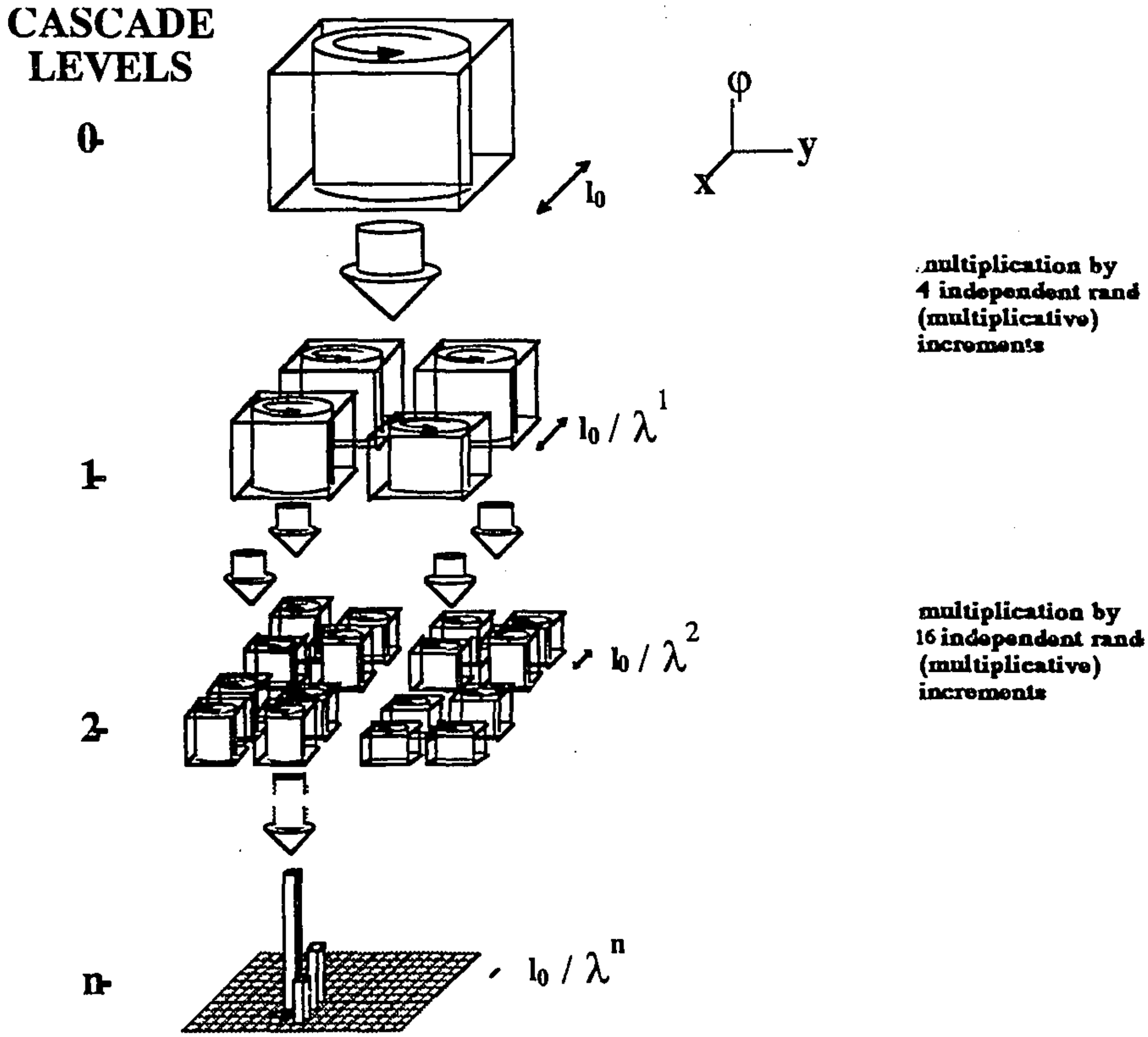

Figure 2-1a: A schematic diagram showing a two-dimensional cascade process at different levels of its construction to smaller scales. Each eddy is broken up into four sub-eddies, transferring a part or all its energy flux to the sub-eddies. In this process the flux of the field at large scales multiplicatively modulates the various fluxes at smaller scales, the mechanism of flux redistribution is repeated at each cascade step (self similarity). Reproduced from Lavallée [58].

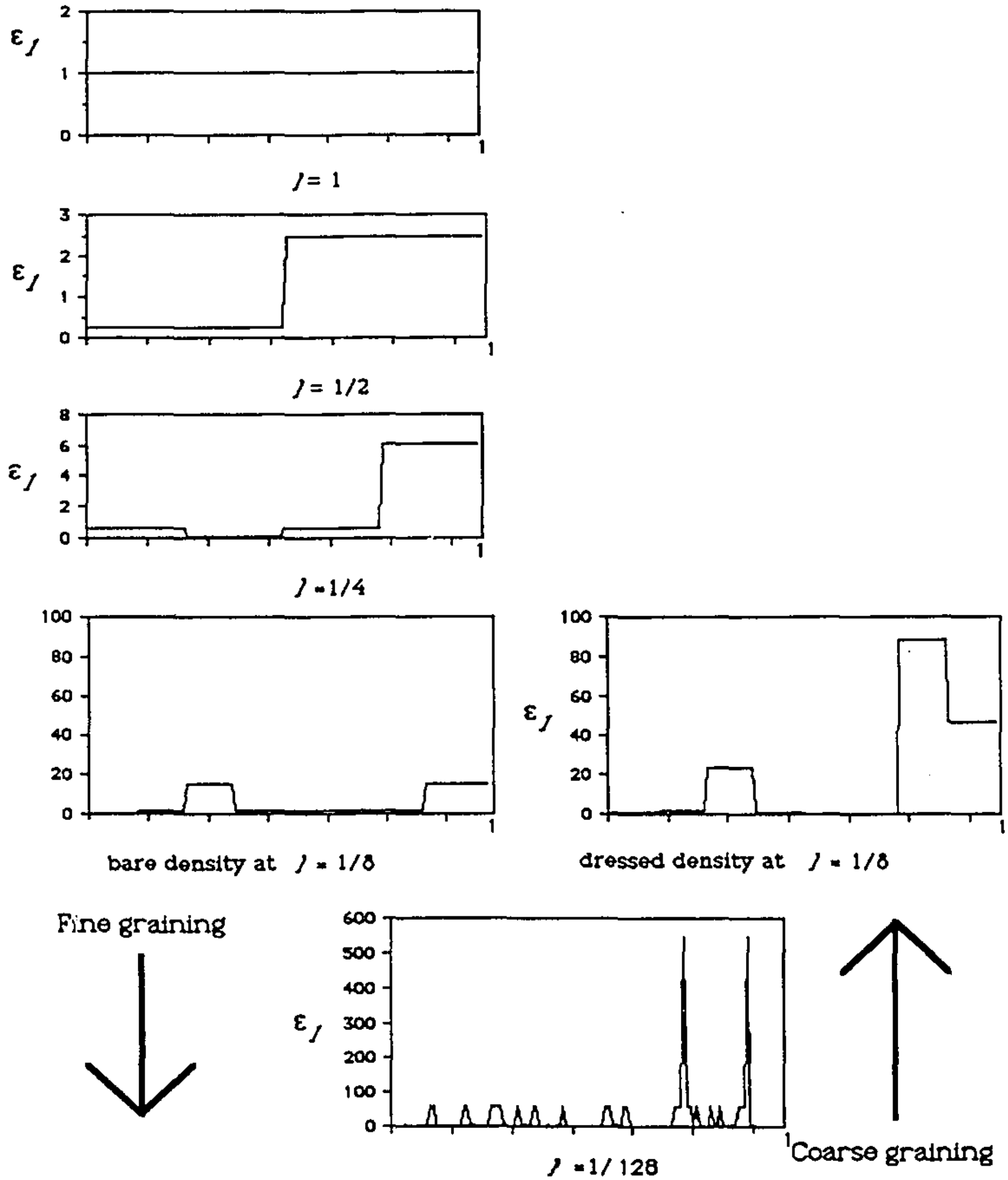

Figure 2-1b: A discrete (α model) cascade in one dimension At each step, the unit interval is broken up into intervals half the size of the previous step and the energy flux density (vertical axis) is multiplied by a random factor. In the α model, there are only two possibilities- a boost or a decrease with probabilities chosen to respect ensemble conservation $\langle\varepsilon_l\rangle=1$. Reproduced from Lavallée [58].

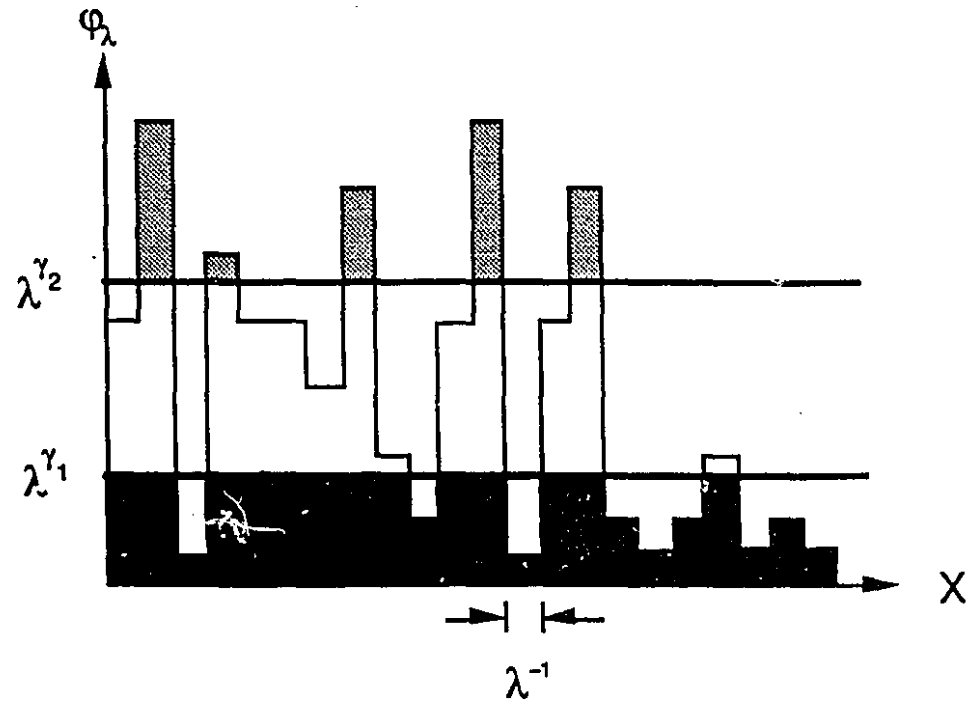

Figure 2-2: A schematic diagram showing a multifractal energy flux density (φ_λ) with smallest resolution λ^{-1}, and indicating the exceedance sets corresponding to two orders of singularities γ_1, γ_2.

This geometric interpretation can be useful in data analysis. For example, consider a data set consisting of N_s satellite photographs (assumed to be statistically independent realizations from the same statistical ensemble). A single D dimensional picture (D=2 in this example) will enable us to explore structures with dimension $D \geq D(\gamma) \geq 0$; structures with $c(\gamma) > D$ (which would correspond to impossible negative values of $D(\gamma)$) will be too sparse to be observed (they will almost surely not be present on a given realization). This restriction on the accessible values of $c(\gamma)$ is shown in fig. 2-3; to explore more of the probability space, we will require many photographs. With N_s photographs, the accessible range of singularities can readily be estimated. If each photograph has a range of scales λ (= the ratio of the size of the picture to the smallest resolution = the number of "pixels" on a side), then introduce the "sampling dimension" (Schertzer and Lovejoy [114], Lavallée et al [59]): $D_s = \log N_s / \log\lambda$; it is not hard to see (fig. 2-3) that the accessible range will be $\gamma < \gamma_s$, with $c(\gamma_s) = D + D_s$.

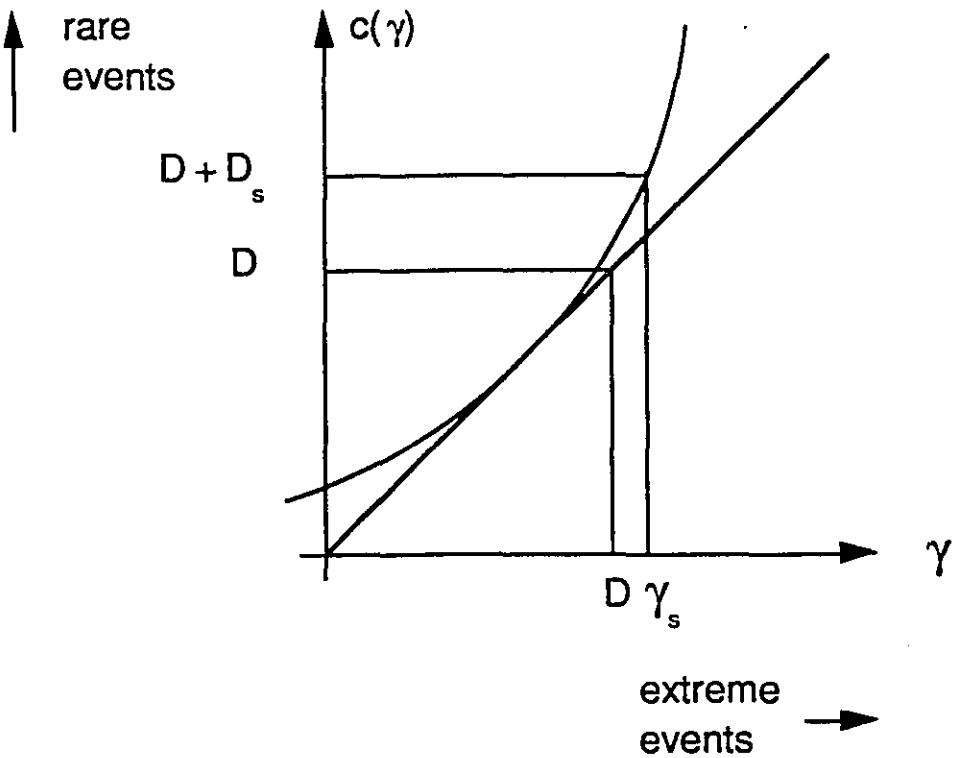

Figure 2-3: A schematic diagram showing a typical codimension function for a conserved process (H=0). The lines $c(\gamma)=D$, $\gamma=D$ indicate the limits of the accessible range of singularities for a single realization, dimension D. The corresponding lines for $D+D_S$, where D_S is the sampling dimension are also shown. As we analyze more and more samples, we explore a larger and larger fraction of the probability space of the process, hence finding more and more extreme (are rare) singularities.

Codimension $c(\gamma)$ has many other properties that are readily illustrated graphically. A fundamental property which is derived by considering statistical moments (below), is that it must be convex. It must also be tangent to the line x=y (the bisectrix). This is because $\langle\varphi_\lambda\rangle \approx \lambda^{\gamma-c(\gamma)}$ = constant, hence the singularity corresponding to the mean of the process, $\gamma=C_1$, satisfies the fixed point relation $C_1=c(C_1)$ as indicated in fig. 2-4. C_1 is thus the codimension of the mean process; if the process is observed on a space of dimension D, it must satisfy $D\geq C_1$, otherwise, following the above, the mean will be so sparse that the process will (almost surely) be zero everywhere; it will be "degenerate". We can also consider the (non conserved) ΔR_λ; it is obtained from φ_λ by multiplication by λ^{-H}, wherever, $\varphi_\lambda=\lambda^\gamma$, we have $\Delta R_\lambda=\lambda^{\gamma-H}$; i.e. by the translation of singularities by -H (see fig. 2-5). Finally, since $c(\gamma)$ is convex with fixed point C_1, it is possible (see fig. 2-6) to define the degree of multifractality (α) by the (local) rate of change of slope at C_1, it radius of curvature $R_c(C_1)$:

$$R_c(C_1) = 2^{2/3}\alpha C_1 \quad (2.5)$$

In universal multifractals (below), this local description obtained with just three terms in Taylor expansion gives all the relevant parameters for a global description of the $c(\gamma)$ function, and we find an upper bound (maximum degree of multifractality) α=2, yielding a parabola. The α=0 case is the monofractal extreme (called the "β model", Frisch et al [33]) whose singularities all have the same fractal dimension (see fig. 2-6).

Rather than specifying the statistical properties via the scaling of probabilities $c(\gamma)$ it can (equivalently) be specified by the scaling of the statistical moments. Consider the q^{th} order statistical moments $\langle\varphi_\lambda{}^q\rangle$. We can now define the multiple scaling exponent $K(q)$:

$$\left\langle \varphi_\lambda^q \right\rangle \approx \lambda^{K(q)}, \quad \lambda > 1 \quad (2.6)$$

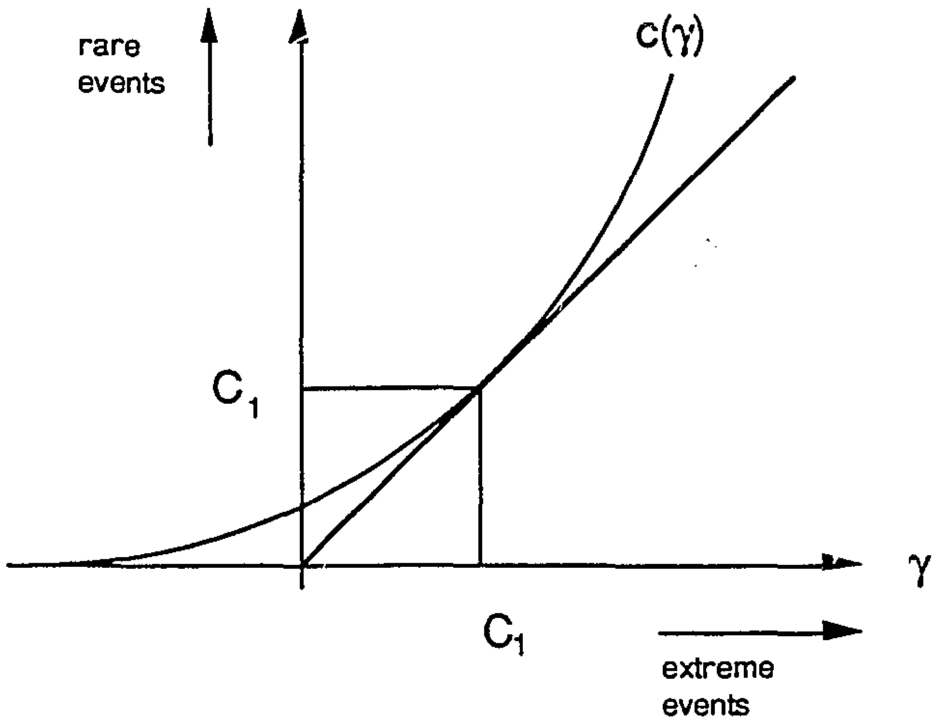

Figure 2-4: Same as previous, but showing the fixed point $C_1=c(C_1)$, the singularity corresponding to the mean of the process. The diagonal line is the bisectrix ($\gamma=c(\gamma)$).

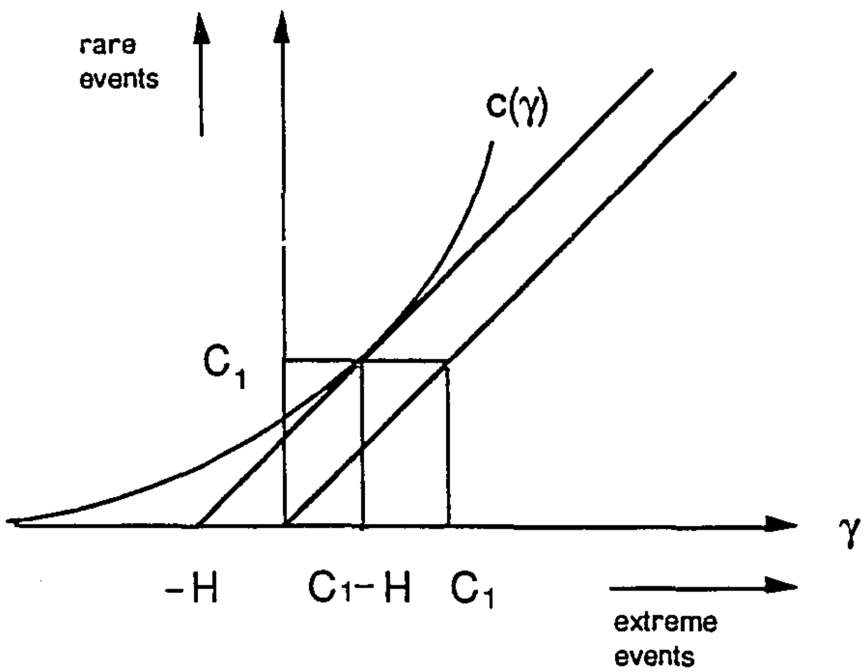

Figure 2-5: Same as 2-4, but for a non conserved process. All the singularities are shifted by -H.

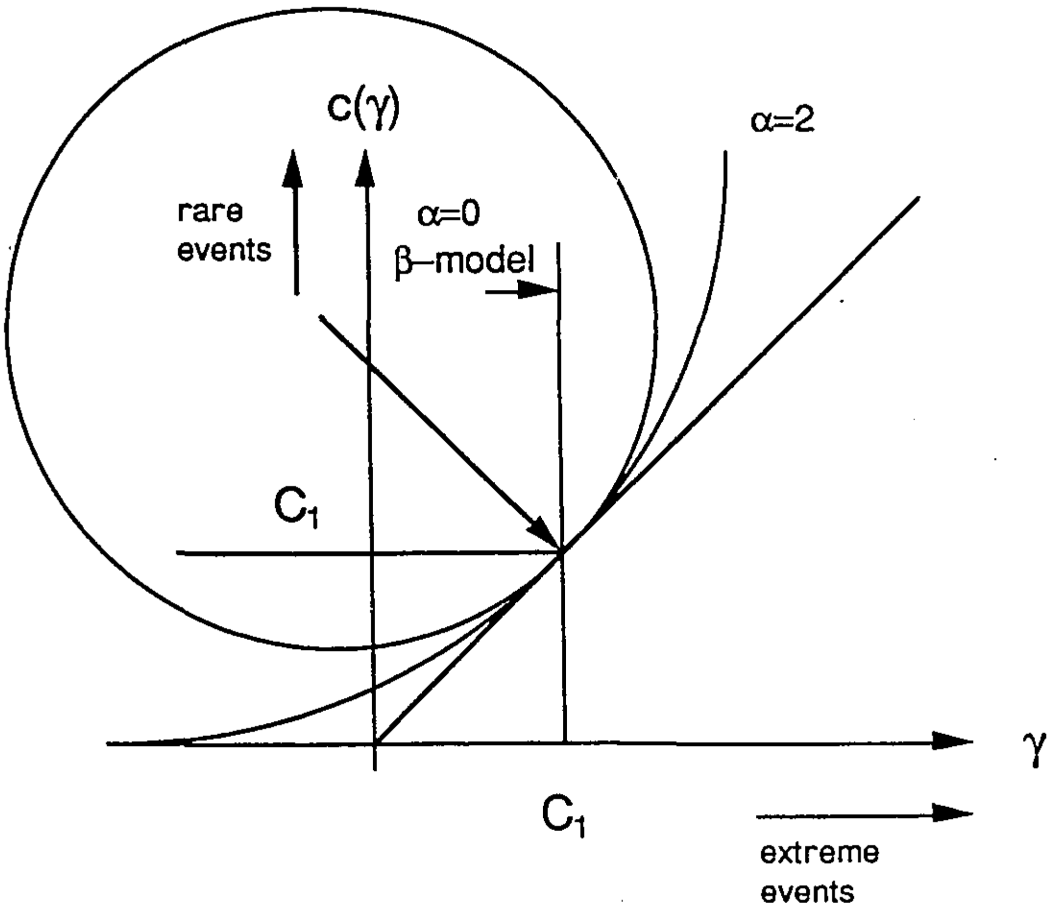

Figure 2-6: Same as 2-4, but showing the radius of curvature ($=2^{2/3}C_1\alpha$) at the fixed point which locally defines α. For comparison, the two extreme universal multifractals are also shown, corresponding to α=0 (the β model), α=2 (the lognormal model).

In parallel to this turbulent multifractal formalism, Hentchel and Procaccia [43], Grassberger [41], Halsey et al [42] and others elaborated a strange attractor formalism for dealing with multifractal probability measures in low dimensional phase spaces. They were primarily interested in the fractal dimensions of geometric sets associated with singularities of measures (rather than densities). This strange attractor notation is related to the turbulence notation as follows:

$$f_D(\alpha_D) = D-c(\gamma);\ \alpha_D = D-\gamma \tag{2.7}$$

In turbulence we are interested in stochastic processes defined on (infinite dimensional) probability spaces, hence the intrinsic (D independent) notation.

K(q), c(γ) are related by the following Legendre transformations (Parisi and Frisch, [94]):

$$K(q) = \max_\gamma (q\gamma - c(\gamma)); \qquad c(\gamma) = \max_q (q\gamma - K(q)) \tag{2.8}$$

which relate points on the c(γ) function to tangencies on the K(q) function and visa versa; $\gamma = K'(q)$, $q = c'(\gamma)$. For example, a quantity that will be useful below in estimating the multifractal parameters of radiances and reflectivities is the sampling moment q_s which is the maximum order moment that can be accurately estimated with a finite sample. Recalling that the maximum accessible order of singularity was $\gamma_s = c^{-1}(D+D_s)$, we obtain: $q_s = c'(\gamma_s)$. Fig. 2-7 shows a schematic of K(q); for conserved fields, we have $C_1 = K'(1)$, (i.e., q=1 corresponds to $\gamma = C_1$), the corresponding radius of curvature is $R_K(1) = (1+C_1^2)^{2/3}/(C_1\alpha)$. The functions for the corresponding non conserved fields ($H \neq 0$) are obtained by $\gamma \rightarrow \gamma - H$, $K(q) \rightarrow K(q) - Hq$.

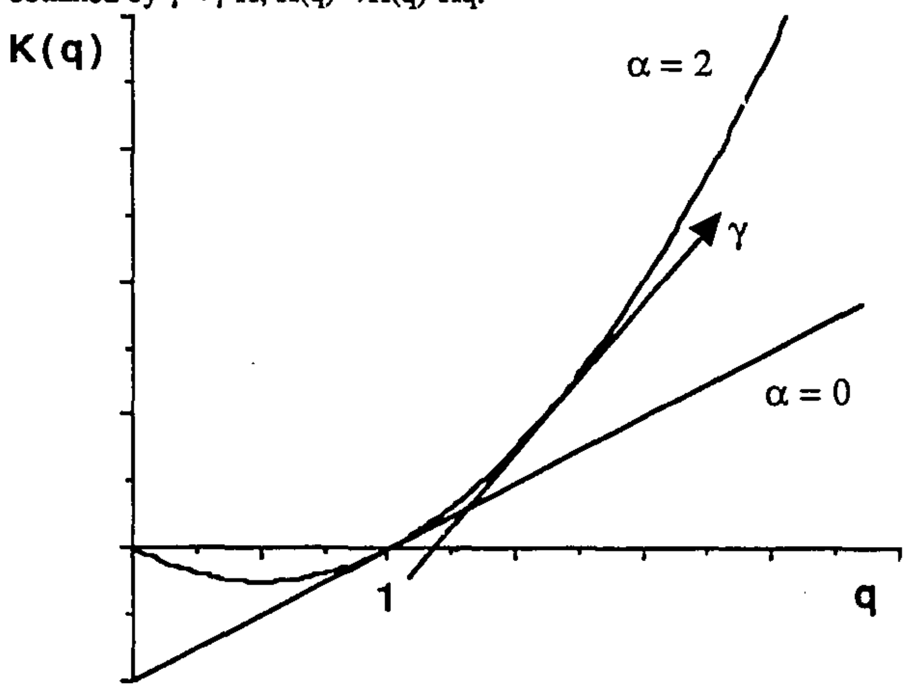

Figure 2-7: The K(q) curves corresponding to the c(γ) curves in fig. 2-6. For $\alpha = 0$ we have that $K(q) = C_1(q-1)$. Also shown is a typical tangent whose slope $K'(q) = \gamma$ provides the one to one correspondence between orders of singularities and moments.

In summary, this local characterization of the behavior of multifractals near the mean involves the three parameters (H, C_1, α) respectively characterizing the deviation of the observed field from the conserved field φ, the sparseness of the latter, and the degree of multifractality.

Finally, we must make a distinction between the "bare" and "dressed" multifractal properties (Schertzer and Lovejoy [109]). The "bare" properties are those which have been discussed above, they correspond to the construction of the process over a finite range of scales λ. In contrast, the "dressed" quantities are obtained by integrating (averaging) a completed cascade over the corresponding scale. Experimentally measured quantities are generally "dressed" since geophysical sensors typically have resolutions which are much lower than the scale below which the fields they are measuring become homogeneous (in the atmosphere, the latter is usually of the order of 1 mm or less). The dressed quantities generally display an extreme, "hard" behavior involving divergence of high order statistical moments. Specifically, for averages over observing sets with dimension D there is a critical order moment q_D (and corresponding order of singularity $\gamma_D = K'(q_D)$) such that:

$$\langle \varphi_\lambda^q \rangle = \infty \quad q \geq q_D \tag{2.9}$$

where q_D is given by the following equation:

$$K(q_D) = (q_D - 1)D \tag{2.10}$$

II.1.3 Universal multifractals:

The above discussion is quite general and at this level, it has the unpleasant consequence that an infinite number of scaling parameters (the entire $c(\gamma)$, $K(q)$ functions) will be required to fully specify the multiple scaling of our field. Fortunately, real physical processes will typically involve both nonlinear "mixing[3]" (Schertzer et al 1[116]) of different multifractal processes, as well as a "densification[4]" (Schertzer and Lovejoy [110]) of the process leading to a continuum of scales (rather than just the discrete scales indicated in fig. 2-1a,b). Either of these mechanisms is sufficient so that the above H, C_1, α description becomes global; we obtain the following universal multifractal functions:

$$c(\gamma-H)=\begin{cases} C_1\left(\dfrac{\gamma}{C_1\alpha'}+\dfrac{1}{\alpha}\right)^{\alpha'} & \alpha\neq 1 \\ C_1\exp\left(\dfrac{\gamma}{C_1}-1\right) & \alpha=1 \end{cases} \tag{2.11}$$

$$K(q)+qH=\begin{cases} \dfrac{C_1}{\alpha-1}\left(q^{\alpha}-q\right) & \alpha\neq 1 \\ C_1 q\mathrm{Log}(q) & \alpha=1 \end{cases} \quad (\text{for } 0\leq\alpha\leq 2,\ q\geq 0) \tag{2.12}$$

The multifractality parameter α is the Levy index and indicates the class to which the probability distribution belongs. There are actually 5 qualitatively different cases. The case $\alpha = 2$ corresponds to lognormal[5] multifractals, the case $1 < \alpha < 2$ corresponds to (log) Levy processes with unbounded singularities, $\alpha = 1$ corresponds to log Cauchy multifractals. These three cases all are "unconditionally hard" multifractals, since for any D, divergence of moments will occur for large enough q (q_D is always finite). When $0 < \alpha < 1$ we have (log) Levy processes with bounded singularities. By integrating

[3] By keeping the total range of scale λ fixed and finite, we may mix (by multiplying them) independent processes of the same type, preserving certain characteristics (e.g. the variance of the resulting processes).
[4] Introducing more and more intermediate scales in a given multiplicative process.
[5] This is nearly the same as the lognormal multiscaling model of turbulence proposed by Kolmogorov [54], Obhukhov [89], except that the latter missed the essential point about the divergence of high order moments, thinking in terms of pointwise processes.

(smoothing) such multifractals over an observing set with large enough dimension D it is possible to tame all the divergences yielding "soft" behavior, these multifractals are only conditionally "hard". Finally $\alpha = 0$ corresponds to the most popular and (too!) well-known monofractal "β model", Novikov and Stewart [86], Mandelbrot [78] and Frisch et al. [33]). A more detailed discussion about these five cases and in particular about the generators of the Levy variables can be found in Schertzer et al [112], Fan [31], and Schertzer and Lovejoy [113] (see also Lovejoy and Schertzer [71, 73] for some applications and review). Universal multifractals have been empirically found in both turbulent temperature and wind data (Schmitt et al [119, 120]). They have also recently found applications in high energy physics (Brax and Peschanski [11]), as well as oceanography (Tessier et al. [130]), earthquakes (Beltrami et al. [6]) and landscape topography (Lavallée et al [59]). The first empirical estimates of C_1, α in cloud radiances are discussed in Lovejoy and Schertzer [71] (see also Gabriel et al [34]) and for rain reflectivities, Seed [123].

Using the universal multifractal formulae above, some of the results discussed earlier may be expressed in simpler form. Formulae which will prove useful below are for q_s (the maximum order moment that can be reliably estimated with a finite sample), and q_D, the critical order for divergence (obtained by solving 2.10 for q_D:

$$q_s = \left[\frac{D+D_s}{C_1}\right]^{1/\alpha} \tag{2.13a}$$

$$\frac{C_1}{\alpha - 1}\,\frac{q_D{}^{\alpha} - q_D}{q_D - 1} = D \tag{2.13b}$$

Formula 2.13a is only valid for $q_s < q_D$. Both of these critical moments are associated with "multifractal phase transitions" (Schertzer et al [117]), and algebraic probabilities (finite q_D) are considered a basic characteristic of self-organized criticality (Bak et al [3]).

II.2 The Double Trace Moment Technique :

II.2.1 Basic Ideas :

We have argued above that atmospheric fields are multifractal, involving an infinite number of scaling exponents (the functions $c(\gamma)$, $K(q)$), but that due to universality, the latter may be characterized by the three basic parameters (H, C_1, α). In this section we briefly discuss how this idea may be tested, and how the parameters estimated. There are methods other than the DTM that can be used to evaluate those parameters and we will discuss them in other chapters but since this is the best one and that we will be using it most we decided to explain it in this introduction chapter.

The physics literature is now replete with different methods developed for estimating multifractal parameters. Unfortunately, the great majority of these have been designed for the particularly "calm" multifractals associated with strange attractors, a few for the slightly less calm "microcanonical" multifractals[6], but virtually none for the general ("canonical") multifractals involving the occasional "hard" singularities discussed earlier. When applied to turbulent and/or geophysical data involving extreme variability, they will have limited accuracy. A final limitation on their accuracy comes from the fact that they have attempted to estimate an infinite number of parameters with finite data sets (the entire $c(\gamma)$, $K(q)$ function, each value of which is a scaling exponent). We now describe a simple technique that overcomes these problems by exploiting the universality to estimate C_1 and α directly; $c(\gamma)$, $K(q)$ are then obtained using eqs. 2.11, 2.12. H is then estimated by combining the C_1 and α estimates with the scaling exponent of the energy spectrum (section II.2.2).

---

[6]This is true for example of approaches bases on partition functions and moments (Halsey et al [42]), single scale histograms (Atmanspacher et al [1], Paladin and Vulpiani [91], multipliers (Chabra and Sreenivasan [15]) and wavelets (Bacry et al [2]).

Consider the conserved (H=0) multifractal flux density at (fine) resolution Λ (the ratio of the outer (largest) scale of interest to the smallest scale of homogeneity[7]). The (dressed) flux over an observing set (B_λ, this corresponds to a single lower resolution "pixel") with dimension D, resolution $\lambda<\Lambda$ is simply an integral over the density:

$$\Pi_\Lambda(B_\lambda) = \int_{B_\lambda} \varphi_\Lambda d^D x \tag{2.14}$$

We may now define the q^{th} order "Trace moments" (Schertzer and Lovejoy[8] [109]) by summing $\Pi^q_\Lambda(B_\lambda)$ over each individual realization[9] (each satellite picture, covering the region A has λ^D disjoint covering sets B_λ which are summed over in eq. 2.15, see the schematic illustration, fig. 2-8 with $\eta = 1$), and then ensemble averaging over all the realizations:

$$\mathrm{Tr}_\lambda(\varphi_\Lambda)^q = \left\langle \sum_i \Pi^q_\lambda(B_{\lambda,i}) \right\rangle \approx \lambda^{K(q)-(q-1)D} \tag{2.15}$$

where the sum is over all the i "balls" $B_{\lambda,i}$ needed to cover A. This formula will break down for moments $q>q_D$, and (when finite samples are used to estimate the ensemble average) when $q>q_s$. Although it allows the determination of K(q) (at least for small enough q), and hence in principle the determination of C_1, α (via eq. 2.12) this method will involve ill-conditioned nonlinear regressions (K(q) vs. q). The double trace moment (DTM) technique (Lavallée et al 1[59], Lavallée [58]) avoids this problem by generalizing the trace moment; it introduces a second moment η by transforming the high resolution field $\varphi_\Lambda \rightarrow \varphi^\eta_\Lambda$. This transforms the flux Π into an η flux $\Pi^{(\eta)}$:

$$\Pi^{(\eta)}_\Lambda(B_\lambda) = \int_{B_\lambda} \varphi^\eta_\Lambda d^D x \tag{2.16}$$

---

[7] For scales smaller than the scale of homogeneity we assume that the field is homogeneous (below the scale at which we have dissipation of energy the field is assume to be homogeneous.). In the actual use of the DTM method we take λ' as the smallest scale known (the pixel scale) for the analysed field.

[8] Although the formalism above was developed in Schertzer and Lovejoy [109], essentially the same method was empirically applied to on rain in Schertzer and Lovejoy [107].

[9] This yields a partition function.

The double trace moment can then be defined as:

$$\mathrm{Tr}_\lambda\left(\varphi_\Lambda^\eta\right)^q = \left\langle \sum_i \left[\Pi_\Lambda^{(\eta)}\left(B_{\lambda,i}\right)\right]^q \right\rangle \approx \lambda^{K(q,\eta)-(q-1)D} \tag{2.17}$$

where we have introduced the (double) exponent $K(q,\eta)$, which reduces to the usual exponent when $\eta=1$: $K(q,1)=K(q)$.

The entire transformation from single to double trace moments can be summarized in the following formulae (where the prime indicates transformed, double trace quantities, not differentiation):

$$\gamma \rightarrow \gamma' = \eta\gamma - K(\eta) \tag{2.18a}$$

$$c(\gamma) \rightarrow c'(\gamma') = c(\gamma) \tag{2.18b}$$

$$q \rightarrow q' = q/\eta \tag{2.18c}$$

$$K(q) \rightarrow K'(q') = K(q,\eta) = K(\eta q') - q'K(\eta) \tag{2.18d}$$

Note the fine point in the above is that due to the integration, we are dealing with dressed rather than bare quantities, hence the dressed singularities (eq. 2.18a) transform with an extra term ($-K(\eta)$); necessary since the dressing operation enforces conservation of the η flux.

The real advantage of the DTM technique becomes apparent when it is applied to universal multifractals (Lavallée [58]) since we obtain the following transformations of C_1:

$$C_1 \left(= \frac{dK}{dq}\Big|_{q=1}\right) \rightarrow C_1' \left(= \frac{dK'}{dq'}\Big|_{q'=1}\right) = C_1\eta^\alpha \tag{2.19}$$

Therefore, $K'(q') = K(q,\eta)$ has a particularly simple dependence on η:

$$K(q,\eta) = \eta^\alpha K(q) \tag{2.20}$$

α can therefore be estimated on a simple plot of log $K(q,\eta)$ vs. log η for fixed q. By varying q, we improve our statistical accuracy. Finally, note that due to eq. 2.18d, whenever $\max(q\eta,q)>\min(q_s,q_D)$ the above relation will break down; $K(q,\eta)$ will become independent of η. For more details on the double trace moment, see Lavallée et al [59], Lavallée [58]. We shall see that effective exploitation of the above involves a "bootstrap" procedure in which the well estimated low q, η exponents are used to estimate α, C_1, and then eqs. 2.11a,b can be used to predict the range of reliable estimates.

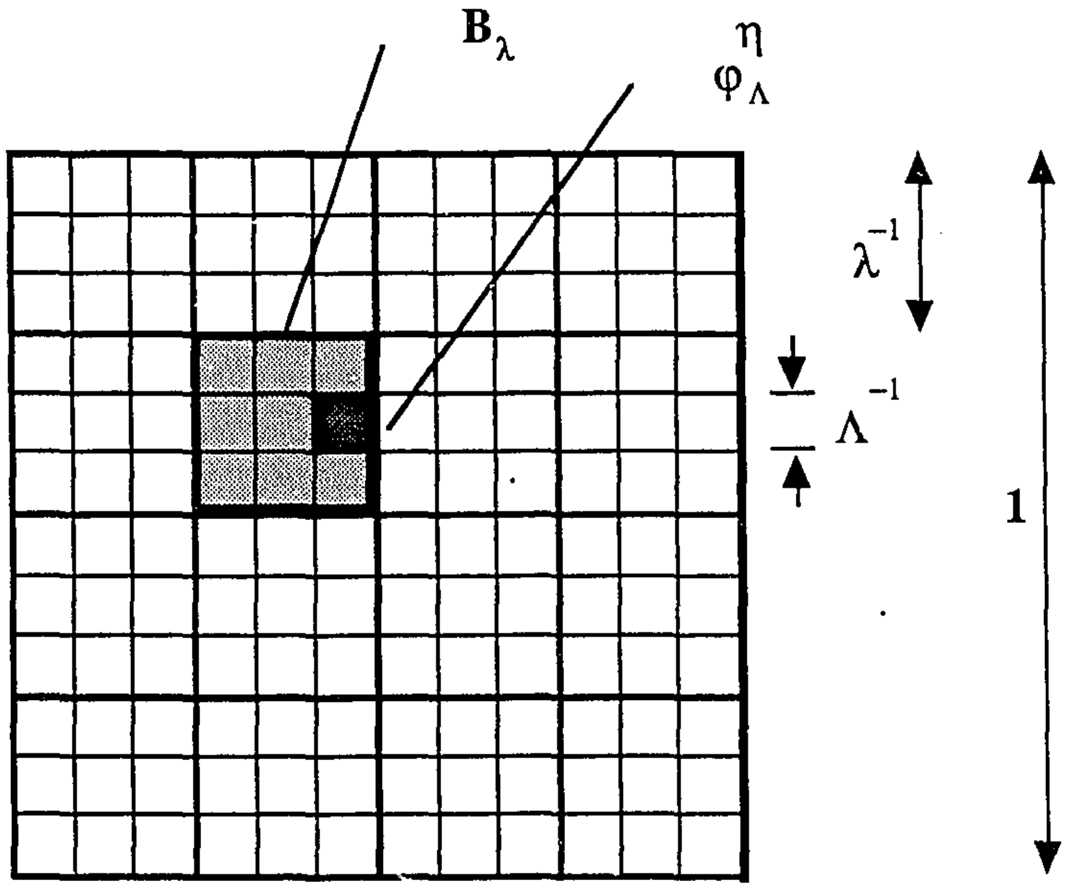

Figure 2-8: A schematic diagram illustrating the different averaging scales used in the double trace moment technique.

II.2.2 Estimating H:

We have seen that in multiplicative processes, it is convenient to isolate an underlying conserved quantity which has basic physical significance; in turbulence it was the energy flux to smaller scales, in rainfall we denoted it by φ, and related it to the rain fluctuations via eq. 2.2. In terms of the scaling, conservation means $<\varphi_\lambda>$ = constant (independent[10] of λ), hence $K(1)=0$. If we consider the energy spectrum of φ_λ, it is of the form $k^{-\beta}$ with[11] $\beta = 1 - K(2)$, i.e., the spectrum is always less steep than a 1/f noise[12].

The reason for dwelling on this is that it illustrates a basic point common to many geophysical fields viz., their spectra have $\beta>1$, hence they cannot be stationary processes, they must be (fractionally) differentiated[13] by order -H (the spectra must be power law filtered by k^H) to become stationary. For rain and clouds, this will mean removing the λ^{-H} term in order to obtain the stationary φ_λ from the non stationary ΔR_λ. The importance of this for analysis has long been realized; for example standard geophysical statistics use variograms rather than autocorrelation functions[14] to avoid convergence problems when $\beta>1$. The same considerations apply to the use of the DTM technique. Fig. 2-9 (from Lavallée [58]) shows the result when a simulated conserved process is fractionally integrated and differentiated by varying amounts: as long as we differentiate (filter by k^H with $H>0$) we obtain stable and accurate estimates of both C_1 and α. However when we fractionally integrate ($H<0$), we only recover α; C_1 is not accurately

---

[10] Recall from section 3 that λ is the ratio of the largest to the smallest scale, hence taking the largest scale = 1 for simplicity, we have $\lambda = l^{-1}$.

[11] This formula is a consequence of the fact that the energy spectrum is the fourier transform of the autocorrelation function which is a second order moment.

[12] The difference is often not great since K(2) is usually small: $= C_1(2^\alpha-2)/(\alpha-1)$, and $0\leq\alpha\leq2$.

[13] See Schertzer and Lovejoy [115] appendix B.2 for more discussion of fractional derivatives and integrals.

[14] In time series we analyse the differences (finite derivatives) rather than the series itself.

determined[15]. This figure also clearly indicates that as long as the spectrum is less steep than the underlying conserved process ($\beta<1-K(2)$), that we can recover C_1. From the C_1, α estimated this way, we can determine K(2) from eq. 2.10 and hence the β of the conserved process, and infer the amount of fractional integration required to go from the underlying conserved process to the observed non conserved process[16]. Writing β for the spectral slope of the observed process, the order of fractional integration required to go from the conserved process to the non conserved (observed) process is therefore given by:

$$H=\frac{\beta-1+K(2)}{2}=\frac{\beta-1}{2}+\frac{C_1(2^{\alpha}-2)}{2(\alpha-1)} \tag{2.21}$$

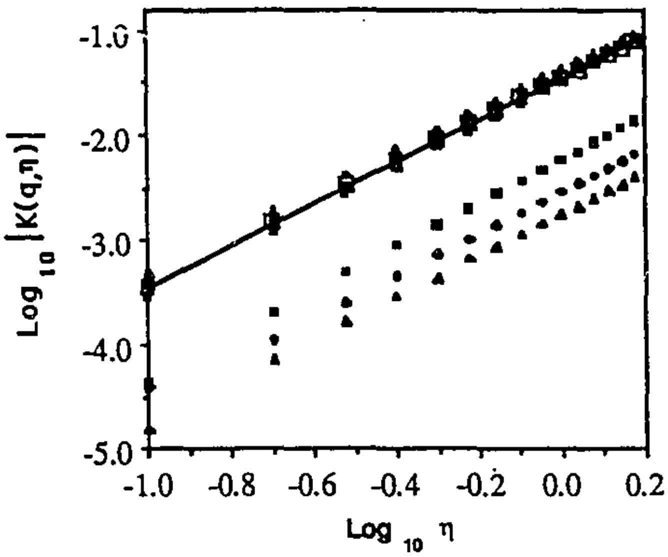

Figure 2-9: log(|K(q,η)|) versus log(η) with α = 2 (lognormal), C_1 = 0.15, D = 2, are given for q = 0.5. The curve of the stationary processes (big hollow square) is compared to those of the same processes after fractional differentiation (white symbols, H = -2, -1 and -0.5 from top to bottom). The fractional differentiation and integration does not affect the estimate of α (all the slopes are parallel), but fractional integration leads to biased estimates of C_1 (the curve with black symbols are all shifted downwards compared to the theoretical stationary processes shown by the line. Reproduced from Lavallée [58].

---

15 Note that in many geophysical fields, the absolute value of the field may not be important. It may be sufficient to only consider fluctuations, hence we may put the mean=0 by setting the 0^{th} fourier component =0. In some cases this component may be important and must be carefully dealt with in real space - see appendix B.2, Schertzer and Lovejoy [115].

16 In the case of turbulence, it is not necessary to infer the relation since it is given by dimensional analysis from known dynamical quantities. For rainfall and cloud radiances, we don't know the corresponding dynamical (partial differential) equations, nor their conserved quantities, so that this type of empirical inference is unavoidable.

As a final comment before turning to the actual data analysis, we describe a short-cut which in many cases enables us to avoid the use of Fourier space. In 1-D we have already recalled that replacing the time series by its differences is approximately the same as multiplying by k in Fourier space[17]. To generalize this to two (or more) dimensions, one possibility is to use a finite difference Laplacian. This multiplies by $|\underline{k}|^2$ in Fourier space, hence the spectrum by $|\underline{k}|^4$; although this is quite drastic we will see that it apparently works fairly well. Differencing the experimental data also remove the problem of physical quantities that are only defined within additive constant. This also has the advantage that it removes any (unknown) additive constant that would mask the scaling behavior. Denoting the modulus of the gradient of the rain (or radiance) field by $|\nabla R|$ we have

$$|\nabla R(x,y)| = \sqrt{\left(\frac{\partial R}{\partial x}\right)^2 + \left(\frac{\partial R}{\partial y}\right)^2} \tag{2.22}$$

which can be approximated by the finite difference

$$|\nabla R(i,j)| \approx \sqrt{(R(i+1,j) - R(i-1,j))^2 + (R(i,j+1) - R(i,j-1))^2} \tag{2.23}$$

with $\Delta x = \Delta y = 1$. The index i and j are respectively the horizontal and vertical coordinates, the finite difference operations are effectuated without privileging any particular direction; problems related to anisotropy are neglected. In the same manner the Laplacian:

$$|\nabla^2 R(x,y)| = \left|\frac{\partial^2 R}{\partial x^2} + \frac{\partial^2 R}{\partial y^2}\right| \tag{2.24}$$

is approximated by:

$$|\nabla^2 R(x,y)| \approx \left|\frac{1}{4}(4R(i,j) - R(i+1,j) - R(i-1,j) - R(i,j+1) - R(i,j-1))\right| \tag{2.25}$$

---

[17]This will not be exactly true at the highest frequencies corresponding to the resolution the series.

II.3 The role of satellite radiances and radar reflectivities:

Even before the theoretical basis of the standard model was brought into question, a series of in situ velocity measurement campaigns (Vinnechenko [133], Gage [35], Lilly [61], Nastrom and Gage [85] -- for discussions and references see Schertzer and Lovejoy [107], Lovejoy and Schertzer [67]) -- failed to find evidence for the mesoscale "gap" anywhere near the designated 1-100 km range. However, even though these campaigns did measure velocity fluctuations over various ranges (several meters to thousands of kilometers) with sufficient statistical reliability to eliminate the possibility of a significant gap, the extreme intermittency of the atmosphere and various experimental difficulties has hindered the emergence of a clear overall (large to small scale) statistical picture of the wind field. One way of attempting to overcome the limitation of in situ wind measurements -- which we explore below -- is to exploit the burgeoning masses of remotely sensed satellite and radar data. Because of the strong (nonlinear) couplings between the various atmospheric fields, any fundamental break in the scaling symmetry in the dynamical (wind) field will be reflected in the latter. Conversely, if the latter are scaling over the observed ranges, we may infer that the symmetry is not broken in the former. The symmetry will be respected unless specific (and strong enough) mechanism exists to break it. A scaling break in one field would constitute a sufficient mechanism to cause a break in any other strongly dynamically coupled field. The cloud, radiance and velocity are strongly coupled. This result follows from the consideration of scale invariance as a symmetry principle.

In any case, satellite cloud radiances and radar rain reflectivities are interesting in their own right, and -- as argued elsewhere (Lovejoy and Schertzer [71], Lovejoy et al [75]) -- provide unique data sets for testing new ideas in scaling and multifractals[18].

---

[18]It is significant that the first empirical data set (in meteorology or elsewhere) whose multifractal dimensions were estimated was the radar reflectivity field of rain, Schertzer and Lovejoy [108].

In this chapter, we focus on the scaling properties of various fields related to the liquid water field. The distribution of cloud and rain liquid water is important both for our understanding of atmospheric dynamics, but also in its own right: it is a fundamental part of the water cycle, and (when it reaches the ground) is the basic hydrological field. The data sets used include LANDSAT, NOAA-9, METEOSAT satellite cloud radiances in the visible, thermal infra red and near infra red wavelength bands (from ≈166m to ≈4000 km overall). In section II.5 we analyze radar reflectivities of rain in both time and space and include a comparison of the latter with global in situ raingage measurements. On all of these data sets we not only test the scaling (which is generally found to hold quite well), but also estimate the fundamental universal multifractal exponents characterizing the fields. Finally in section II.6, we briefly indicate how knowledge of these exponents can be used to create (both static and dynamic) multifractal models of the corresponding fields.

II.4 The Horizontal scaling properties of cloud radiances:

We have already discussed scale invariance as an important atmospheric symmetry principle. If, over the range in which most of the interactions with the solar and blackbody radiation fields occur, it applies to the distribution of water in the atmosphere then the radiance fields will also be scale invariant over the corresponding range[19]. Although the multifractal parameters of the radiation fields will be non-trivially related to those of the liquid water field they will still give us valuable information about the limits to scaling, anisotropic scaling (Pflug et al. [97], Lovejoy et al [75]) and the relation between cloud and radiation fields.

Because of the ready availability of high quality satellite data, and our desire to obtain a resolution independent characterization of the satellite data, we analyzed images emanating from several different satellites and sensors (summarized in table 2-1).

---

[19] i.e. they will not break the scaling symmetry. Formally, this is because the radiative transfer equations have no characteristic length associated with them.

Location	Satellite	Sensor	wave-length	resolution	picture size
Tropical Pacific	LANDSAT	MSS	0.49 to 0.61 μm	166m[20]	512x512 89 km
Atlantic West of Spain	METEOSAT	Visible Channel	0.4 to 1.1 μm	8 km[21]	512x512 4000 km
Atlantic West of Spain	METEOSAT	infrared Channel	10.5 to 12.5 μm		
Atlantic East of Florida	NOAA-9	AVHRR Channel 1	0.5 to 0.7 μm	1.1 km	512x512 550 km
		AVHRR Channel 2	0.7 to 1.0 μm		
		AVHRR Channel 3	3.6 to 3.9 μm		
		AVHRR Channel 4	10.4 to 11.1 μm		
		AVHRR Channel 5	11.4 to 12.2 μm		

Table 2-1: The characteristics of the different satellite images analyzed.

The first analysis performed was the estimation of the (isotropic) energy (power) spectrum which is the modulus squared of the Fourier amplitudes integrated over all angles in Fourier space and ensemble averaged over all realizations of the process. As usual the ensemble averaging was approximated by averaging over all the available samples with the same wavelength bands and resolution. Figure 2-10 shows the results for the satellite images and the frequency range of the images (following the same classification as in table 2-1). For all the spectra we observe reasonable scaling behavior for the entire range accessible to each satellite. We obtained the following results (from bottom to top): LANDSAT (visible) $\beta = 1.7$, METEOSAT (visible) $\beta = 1.4$, METEOSAT (infra red) $\beta = 1.7$, NOAA-9 (channel 1 to 5) $\beta = 1.67, 1.67, 1.49, 1.91, 1.85$. The variations in the exponents have both statistical and systematic origins. First spectral exponents of intermittent data are notoriously difficult to estimate requiring very large sample sizes. Second, the spectral bands vary from one satellite to another. Even if we

[20] The resolution of the sensor is 83 m but we had to degrade this resolution in order to avoid certain problems discussed in the text.
[21] The visible channel data was originally at a higher resolution and was resampled on a 8 km grid.

have labeled them as being in the same group (visible, near infra red, thermal infra red) they are not completely coincident as can be seen in table 2-1. Roughly speaking the radiative transfer in the visible is dominated by scattering, in the near infra red it combines both scattering with absorption and emission while in the thermal infra red it is dominated by absorption and thermal emission. Since these radiative transfer processes are quite different we expect some systematic variation in the power spectra. We take these results as good evidence that the basic scaling is respected over the range of ~200 m to ~4000 km.

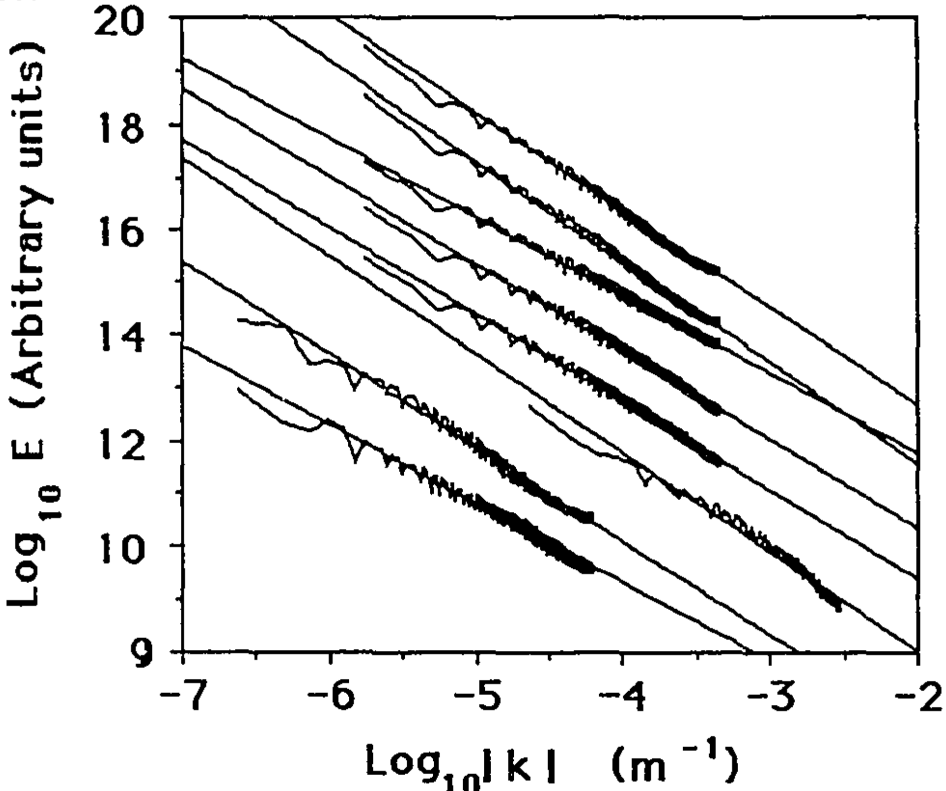

Figure 2-10: Average power spectrum for the satellites images grouped according to the satellite and the frequency range of the images (from bottom to top): LANDSAT (visible) β = 1.7, METEOSAT (visible) β = 1.4, METEOSAT (infra red) β = 1.7, NOAA-9 (channel 1 to 5) β = 1.67, 1.67, 1.49, 1.91, 1.85.

The DTM analysis was done on each group of images considering each scene as a separate realization. In figure 2-11 we show $\log\left(\mathrm{Tr}_\lambda\left(\varphi_\Lambda^\eta\right)^q\right)$ vs $\log(\lambda)$ for several values of η for the LANDSAT images. The same plot is shown in figure 2-12 for METEOSAT images in the visible and infra red channels. We also show the corresponding graph (figure 2-13) for all the channels of NOAA-9. As expected from the spectral analysis, these graphs are nearly linear over all the accessible range. This is another confirmation that scaling is obeyed over the observed range. So from here on we could concentrate on the determination of the universal parameters.

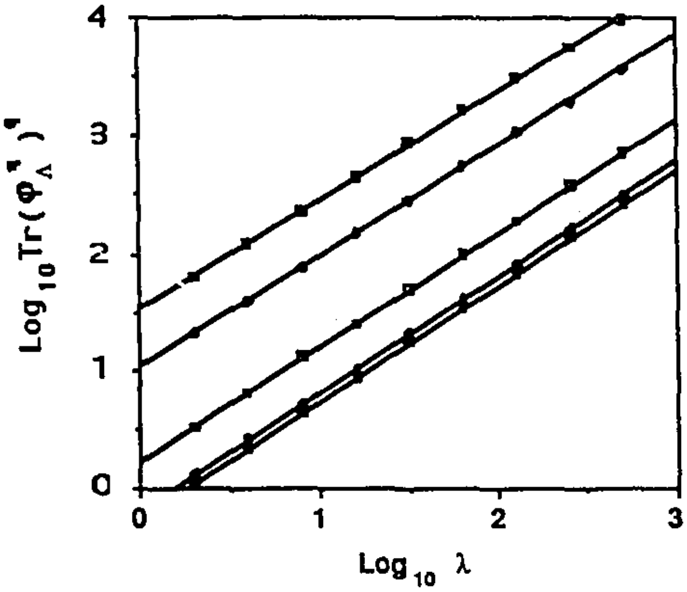

Figure 2-11: $\log\left(Tr_\lambda\left(\varphi_\Lambda^\eta\right)^q\right)$ versus $\log(\lambda)$ for several values of η (from top to bottom, η = 3.2, 2.5, 1.2, 0.35, 0.15) using q = 0.5 for the gradient of 3 images taken by LANDSAT.

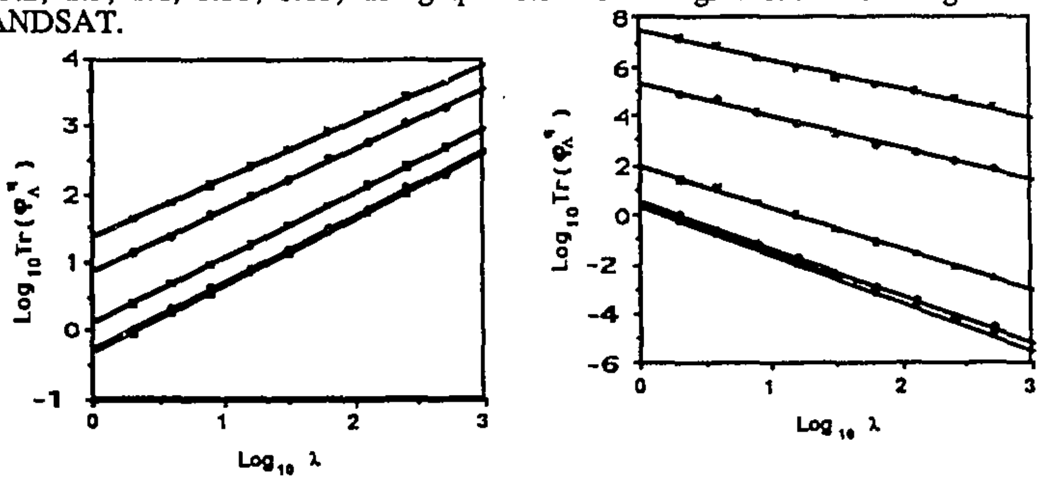

Figure 2-12: left) $\log\left(Tr_\lambda\left(\varphi_\lambda^\eta\right)^q\right)$ versus $\log(\lambda)$ for several values of η (from top to bottom, η = 3.2, 2.5, 1.2, 0.35, 0.15) using q = 0.5 for the gradient of images taken by METEOSAT in the visible. right) Same as left) but for the infra red channel and using q = 2.0

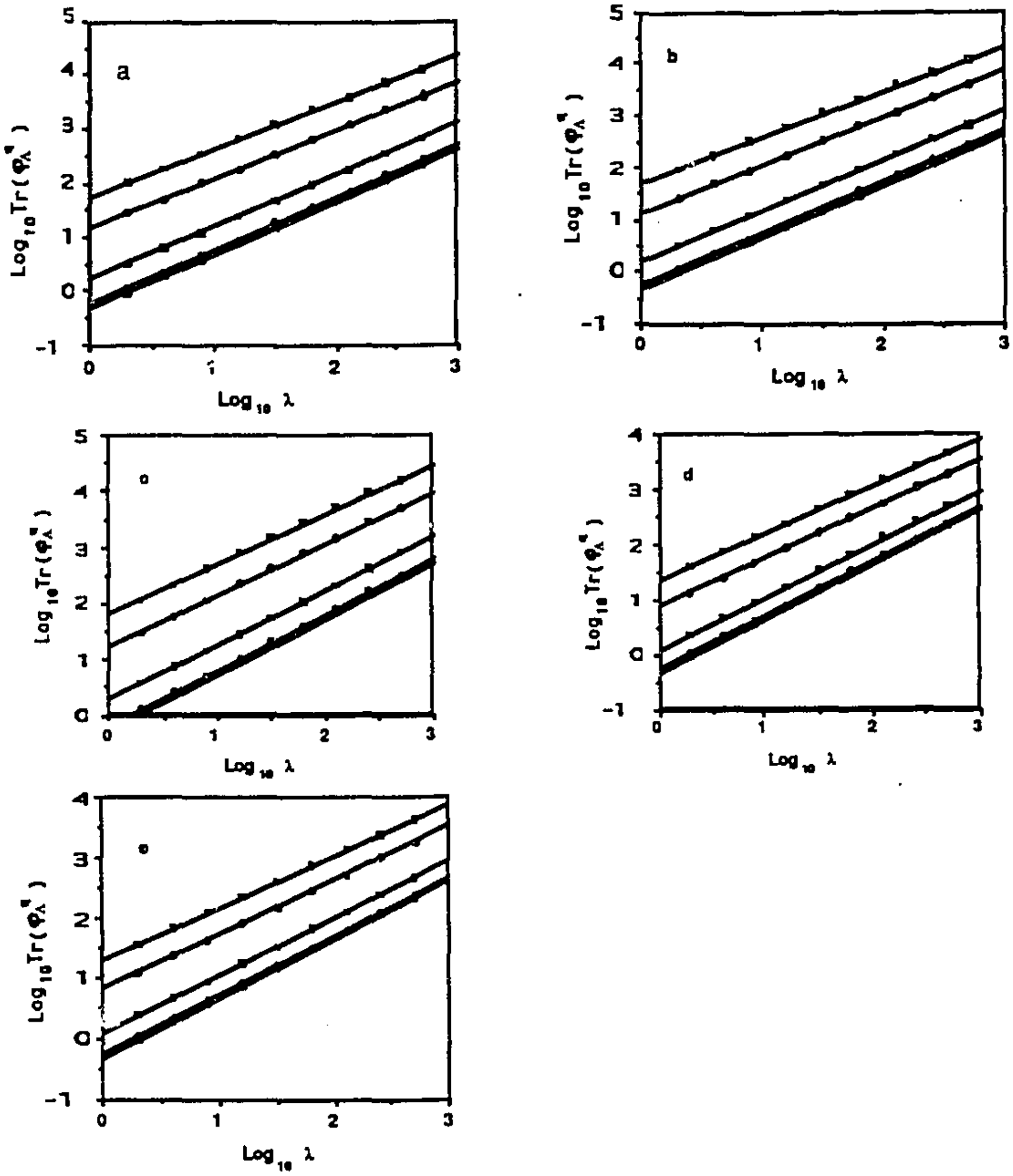

Figure 2-13: $\log\left(\mathrm{Tr}_\lambda\left(\varphi_\Lambda^\eta\right)^q\right)$ versus $\log(\lambda)$ for several values of η (from top to bottom, $\eta = 3.2, 2.5, 1.2, 0.35, 0.15$) for gradient of images of all channels of NOAA-9 AVHRR using $q = 0.5$; statistics were accumulated for 15 images. a) channel 1, b) channel 2, c) channel 3, d) channel 4, e) channel 5)

From these $\log\left(Tr_\lambda\left(\varphi_\lambda^\eta\right)^q\right)$ versus $\log(\lambda)$ curves we obtained the $\log(K(q,\eta))$ versus $\log(\eta)$ from whose slope we deduce the universal parameter α and from whose intercept with the line $\log\eta = 0$ we estimate C_1. In figure 2-14 we show a typical result for our analysis. In this case we performed the analysis on the gradient of one image and we obtained the values $\alpha = 1.3$ and $C_1 = 0.1$. The deviation from linear behavior at high values of η is due to undersampling problems, this problem should occur for values of $\max(q\eta,\eta) = \min(q_s,q_D) \approx q_s$ ($q_D > 50$ here[22]) which in this case (since only one image is used) is estimated to be

$$q_s = \left[\frac{D}{C_1}\right]^{1/\alpha} = \left[\frac{2}{0.1}\right]^{1/1.3} \approx 10 \qquad (2.26)$$

which is close to the value estimated directly on the graph: the straight line behavior breaks down at $\eta \sim 5$ ($q = 2$ here). As expected this is roughly were the curve becomes horizontal.

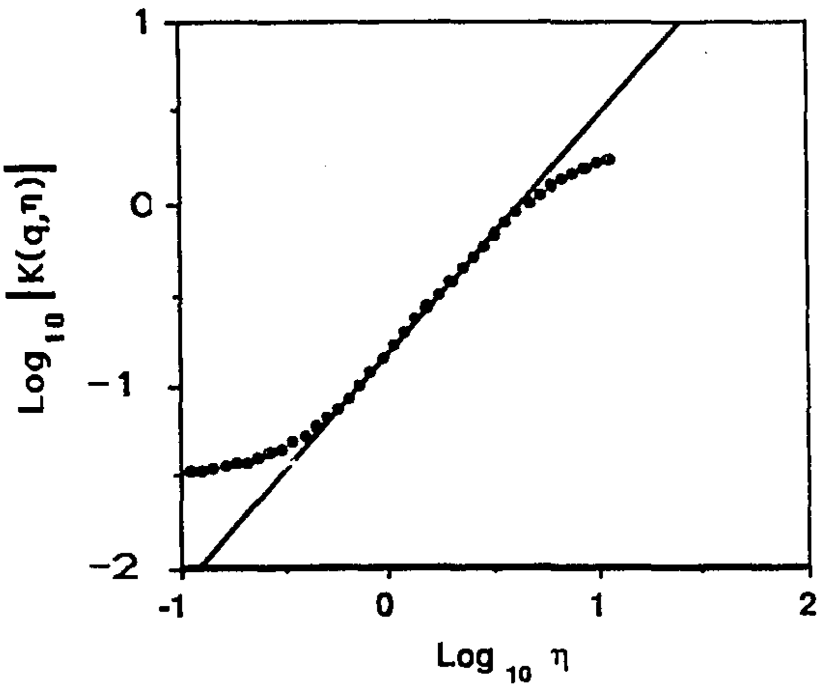

Figure 2-14: $\log(|K(q,\eta)|)$ versus $\log(\eta)$ for the gradient of an image taken by the channel 5 of NOAA-9, we used a value of $q = 2.0$ and the straight line corresponds to the regression line from which we deduce $\alpha = 1.3$ and $C_1 = 0.1$.

[22] Evaluated using D=2, recent analysis suggest it could not be the case. D may be lower thus q_D might be of the same magnitude of q_s.

For the reason given in section 3.2 (i.e., the possibility of non-conserved fields) we analyzed the modulus of the gradient and the modulus of the Laplacian of the radiance fields. As expected, both methods always gave similar results so in order to assure the reader about this fact we reproduce the resulting $\log(|K(q,\eta)|)$ versus $\log(\eta)$ for the modulus of the gradient and the modulus of the gradient of one of the analyzed images (fig. 2-15). From here on all the analyses will be performed using the gradient except where stated otherwise.

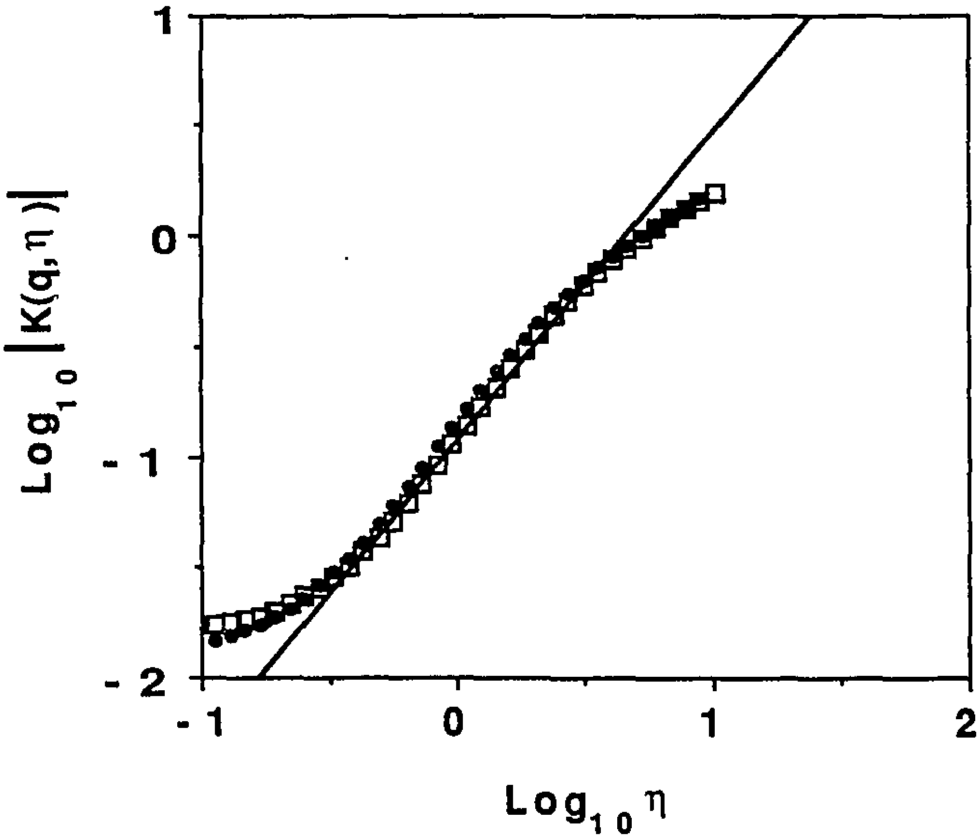

Figure 2-15: $\log(|K(q,\eta)|)$ versus $\log(\eta)$ for the Laplacian and the gradient of an image taken by the LANDSAT satellite. The filled circles are calculated using the Laplacian and for the empty squares we used the gradient. In both case $q = 2.0$. The straight line corresponds to $\alpha = 1.1$ and $C_1 = 0.1$.

Fig. 2-16 shows a plot of $\log(|K(q,\eta)|)$ versus $\log \eta$ for all the images taken in the visible wavelength channel. We can see that even if the images are covering different scales and have slightly different wavelengths there is good agreement between the different satellites. We obtain $\alpha = 1.2$ and $C_1 = 0.0.8$ for LANDSAT, $\alpha = 1.12$ and $C_1 = 0.12$ for METEOSAT and $\alpha = 1.07$ and $C_1 = 0.12$ for NOAA-9 channel 1. The break in the linear behavior for low values of η should not be interpreted as a scaling break. In this range of η the analysis is sensitive to extremely low values of the field, noise will overcome the signal leading to a deviation from the expected linear behavior. Of course, different sensors will have different noise level and this is why all the curves don't break at the same place. The next graph (figure 2-17) performs the same exercise for the thermal infra red sensors (channel 4 and 5 of NOAA-9 and METEOSAT VISSR infra red channel). The straight portions of the curves are nearly parallel and both channels of NOAA are almost on top of one another. The estimates for α are still close to one another ($\alpha = 1.21$ for METEOSAT and $\alpha = 1.35$ for NOAA-9) and the estimates for C_1 are also compatible ($C_1 = 0.17$ for METEOSAT and $C_1 = 0.09$ for NOAA-9). Table 2-2 summarize all results for the different satellites and sensors.

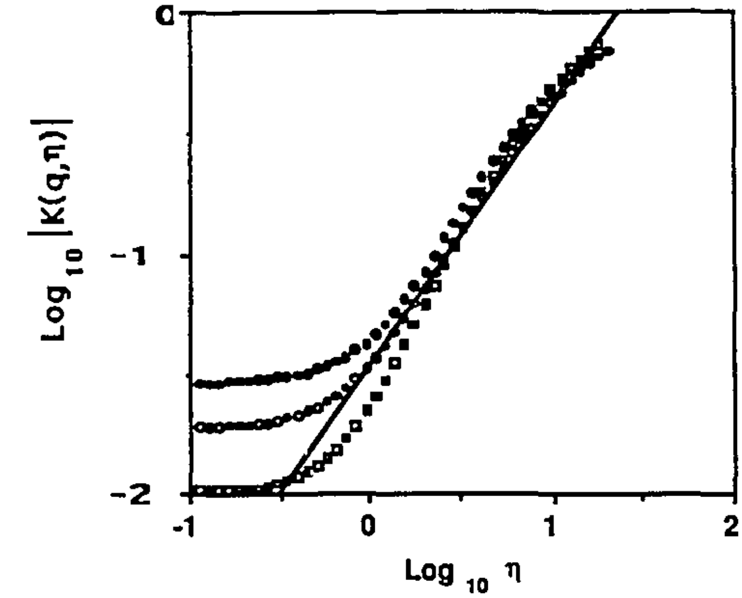

Figure 2-16: log(|K(q,η)|) versus log(η) with q = 2.0 for the gradient of all the images in the visible range. The straight line corresponds to α = 1.1 and C_1 = 0.1. The empty squares are for LANDSAT, the empty circles for NOAA-9 channel 1 and the filled circles for METEOSAT visible channel.

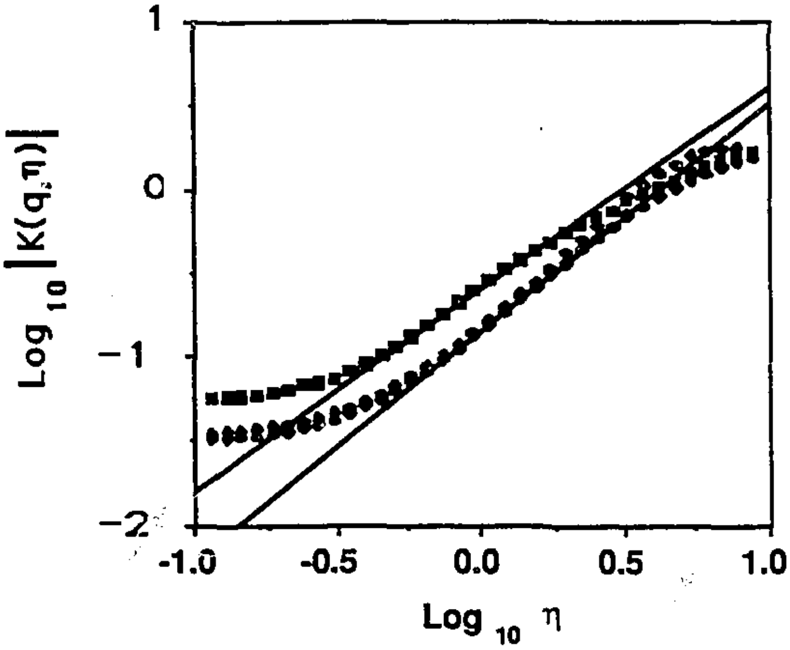

Figure 2-17: log(|K(q,η)|) versus log(η) with q = 2.0 for the gradient of images from the infra red sensors. The diamonds are for NOAA-9 pictures (empty: channel 4, filled: channel 5) and the filled squares are for METEOSAT pictures. The straight lines correspond to linear regression fit on the linear part of the curves.

Satellite	Sensor	wave-length	scaling range	α	C_1	H
NOAA 9	AVHRR channel 1	0.5 to 0.7 μm	1 to 512 km	1.13	0.09	0.4
NOAA 9	AVHRR channel 2	0.7 to 1.0 μm	1 to 512 km	1.10	0.09	0.4
NOAA 9	AVHRR channel 3	3.6 to 3.9 μm	1 to 512 km	1.11	0.07	0.3
NOAA 9	AVHRR channel 4	10.4 to 11.1 μm	1 to 512 km	1.35	0.10	0.5
NOAA 9	AVHRR channel 5	11.5 to 12.2 μm	1 to 512 km	1.35	0.10	0.5
METEOSAT	VIS	0.4 to 1.1 μm	8 km to 4000 km	1.35	0.10	0.3
METEOSAT	IR	10.5 to 12.5 μm	8 km to 4000 km	1.21	0.09	0.4
LANDSAT	MSS	0.49 to 0.61 μm	166m to 83 km	1.23	0.07	0.4

Table 2-2: The evaluated universal multifractal parameters for each group of pictures. The accuracy on the values of α is ± 0.2, on C_1 it is $\pm$ 0.1 and on H it is $\pm$ 0.2.

All the observed values for α lie between 1 and 2. Since we always obtained $\alpha > 1$, the corresponding radiance fields will be unconditionally hard multifractal processes (section 2): i.e. sufficiently high order moments will diverge when the reflectivity field is average over a space of dimension D. The critical order for divergence is given by eq. 2.13b taking D = 2 it gives values of $q_D > 50$ which is sufficiently large that it would require enormous sample sizes to be observed directly[23].

There are many possible explanations for the spread in these values. First we have to remember that these universal parameters are well defined only for ensemble average

[23] The relevant value of D may be much smaller, in which case q_D will also be much smaller, and hence the divergence detectable. This is because research in progress indicates that the relevant D may be the order of fractional integration .

quantities so that some statistical variation is certainly to be expected. For example, using numerical simulations with 25 independent one-dimensional samples with 1024 points each, Lavallée et al [59] estimated that α could be estimated to an accuracy of ~ ± 0.1 which is a rough indication of the enormous sample sizes that are theoretically required (note that what is most fundamental is the range of scales and the number of independent realizations: here $\lambda = 256$ or 512 and 3 - 5 realizations were used). Second, different satellites have different problems. For example, LANDSAT was not designed for the observation of clouds so that occasionally (<30% of the images in this case) the detector was saturated by particularly bright cloud regions (with albedo ≥ 0.45). Roughly the effect of this on the multifractal analysis is to cut off high order singularities corresponding to the saturation level. Fortunately our estimates of α and C_1 from the DTM technique mainly rely on the less extreme values (i.e., the low order moments η, $q\eta \approx 1$) near the mean and should not be badly biased. Some METEOSAT images were not completely over the ocean and it was possible to see landmasses under the clouds, so the analyzed albedo field is not purely due to clouds but in some part also to the land beneath them (which will presumably have different multifractal properties and exponents). However, since at visible wavelengths the land has much lower radiance than clouds, this will primarily affect the very low η, $q\eta$ scaling and $K(q,\eta)$ estimates, again allowing reasonable C_1, α estimates from the DTM technique.

Selection bias was avoided as much as possible. All images in our largest set (NOAA-9) were taken with the sensor centered at a longitude of 70º west and a latitude of 27.5º north. This point is situated over the Atlantic ocean, east of Florida. The 15 scenes were each taken at about 1400 ± 20 local time during the month of February 1986 (the exact dates are the 10-20, 22, 24, 25 and 27). The three LANDSAT images are part of a bigger (400 x 400 km) picture which itself was selected to have 90% cloud coverage. And the three METEOSAT images are part of a sequence taken at 1/2 hr intervals at the same location. So within each set, the images are not completely independent as we would like them to be. Clearly in the future, massive systematic analyses must be undertaken.

Another problem that might have contributed to the spread of values for α is anisotropic scaling. Both the spectra and the DTM method as implemented here are entirely isotropic analysis techniques since the resolution of the fields is degraded isotropically (e.g. by using square boxes at all scales in the DTM method). However, as shown by Pflug et al. [97] rotation and stratification of structures (due here to the Coriolis force) are important, hence more precise analyses should use generalized scale changes.

Recalling that C_1 characterizes the sparseness of the mean whereas α characterizes the rate at which the sparseness varies as we go away from the mean, we expect C_1 to be more accurately estimated than α. This is indeed the case since for C_1 the range of values observed varies between 0.07 and 0.13. Such low values of C_1 are an indication that the conserved multifractal φ is not too sparse (a space filling mean would have $C_1 = 0$). It also explains the relative success of monofractal analyses (e.g., Lovejoy [63]), since near the mean, the parameter H will provide a reasonable approximation to the scaling. However since α is fairly large (far from the monofractal value of 0), as we move away from the mean value, the monofractal approximation rapidly becomes poorer. For more discussion of monofractal cloud analyses, their limitations and biases (due to multifractal effects), see Lovejoy and Schertzer [73], especially the appendices.

II.5 The Horizontal Scaling of Rain Reflectivities

The relative success of satellite based rainfall estimation schemes (such as RAINSAT, Bellon et al [5]) --which use both radar reflectivities and rain gage measurements for ground truth-- proves that there is indeed an intimate relation between visible and infra red radiances, rain, and radar reflectivities of rain. We therefore turn our attention from the radiances to data sets more closely related to rainfall. The first such data set we studied was obtained using a scanning radar situated in Montreal. This radar provides information for 24 elevation angles, at a wavelength of 10 cm with a pulse repetition rate of 300 Hz, and a downrange resolution of 75 m. We analyzed scans during a convective storm over Montreal that took place at 22.00 EST 1 May 1992. From these scans we analyzed 256 x 256 square section images (avoiding the center and the outer limit which were biased due to ground echo and the curvature of the earth). In order to avoid ground clutter contamination we did not use the smallest elevation angles. The first analysis was the isotropic power spectrum which is shown on figure 2-18. We observe that scaling is observed on the range of 75 m to 10 km. From a linear regression we deduce that the negative spectral slope is $\beta \approx 1.45$. Figure 2-19, where it is shown $\log\left(Tr_\lambda\left(\varphi_\lambda^\eta\right)^q\right)$ vs log λ for various η, confirms that there is scaling over the entire range studied. The $\log\left(\left|K(q,\eta)\right|\right)$ vs log η curve, calculated from the previous graph is shown on figure 2-20. In this case we estimate $\alpha \approx 1.4$ and $C_1 \approx 0.12$.

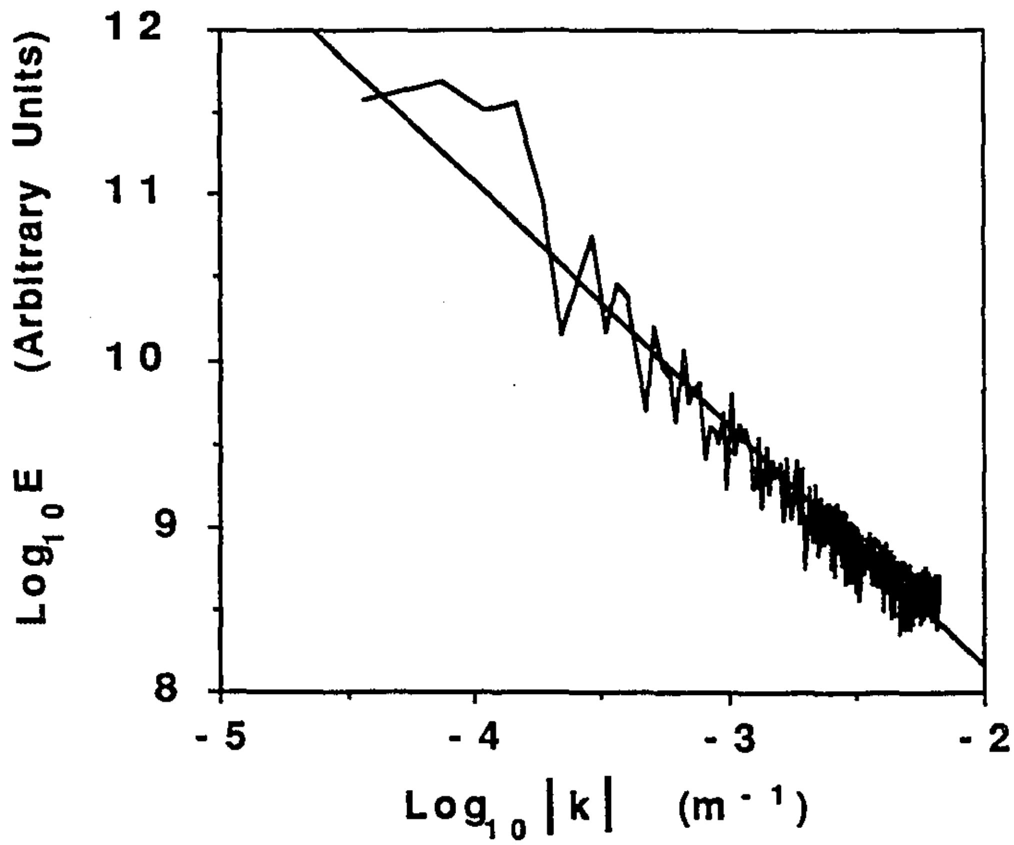

Figure 2-18: Isotropic power spectrum for radar ppi's. We included a line of slope 1.45 so that the scaling behavior is more apparent.

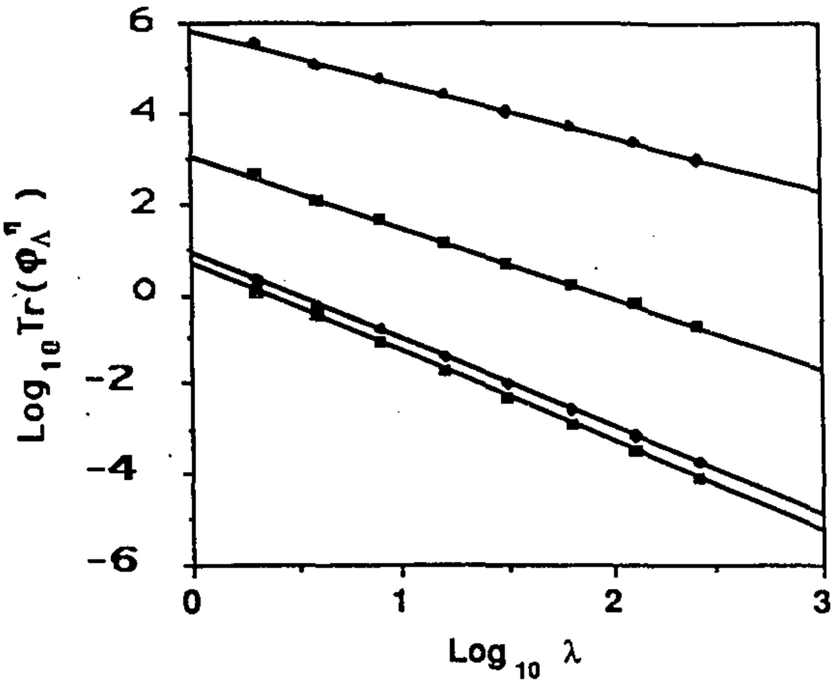

Figure 2-19: $\log\left(\mathrm{Tr}_\lambda\left(\varphi_\Lambda^\eta\right)^q\right)$ versus log(λ) for several values of η (from top to bottom, η = 2.7, 1.61, 0.4, 0.2) using q = 2.0 for the gradient of radar ppi's.

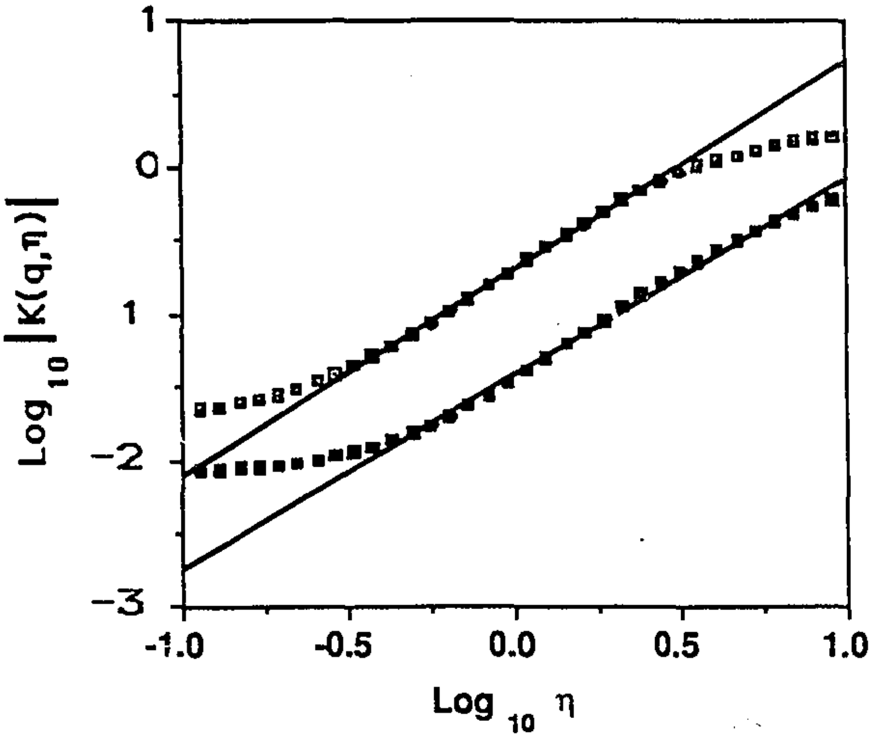

Figure 2-20: $\log(|K(q,\eta)|)$ versus log(η) with q = 2.0 (top curve) and q = 0.5 (bottom curve) for radar ppi's. The straight lines correspond to α = 1.4 and C_1 = 0.12.

II.6 . The Vertical scaling of rain reflectivities:

In the previous section we obtained an estimate of the universal parameters for the horizontal radar reflectivity field. In order to examine the vertical structure we turned our attention to another data set. The data we studied was obtained using a vertically pointing (3 cm wavelength) radar with a pulse repetition rate of 0.4 Hz. We analyzed a data set lasting for 5 hours, 41 minutes, 20 seconds (8192 consecutive pulses), with near range of 171m altitude above the radar and far range of 6958m above (in 325 equally spaced bins, 21.4 m pulse length). The vertical structure of rain reflectivities is quite different from the horizontal structure due to the strong stratification caused by gravity (Lovejoy et al [70]).

The meteorological situation involved stratiform rain ahead of the warm sector of a low. The surface temperature varied between 8°C and 10°C during the storm. There was a bright band (i.e., melting snow and ice) between 1.5 and 2.5 km altitude. A small portion of the raw data is shown in figure 2-21. When we analyzed the horizontal cloud radiances, we immediately calculated the (usual) isotropic energy spectrum obtained by integrating the Fourier square moduli over angles in Fourier space (and then estimating the ensemble average by averaging over the available data). This was natural since in the horizontal plane, the anisotropy was not too pronounced. Here the situation is quite different since a priori, the vertical and temporal characteristics of rain are very different, the (k,ω) (Fourier space, corresponding to (z,t) real space) will be quite anisotropic -- strongly stratified in the z direction (as may be seen in figure 2-22). The proper framework for analyzing this anisotropy is GSI and the related space-time transformations that are discussed more in detail in section II.5. In this section we limit ourselves to more straightforward analyses. First, we calculate lines of constant Fourier amplitudes in the two dimensional (k,ω) space (fig. 2-22). As expected, we roughly obtain ellipses whose stratification is opposite that of the real space (z,t) stratification (and increases with increasing k). The slight overall rotation corresponds to a constant advection velocity. This differential stratification corresponds to the fact that (one dimensional) temporal and (one dimensional) spatial spectra will have different spectral exponents (β_t, β_v). Indeed, the one dimensional vertical spectrum for the region below the bright band (fig. 2-23, averaged over all the pulses in time) shows $\beta_v \sim 1.4$ whereas the corresponding temporal spectrum (fig. 2-24) average over different portions corresponding to different ranges of altitudes yields $\beta_t \sim 1.2$. The break in the vertical spectrum occurs at scales of ~100 m and roughly coincides with the horizontal scale of averaging --the pulse width in the horizontal was ≈ 100m at 3 km distance. In fig. 2-22, we can see the "spheroscale" which is the scale over which the (near) elliptical contours become (near) circles indicating approximate isotropy at the corresponding scale (≈ 1 km here). The existence of a bright band limited these analyses in fig. 2-23 to a range of only a factor 64. This vertical scaling confirms that already reported using an entirely different method: "functional box-counting", Lovejoy et al. 1987 found that reflectivities of 10 stratiform and 10 cumuloform storms were fairly accurately scaling over the range 1 - 8 km.

For each pulse we calculated trace moment statistics of 64 levels below bright band levels and accumulated the statistics over the 8192 pulses. In fig. 2-25 we show the log of the trace moment of order $q = 2$ against the log of the scale ratio λ for different values of the exponent η. It can be seen that we obtained scaling over nearly 2 orders of magnitude in λ (corresponding to the high frequency scaling in fig. 2-24). In fig. 2-26 we show log $|K(q,\eta)|$ vs. log η for $q = 0.5$ and $q = 2.0$ from which we deduce $\alpha \approx 1.35$ and $C_1 \approx 0.1$.

Figure 2-21: A portion of the raw data (reflectivity for elevation against time) for the vertically pointing radar reflectivities. We show 1024 time steps by 318 vertical bins section. The gray scale is proportional to the dbZ value.

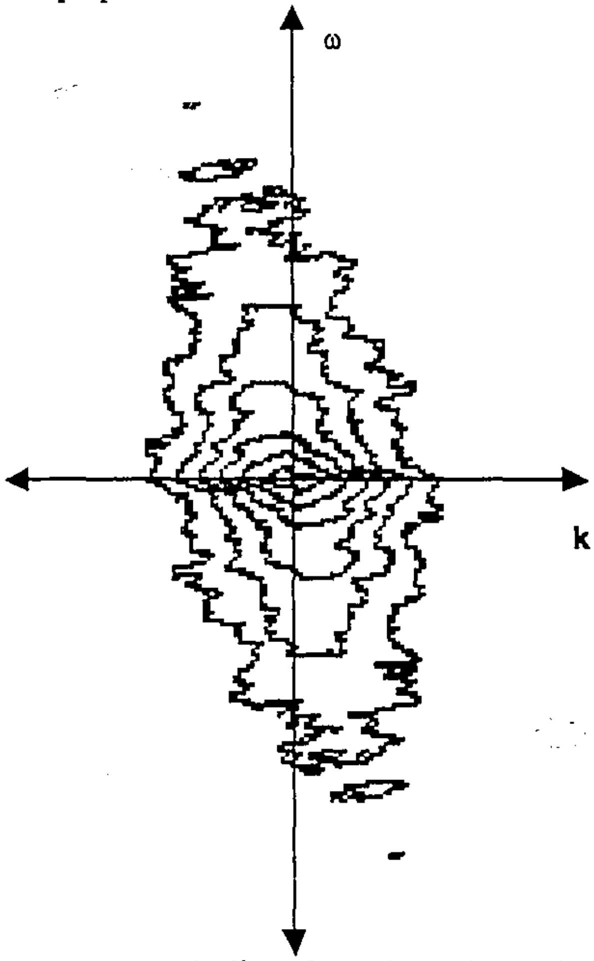

Figure 2-22: 2-D Power spectrum isolines for radar reflectivities. We can see that the isolines are highly elongated in the temporal frequency direction for high frequencies and in the spatial direction for low frequencies.

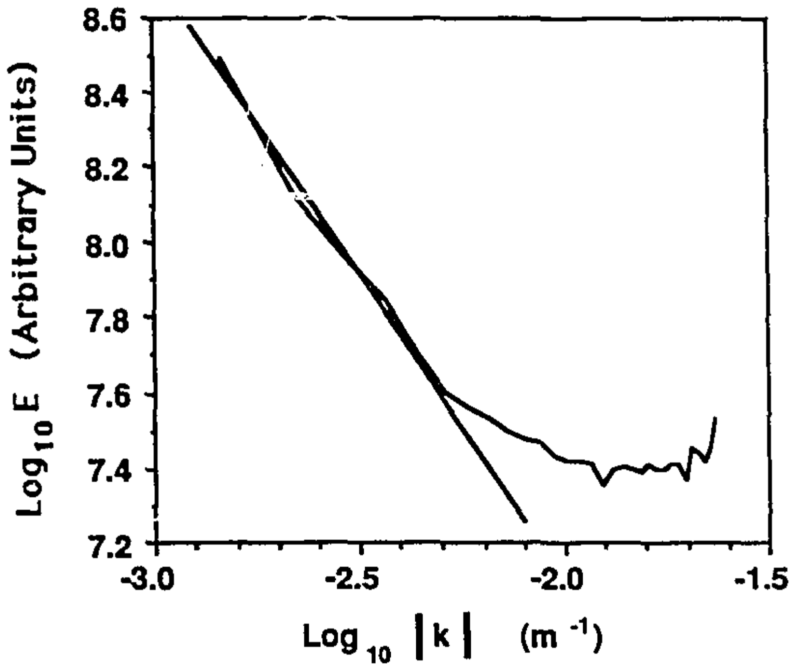

Figure 2-23: Power spectrum for the radar reflectivities against elevation. From the slope of the regression line $\beta = 1.4$.

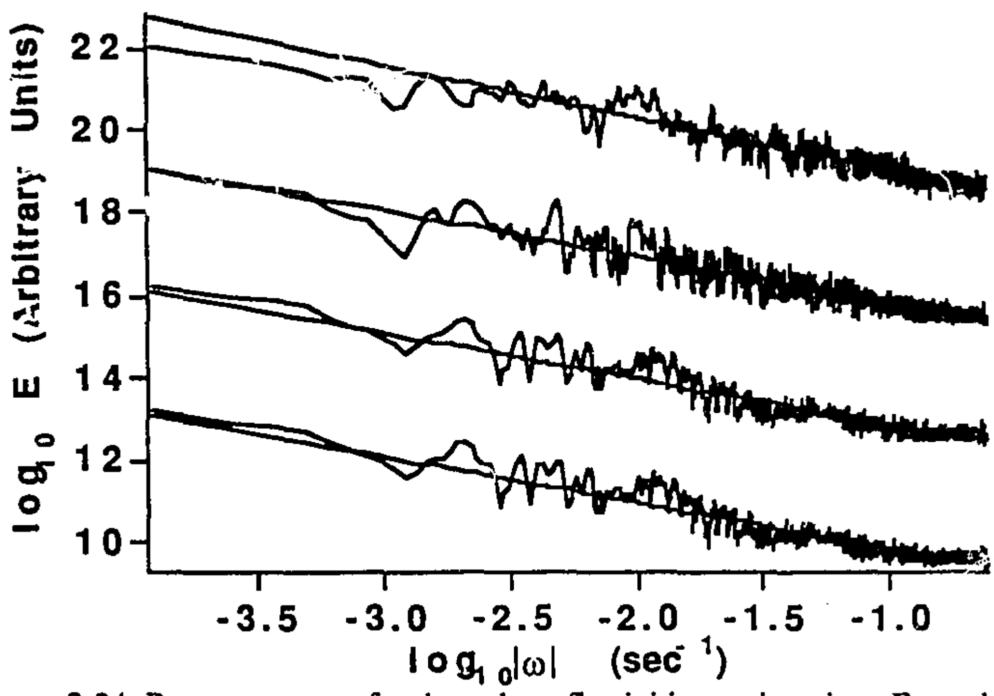

Figure 2-24: Power spectrum for the radar reflectivities against time. From the slope of the regression line we deduce $\beta = 1.2$. The bottom curve corresponds to an average for the 32 lower levels, the next one is an average of the next 32 levels (displaced by 3) and the same for the next two curves.

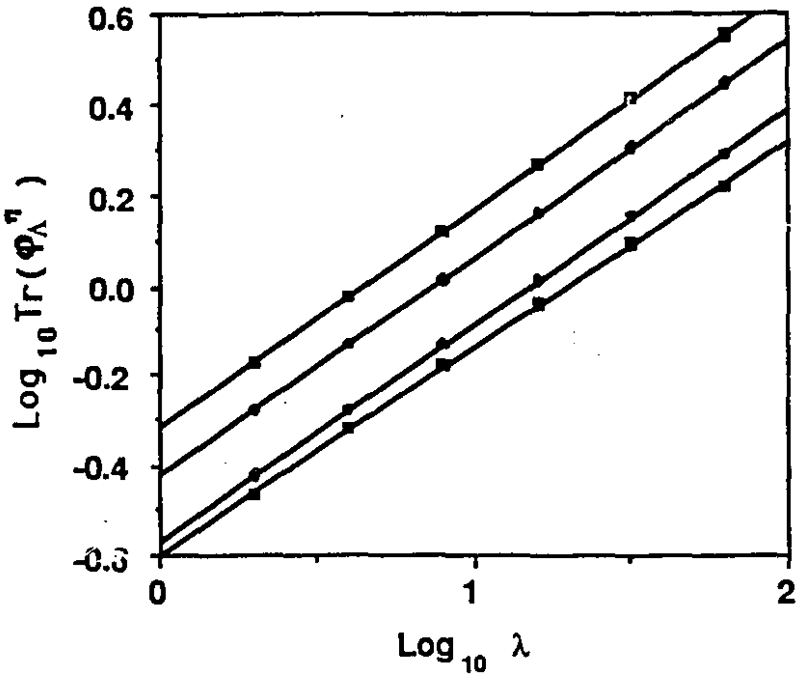

Figure 2-25: $\log\left(Tr_\lambda\left(\varphi_\lambda^\eta\right)^q\right)$ versus $\log(\lambda)$ for several values of η (from top to bottom, η = 1.2, 0.7, 0.3, 0.1) for radar reflectivities against elevation and statistics accumulated in time. We used $q = 0.5$.

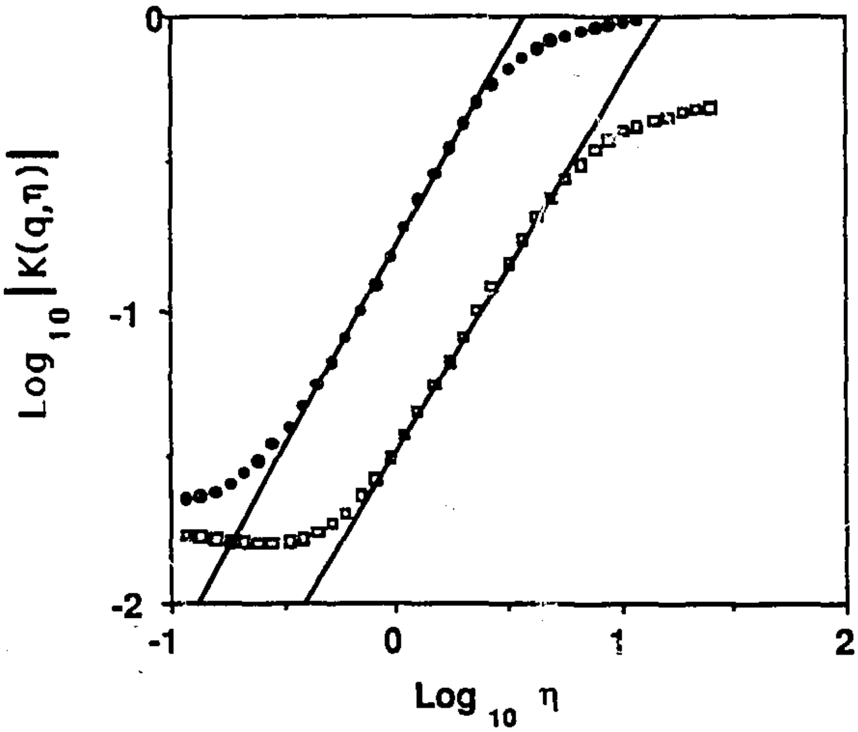

Figure 2-26: $\log(|K(q,\eta)|)$ versus $\log(\eta)$ for the radar reflectivities against elevation and statistics accumulated in time. The filled squares are for $q = 0.5$ and the empty squares are for $q = 2.0$. From the regression lines we deduce $\alpha = 1.35$ and $C_1 = 0.1$.

II.7. Isotropic (Self-Similar) Simulations of Rainfall

In this section we indicate briefly how to exploit the universality (and the measured H, C_1, α parameters) to perform multifractal simulations. The first multifractal models of this type were discussed in Schertzer and Lovejoy [109], and Wilson et al [138] gives a comprehensive discussion including many practical (numerical) details. In particular, he describes the numerical simulation of clouds and topography, including how to iteratively "zoom" in, calculating details to arbitrary resolution in selected regions. Although we will not repeat these details here, enough information has been given in the previous sections to understand how they work. First, for a conserved (stationary) multifractal process φ_λ we define the generator $\Gamma_\lambda = \log\varphi_\lambda$. To yield a multifractal φ_λ, it must be exactly a 1/f noise, i.e., its generalized spectrum is $E(k) \approx k^{-1}$ (this is necessary to ensure the multiple scaling of the moments of φ_λ). To produce such a generator, we start with a stationary gaussian or Levy "subgenerator". The subgenerator is a noise consisting of independent random variables with either gaussian (α=2) or extremal Levy distributions (characterized by the Levy index α), whose amplitude (e.g., variance in the gaussian case) is determined by C_1. The subgenerator is then fractionally integrated (power law filtered in Fourier space) to give a k^{-1} spectrum. This generator is then exponentiated to give the conserved φ_λ which will thus depend on both C_1 and α. Finally, to obtain a non conserved process with spectral slope β, the result is fractionally integrated by multiplying the Fourier transform by k^{-H} where H is given in eq. 3.8. The entire process involves two fractional integrations and hence four FFT's. 512X512 fields can easily be modeled on personal computers (they take about 3 minutes on a Mac II), and 256 x 256 x 256 fields (e.g., space-time simulations of dynamically evolving multifractal clouds) have been produced on a Cray 2 (Brenier [24][12], Brenier et al [13]).

---

[24]Such clouds simulation have been turned into a video called "Multifractal dynamics".

We performed simulations using universal multifractal parameters close to what have been observed for cloud radiances. They are shown in fig. 2-27 and 2-28. We used α = 1.35, C_1 = 0.1 and we vary the value of H because this seemed to be the most important difference between visible and infra red images. For fig 2-27 we used H = 0.3 and for fig 2-28 we used H= 0.4. For infra red images the value of H is higher giving it the smoother look that meteorologist are familiar with.

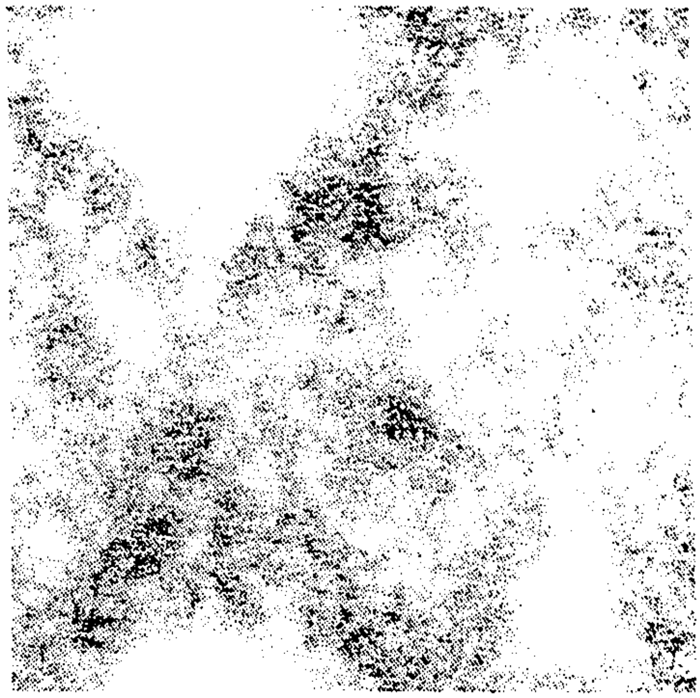

Figure 2-27: 2-D simulation using $\alpha = 1.35$, $C_1 = 0.1$ and $H = 0.3$. The values of the parameters are close to what has been estimated for cloud radiance pictures in the visible frequencies range.

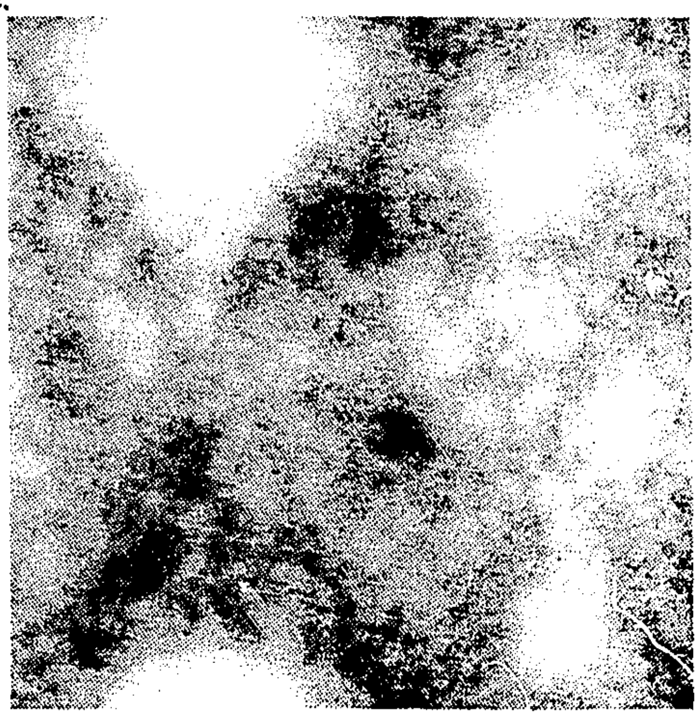

Figure 2-28: simulation using $\alpha = 1.35$, $C_1 = 0.1$ and $H = 0.4$. The values of the parameters correspond to what has been evaluated for cloud radiance pictures in the thermal infra red frequencies range.

II.8. The Multifractal Atmosphere:

We have briefly sketched some arguments in favor of unified scaling and presented some of the multifractal notions. The object was to both motivate the various empirical analyses which followed, as well as to explain the ideas in sufficient detail so that the workings of the new Double Trace Moment (DTM) analysis technique could be grasped. This technique is the first to be designed to directly estimate the universal multifractal parameters; it is considerably more statistically robust than previously existing analysis methods, and it applies not only to "calm" multifractals (of the sort associated with strange attractors), but also to the "hard" (extremely variable) multifractals found in geophysics (indeed, we quantitatively confirm the "hard" nature of the cloud radiances and rain reflectivities).

We applied not only the DTM, but also conventional energy spectra to analyze satellite cloud radiances from LANDSAT, NOAA-9, and METEOSAT satellites in the visible, near IR, and thermal IR wavelengths. Overall, the data sets spanned the range 166m to ≈4000 km; and were found to be scaling through the entire region, including the mesoscale. Although we conclude that the evidence for horizontal scaling is good it should be stressed that enormous, systematically sampled data sets will be needed to fully characterize the scaling of atmospheric fields as well as the corresponding inner and outer limits. This study only provides an early exploration of what is largely unknown territory.

Moving on from the horizontal scaling of cloud radiances, we analyze data from a vertically pointing radar measuring reflectivities of rain with a resolution of 2.5 seconds in time, 21m in space. In the vertical, the scaling was followed at high frequencies, but we found a spectral bump corresponding in size (≈1 km) to the thickness of the bright band which was present throughout the sequence. Since other studies with larger samples (e.g., 20 cases instead of one) found vertical scaling over the corresponding range, the bump is likely to be consistent with statistical (sample to sample) fluctuations.

Finally, we sketched how our empirically determined multifractal exponents, combined with appropriate space/time transformations can enable us to make dynamical multifractal simulations. These simulations will be necessary to further our understanding of the underlying atmospheric dynamics. They will help us tame the ubiquitous extreme atmospheric variability, and may have far reaching implications for remote sensing, objective analysis, and (stochastic) forecasting.

Chapter III

Multifractal Objective Analysis and Global Rainfall

In every objective analysis technique a common goal is to obtain information on a field sensed by an in situ measuring network. Meteorological data sets gathered from such networks, have many problems due to both their spatial resolutions and their heterogeneity (sparseness). In particular, observations are not homogeneously distributed around the planet and leave large geographical gaps where no data are available. Furthermore, conventional in situ observations are not truly point measurements since there is usually a certain amount of spatial averaging (even if on a very small scale) and there is also a significant amount of temporal averaging which -- due to the relation between spatial and temporal statistics -- smoothes out sufficiently small spatial variations and is essentially equivalent to spatial averaging. This finite resolution is rarely explicitly considered. The variability of the meteorological fields is considered to be essentially independent of the spatial resolution of the measurements. Multifractals specifically address these finite resolution and large variability problems, this is the basic motivation of the analyses performed in this chapter.

III.1. Critical review of Objective Analysis Methods:

In his historical outline Daley [21] explains that the advance of Numerical Weather forecasts required efficient methods of obtaining information at certain locations in order to initialize their models based on primitive equations. This was first done by dressing up synoptic charts where from known data trained meteorologists could trace all kinds of isolines according to their judgment. These subjective maps were then digitized and entered into the computer model. This time consuming task called for robust procedures to estimate the atmospheric dependent variables on regular two or three dimensional grids. Furthermore, the subjective element had to be eliminated since the analysis should not rely on know-how. The research field devoted to the development of such techniques came to be known as objective analysis.

The first techniques that were developed considered the analyzed fields as being deterministic. The problem was to minimize the effect of random measurements errors. For this reason, we will refer to these as deterministic techniques, even though statistical techniques are used to minimize the errors.

In fact, the first and simplest technique even predates the first numerical forecast experiments of Richardson (1922) [103]. The method is known as Thiessen's polygons (Thiessen, 1911 [132]). The purpose of the method was mainly to get a rough estimate of the amount of water received by a region in order to design proper drainage equipment. Polygons are defined by the mediatrix of the segments joining neighboring stations and the amount of rain is considered uniform within a polygon. If the total amount of rain over a region is desired then the precipitation heights are weighted by the area of the polygons, so the total precipitation over an area is given by:

$$P = \frac{\sum_i s_i h_i}{A} \tag{3.1}$$

where s_i is the surface of the i^{th} polygon with a precipitation height h_i and A is the total area of the region of interest. This method is still widely used in hydrology; for example, Diskin (1970) [25] proposed an automated version of this method.

Another old and simple technique is the arithmetic mean which assumes that the rainfall depth is constant over a certain region and the amount is simply the arithmetic mean of all the measurements inside that region.

A more refined method was proposed by Panofsky [92]. He performed a polynomial least squares fit that would englobe all the data points in a certain area. Some improvements to this method were done by Gilchrist and Cressman [37] by making the fit locally; i.e. polynomials were fitted to all observations in a local region surrounding each gridpoint. The polynomial fit methods have the shortcoming of generating uncontrolled oscillations.

Another class of deterministic techniques is known as the weighted interpolation methods. In these methods, a value is obtained for the missing data using a weighted average of the surrounding data values. i.e.

$$\hat{z}(r_0) = \frac{\sum_{i=1}^{N} b_i W(r_i)}{\sum_{i=1}^{N} W(r_i)} \tag{3.2}$$

where $\hat{z}(r_0)$ is the estimated value at the point x_0, $W(r_i)$ is the weighting function applied to a station i a distance r_i from x_0. The b_i are the weights obtained by least squares fittings of the function W(r) with the available data. Various functional forms were tested. For example Cressman [19] used the function

$$W(r) = \frac{R^2 - r^2}{R^2 + r^2}; \quad r = |x_0 - x_i|; \quad W(r) = 0 \quad r > R \tag{3.3}$$

where R is some arbitrarily defined range of action (the distance at which the function goes to zero). Other functional forms have been tried by MacCraken and Sauter [76], Hovland et al [44], Endlich and Mancuso [29] and others. A survey of these techniques applied to wind and concentration fields can be found in Goodin et al [40].

These regression methods assumed gaussian distributions of the residues as well as certain smoothness and analyticity properties of the field that are absent in the analyzed data. Methods which exactly fit all data points were believed to be a solution to the poor performance of the previous techniques. In this direction, the most sophisticated method we will present is the spline surface fitting. The method consists in finding the surface s(r), interpolating the observed points i.e. $s(r_i) = z(r_i)$ i = 1, 2,.......N and minimizing the functional $\int_\Omega [\nabla s(r)]^2 dr$ over the domain Ω (it is a first approximation of the average curvature or of the bending energy of a thin elastic sheet). Apart from the computational problems this technique provides artificially smooth surfaces that were not acceptable. Further details on this method can be found in Duchon [26] and Wahba [134].

To remedy to the problem it was proposed that instead of relying on an arbitrary choice of surface type and optimality condition that the field should be considered as a realization of a random process and an optimal estimate of missing data would be performed by minimizing a quantity such as the variance. This leads to what are called statistical methods. Two methods for performing statistical linear interpolation have been developed and are widely used. They both try to estimate a missing value $\hat{z}(r_0)$ with a relation of the form:

$$\hat{z}(r_0) = \sum_{i=1}^{N} b_i z(r_i) \tag{3.4}$$

The difference in the two methods resides in the way the weights b_k are obtained. For Gandin's method (Gandin [36]) they are found by solving :

$$\sum_{i=1}^{N} b_i C(r_i, r_j) = C(r_j, r_0) \quad j = 1,\ldots\ldots,N \tag{3.5}$$

$$\text{with } C(r_i, r_j) = E\left[z(r_i) z(r_j)\right] \text{ i.e. the covariance}$$

Since the correlation between the point where an estimate is desired and the measured points is generally unknown assumptions of homogeneity and isotropy are generally made i.e. $C(r_i, r_j) = C(|r_i - r_j|)$, the correlation depends only on the distance between the stations. A correlation function can then be fitted empirically from the known data points and used for the interpolation.

Another condition that must be satisfied is that in order to get an unbiased estimator $(E(z(r_0)) = E(\hat{z}(r_0)))$ there should either be a constraint on the b_i or the expectation $E(z(r)) = 0$. For Gandin's method this condition is usually satisfied by using deviations from the climatological average rather than the actual field.

Putting the constraint on the b_i bears another name: Kriging (Matheron [81, 82], Ricardo [102]). It also starts with equation (3.4) but the constraint is replaced by:

$$\sum_{i=1}^{N} b_i C(r_i, r_j) + \nu = C(r_j, r_0) \sum_{i=1}^{N} b_i = 1 \tag{3.6}$$

where ν is a Lagrange multiplier. The variance estimator is generally replaced by the semi-variogram:

$$\gamma(r_i, r_j) = \frac{1}{2}E\left[\left(z(r_i) - z(r_j)\right)^2\right] \tag{3.7}$$

then it is postulated that the semi-variogram is only a function of the distance, i.e.

$$\gamma(r_i, r_j) = \gamma(|r_i - r_j|) \tag{3.8}$$

It is called the weak stationarity or "intrinsic" hypothesis.

In order to include slow but systematic variations assumed to break the translational invariance (such as orographic[1] effects), the interpolated field can be split in a stochastic component with known spatial covariance plus a stochastic trend that can be modeled using orthogonal functions (typically, a low order polynomial function of the location variable is used). Not surprisingly, since these methods are basically linear interpolation, they will result in fields much smoother than we would expect for multifractals.

Another method that has been used is the empirical orthogonal function (EOF)[2] method which consists of expanding the random process in a linear combination of orthogonal eigenfunctions φ_ℓ:

$$z(r) = \sum_{\ell=1}^{\infty} Y_\ell \varphi_\ell(r) \tag{3.9}$$

For orthogonal function on a finite domain [a,b] and uncorrelated coefficient, these eigenfunctions have to satisfy a homogeneous Fredholm integral equation that can be solved numerically:

$$\int_\Omega C(r,r')\varphi_\ell(r)dr = \mu_\ell \varphi_\ell(r') \tag{3.10}$$

where C(r, r') is the correlation function of the process.

An estimate of missing data points can be obtained using truncated expansions:

$$\hat{z}(r_0) = \sum_{\ell=1}^{M} Y_\ell \varphi_\ell(r_0) \tag{3.11}$$

[1] Systematic variation with altitude. This is particularly important for mountainous regions.
[2] In one dimension, this technique is named the Karhunen-Loeve expansion. It is explained in Davenport and Root [22], Obukhov [88] and Papoulis [93].

Creutin and Obled [20] tested most of these methods[3] for rainfall and came to the conclusion that the best method is Gandin's method since methods like Kriging or the EOF technique did not perform significantly better but are more difficult to implement.

A basic problem encountered with even the most advanced "statistical" methods of investigation of objective analysis is that the grid, the measuring network, and the measured phenomena are all strongly variable with heterogeneities down to very small scales. This strong sub resolution variability leads to resolution dependencies that we have argued to be nearly power law (scaling) functions of the resolution. Due to the rapid advances in scaling notions in the last ten years -- especially the possibility that scale invariance is a fundamental and unifying geophysical symmetry principle -- it is urgent to replace many of the hypotheses such as regularity (non-scaling) and statistical homogeneity, by scaling (inhomogeneity) assumptions. Our effort is to develop techniques that respect both the scaling symmetries of the network as well as of the phenomenon being measured. Contrary to the usual methods, there is no need to smooth the original field and there are no artificial assumptions of "regularity", differentiability, etc.

In this chapter, we will present the entire analysis and correction procedure somewhat differently, assuming that the observed field is simply the product of a multifractal station density field and a multifractal rain rate field. We will examine the statistical properties of rainfall; the parameters we estimate are ensemble averaged quantities, they will vary considerably from one individual realization to another. Although we won't make any attempt at estimating the field at locations where measurements were not made (leaving it for future developments) we will obtain extensive statistical information about the spatial variability of the rainfield corrected for measurement bias. In our view such knowledge must precede the choice and implementation of any interpolation scheme because it must be adapted to the variability of both the sensed field and the measuring network.

---

[3] Other reviews could be found in Thiébaux and Pedder, [131] and Bras and Rodriguez-Iturbe, [10].

III.2 Analysis of The Measuring Network

III.2.1 Monofractal Analysis of a Raingage network:

When we examine the distribution of stations that reported daily rainfall accumulation for the synoptic stations archived at the National Meteorological Center (NMC) of the National Oceanographic and Atmospheric Administration (NOAA) during 1983 (figure 3-1) it is clear that this distribution is far from being homogeneous: in fact -- not surprisingly -- the inhomogeneity of the network is highly correlated with landmasses and economics.

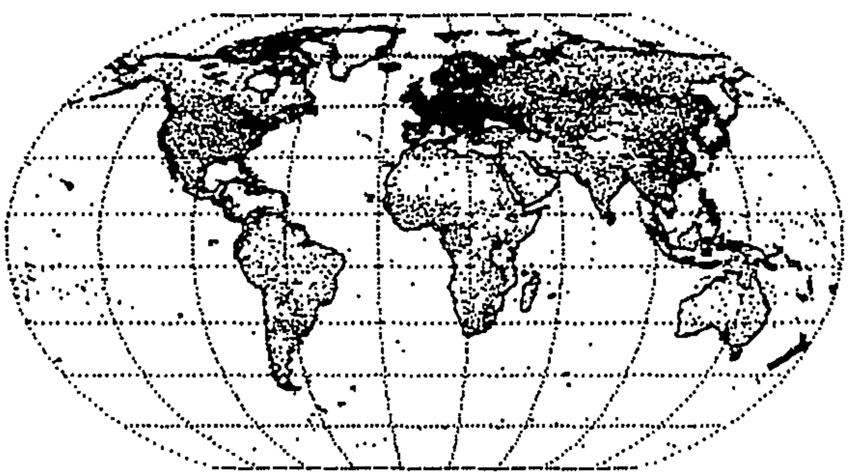

Figure 3-1: Position of the stations reporting daily rainfall accumulations in 1983 that have been used in our analysis. We also plotted the continent layouts for reference.

Lovejoy et al [68] performed monofractal analyses of the scaling properties of the World Meteorological Organization (WMO) network, showing that the scaling was fairly well respected over the range of 1 to 5000 km which was nearly the maximum possible given the finite sample size (only ~9600 stations were available). They calculated the average number of stations in a circle of radius L surrounding each station and found scaling (power) laws with exponent D ≈ 1.75 being the "correlation dimension" of the network. Montariol and Giraud [39] studied the US. Synoptic and Climatic network (excluding Hawaii and Alaska). They went beyond this monofractal framework and calculated multifractal dimensions associated with statistical moments of the station density. In a first attempt to study rainfall as sensed by a network they calculated the dimensions of the subset of stations that observed rainfall on a particular day.

A common definition of the dimension D_m of a set is given by the variation of the number of points <n(L)> with the size of the region (L): $\langle n(L)\rangle \propto L^{D_m}$. If the region is centered uniformly with respect to the set, D_m is the box dimension, if the regions are centered on points on the set, D_m is the correlation dimension. Because of the "bias" introduced in the latter, the correlation and box dimensions will not generally be identical (the latter is necessarily ≥ the former). The estimate of fractal dimensions is usually performed on flat surfaces, but the earth is not flat. To account for the curvature of the earth we must choose a method of defining scales. We do it in the following manner: if the planet (a perfect sphere) is covered uniformly with stations in an area S, then <n(L)> ∝ S. Taking $S(\theta)$ as the area of the spherical cap defined by 2 points subtending an angle θ at the earth's center (radius r). The scale $L(\theta)$ may be defined as:

$$L(\Theta) = \left[\frac{4}{\pi}S(\Theta)\right]^{1/2} = \left[2\pi r^2(1-\cos(\Theta))\right]^{1/2} \tag{3.12}$$

This definition used by Lovejoy et al [68] reduces to the usual great circle distance ($=r\theta$) for small θ, and has the required property that the dimension of an homogeneously distributed network has the fractal dimension $D_m = 2$. An estimate of the fractal dimension D_m, the correlation dimension, is obtained by estimating the average number of pairs within a certain distance L (showed in fig. 3-2).

Performing the same analysis as Lovejoy et al. [68] we observed scaling over roughly the same range (1 to 5000 km) and the dimension obtained is also almost the same (they obtained ≈ 1.75 and we got 1.79). It is expected that there will be some difference in both dimensions since they studied the WMO network (9563 stations). The network we analyzed contains 7983 stations. Apart from the fact that both networks follow similar geographic and economic constraint for their location, most of the stations are parts of both networks[4]. This explains the similarity in the correlation dimension of the two networks.

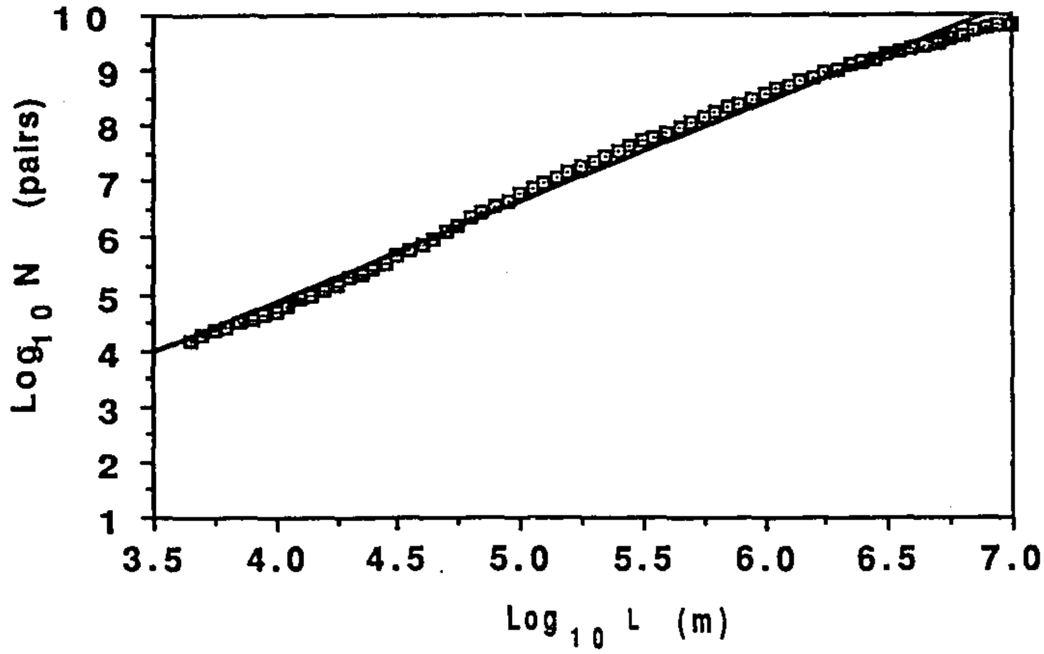

Figure 3-2: Log of number of pairs of stations against the log of the distance between two stations. The solid line is the best mean square regression line fitting the data, the slope of this line gives the correlation dimension of the rain gauge network.

The estimate of the fractal dimension of experimental data is usually carried out by box-counting, a technique that consists in covering the embedding space into non-overlapping boxes of size L, and counting the number of boxes containing at least 1 point belonging to the set under study, repeating this for different values of L. Since $N \sim L^{-D}$ the absolute slope of the log(N) vs. log(L) curve gives the fractal dimension.

The box-counting and correlation methods have different advantages and disadvantages. The fundamental difference between the two is that the correlation method involves frequent sampling of rain near clusters of stations; in this sense it is biased. In comparison, box-counting uniformly samples space since the boxes form a disjoint covering. Another difference is that with correlation methods it is easier to take into account the earth's curvature than with boxes or grids. This makes it more sensitive to low probability events because on a fractal it is more likely that a point belonging to the

[4] Unfortunately we have no quantitative informations on this.

fractal will be near another point on it than a point taken at random. In this way it makes more intensive use of the data than box-counting. The main disadvantage to the correlation method is that we have to remove this bias from the analysis.

III.2.2 Multifractal Analysis of the network:

(Mono) fractal techniques consider the measuring network as a geometric set of points. The significant advances were the recognition that the exact positions of the individual stations not the fundamental problem and the introduction of the scaling hypothesis. However, only one exponent was used to describe the scaling (the scaling of every statistical moment was expected to be derivable from it, it proved to be a particular case). With multifractals, the quantity of interest is the number density of measuring stations. We will empirically show that it is approximately a scale invariant measure underlying the actual station locations. This treatment of the stations is similar to that used in the characterization of strange attractors where the multifractal probability measure defines the probability of finding the system in a given state is stable under a change of initial conditions but the detailed distribution of points on the flow or mapping may vary a lot from one realization to another. Here an infinity of exponents (a scaling function) is needed to characterize the scaling behavior, one for each statistical moment.

III.2.2.1 Power Spectrum:

In order to get a good idea of the limits of the scaling regime, the first step we take when performing any of the analysis presented in the following sections of this chapter is to estimate the (isotropic) energy (power) spectrum which is the modulus squared of the Fourier amplitudes integrated over all angles in Fourier space and ensemble averaged over all realizations of the process. Since the field for the density of stations is distributed on a sphere we should really use a decomposition into spherical harmonics rather than

Fourier analysis, however for simplicity, we chose to perform the analysis on equal area projections of portions of the earth and use Fourier spectra. For each projection we generated 10 maps of 8000 by 8000 km sections of the earth (5 in the northern hemisphere and 5 in the southern) centered 72º of longitude apart. We then averaged the power spectrum of all the sections. One of these results is shown in figure 3-3. On this figure we see that there is a region in the low frequency range that could be fitted fairly well by a straight line. This indicates that scaling is respected in the range of 200 to 8000 km. For all the projections tested (Mercator, Aitoff, Sinusoidal), the scaling region is the same (as it should be) and the slope of the best fitting straight line in this region (the spectral slope β) is 0.63 ± 0.13. This value will be used to determine the multifractal parameter H after the other parameters have been determined by other methods. The regular oscillations in the power spectrum seem to be caused by a large localized concentration of stations in real space.

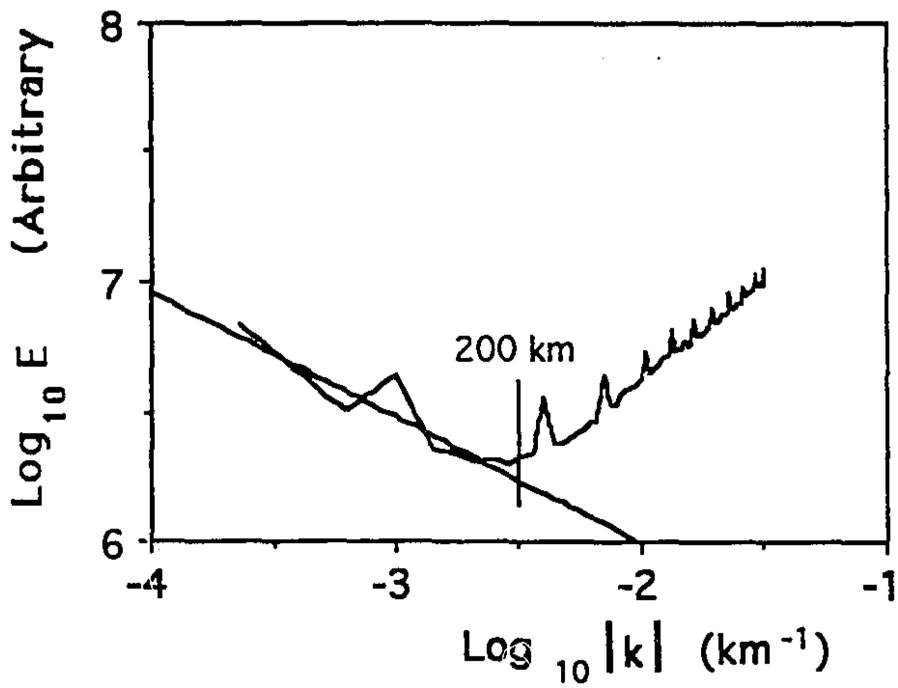

Figure 3-3: Power spectrum for the density of station field using the Aitoff equal area projection.

III.2.2.2 Probability Distribution / Multiple Scaling:

This approach is an effort to apply directly eq. 3.13 which is a fundamental property of multifractal fields. We desire to obtain directly the $c(\gamma)$ from histograms using the "Probability Distribution Multiple Scaling" (PDMS) technique, (Lavallée et al. [60]) and from there estimate the universal multifractal parameters.

The method is based on:

$$\Pr\left(R_\lambda > \lambda^\gamma\right) \approx \lambda^{-c(\gamma)} \tag{3.13}$$

and consists in plotting log Pr vs log λ for γ constant. In this manner it accounts for the non unity prefactors in equation (3.13).

We partition the globe with a 256x256 grid using the sinusoidal (equal area) projection, estimated the density of stations in each grid element and from there we estimated the different probabilities. Some of the log Pr vs log λ curves are presented in fig. 3-4. We see that good scaling is observed for $0 \leq \log \lambda \leq 2.0$ (i.e. from 200 km to 20 000 km). $c(\gamma)$ is obtained from the slope of these lines and are reported on fig. 3-5.

We could already note that for high values of γ, instead of following universal relations we observe a linear behavior that is associated with a first order multifractal phase transition will be explained in the next section. The straight line for large γ's has a slope of $q_D = 3.6 \pm 0.1$ as expected. A value close to this one ($q_D = 3.7 \pm 0.1$) is observed on the histograms. On fig. 3-6 we show $\log_{10} \Pr(\rho_\lambda > P)$ vs $\log_{10} P$, P being the threshold density. For this figure we used $\approx$ 800 km x 800 km grid elements (which is well within the scaling range).

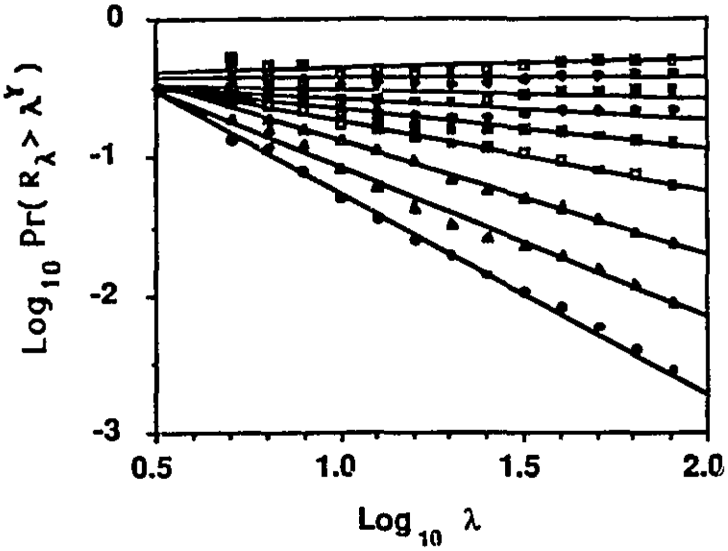

Figure 3-4: PDMS analysis on the network. Log of the probability against the log of the scale ratio λ for different values of the singularity order γ varying in steps of 0.1 from $\gamma = 0$ (empty squares) to $\gamma = 0.8$ (filled circles).

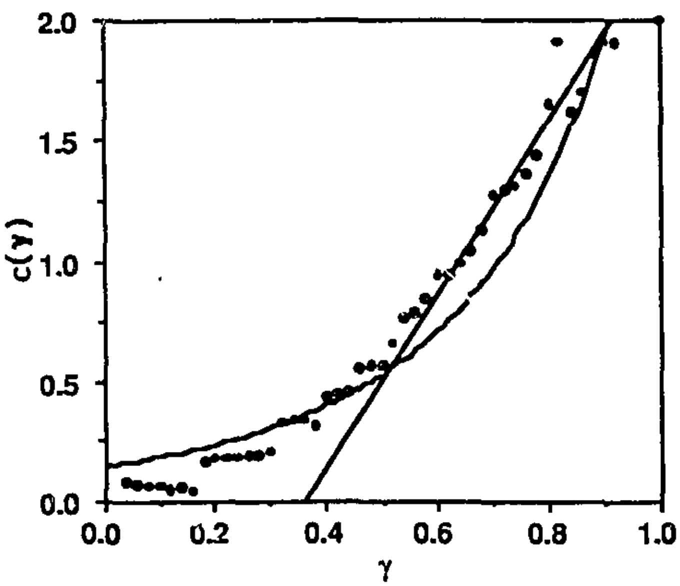

Figure 3-5: $c(\gamma)$ vs. γ for the network deduced from the previous graph as well as a theoretical curve with the parameter obtained by the DTM technique (solid line); i.e. $\alpha = 0.85$ $C_1 = 0.37$ and $H = 0$. The straight line has a slope $q_D = 3.6 \pm 0.1$.

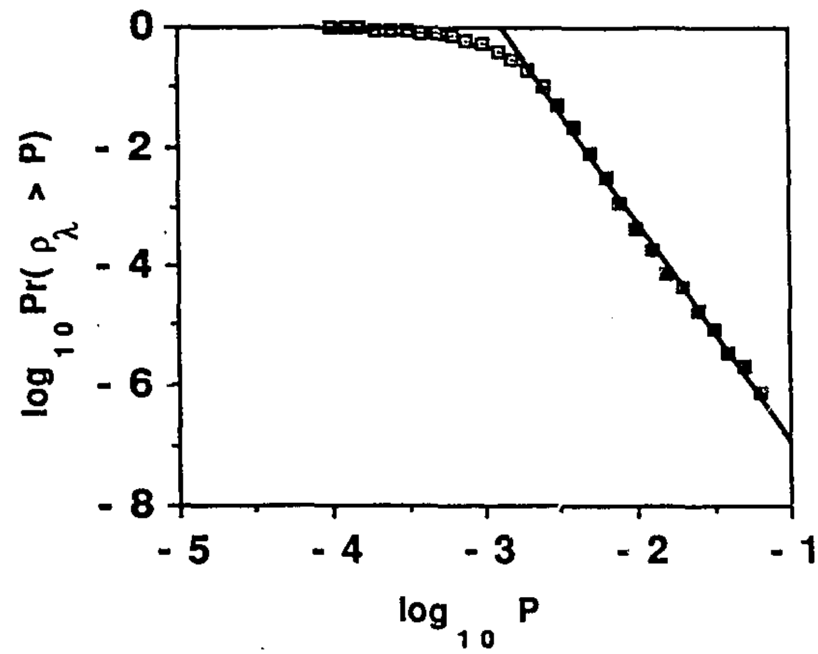

Figure 3-6: log of the probability of finding a density of station greater than ρ in a circle of 800 km against log ρ. The asymptotic slope gives directly the exponent q_D that we estimate to be 3.7±0.1.

In order to estimate the different universal multifractal parameters we tried to fit eq (2.11) with the data of fig. 3-5. Non-linear curve fitting algorithms such as the Levenberg-Marquant [98] or the simplex method [126] failed badly to converge to a solution. The regressions problems are very likely due to the high degree of correlation between the parameters and the limited range of γs accessible to our analysis. The theoretical curve shown on the same figure was calculated using the parameters obtained with the double trace moment technique. A method that we used in the previous chapter and the results on this particular field will be presented in section II.2.2.5.

III.2.2.3 Sampling limits, detectability and Multifractal Phase transitions:

The scaling exponent functions have analogs in thermodynamics (Tél [127], Shuster [122], Schertzer et al [117]). The probability description (γ, c(γ)) is the multifractal analog of the (energy, entropy) description of standard thermodynamics and the moment description (q, K(q)) is the analog of the (inverse temperature, Massieu Potential) description. Discontinuities in these functions (phase transitions) could be caused by two different statistical mechanisms (these are very different from the "high temperature" transitions discussed in relation to strange attractors). Finite sample sizes give rise to second order transitions. First order phase transitions (discontinuities in the first derivative of moments function) occurs for larger samples and are due to divergence of moments that take place when a cascade process is observed at a scale larger than its homogeneity scale (the smallest scale used in building the process), i.e. it appends for dressed cascade processes.

When an investigation of a multifractal process is performed we will typically have N_S independent realizations, each of dimension D and each covering a range of scales λ. With more realizations (increased N_S) a larger portion of the probability space will be explored. Thus, extreme but rare events that were missed with a smaller sample will be encountered. The extent of the portion of the probability space sampled can be quantified by the sampling dimension D_S (Schertzer and Lovejoy [114], Lavallée et al [60]). From eq. (3.13) and using the fact that there are a total of $N \bullet N_S = \lambda^{D+D_S}$ structures in the sample, the dimension corresponding to the highest order of singularity likely observed with N_S independent realizations is given by:

$$c(\gamma_s) = D + D_s = \Delta_s; \qquad D_s \approx \frac{\log N_s}{\log \lambda} \tag{3.14}$$

where Δ_s is the overall effective dimension.

When $\gamma_s < \gamma_0$, the upper bound γ_s for observable singularities leads to a second order multifractal phase transition. The Legendre transform of $c(\gamma)$ with $\gamma > \gamma_s$ leads to a spurious linear estimate K_s instead of the nonlinear K for $q > q_S$; $q_s = c'(\gamma_s)$ being the maximum moment that can accurately be estimated. $K_s(q)$ will follow the relation:

$$\begin{aligned} K_s(q) &= \gamma_s(q - q_s) + K(q_s) \qquad q \geq q_s \\ K_s(q) &= K(q) \qquad\qquad\qquad\;\; q \leq q_s \end{aligned} \tag{3.15}$$

This is a second order phase transition associated with a jump in the second derivative of the (free energy/Massieu potential; $\Delta K''(q_s) = -K''(q_s)$).

When constructing a cascade process, the multiplicative iterations will generally be performed down to a scale η (the inner scale of the process), but it will generally be observed by spatial and/or temporal averaging on scales $\ell >> \eta$ (with corresponding adimensional quantities $\lambda = L/\ell$, $\Lambda = L/\eta$, L being the outer scale of the process). The variability at the observation scale ratio λ may be wilder than the corresponding field obtained by stopping the cascade at the same scale ratio. We say that the observation is dressed by the small scale activity, and that the process without smaller scale activity is bare. For small γs this won't affect their computed values. Above a certain critical singularity order γ_D the dressed codimension will be determined by maximizing the probability (minimize c) with the only constraint being the convexity, the dressed codimension (c_d) will thus follow the tangent and the dressed quantities follow:

$$\begin{aligned} c_d(\gamma_d) &= q_D(\gamma_d - \gamma_D) + c(\gamma_D) \quad && \gamma_d \geq \gamma_D \\ c_d(\gamma_d) &= c(\gamma) && \gamma_d \leq \gamma_D \end{aligned} \tag{3.16}$$

where $q_D = c'(\gamma_D)$ and is the slope of the algebraic fall-off of the dressed probability distribution, it is the critical order of divergence of statistical moments ($\langle \varepsilon^q \rangle = \infty$; $K_d(q) = \infty$, $q \geq q_D$). Schertzer and Lovejoy [106, 107, 109] have shown that q_D is the solution of:

$$D = q_D D - K(q_D) = q_D(D - \gamma_D) + c(\gamma_D) \tag{3.17}$$

When $\gamma_S < \gamma_D$, it is important to estimate the maximum observable dressed singularity for a given sample size with $\Delta_S = c_d(\gamma_{d,s})$ by taking the Legendre transform of c_d with the restriction $\gamma_d < \gamma_{d,s}$. The finite sample $K_{d,s}(q)$ is given by:

$$\begin{aligned} K_{d,s}(q) &= \gamma_{d,s}(q - q_D) + K(q_D) \quad && q > q_D \\ K_{d,s}(q) &= K(q) && q < q_D \end{aligned} \tag{3.18}$$

For $N_S \to \infty, \gamma_{d,s} \to \infty$ and for $q > q_D$, $K_{d,s}(q) \to K_d(q) = \infty$. For a large but finite N_S there will be a high q (low temperature) first order phase transition corresponding to a jump in the first derivative of K(q):

$$\Delta K'(q_D) = K_{d,s}(q_D) - K'(q_D) = \gamma_{d,s} - \gamma_D = \frac{\Delta_S - c(\gamma_D)}{q_D} \tag{3.19}$$

for small samples ($\Delta_S \approx c(\gamma_D)$), this transition will be missed, the free energy simply becoming "frozen".

Later on we will estimate (using the double trace moments method) that $\alpha \approx 0.85$, $C_1 \approx 0.4$ and $H \approx 0$ for the network station density. Since we have only one realization ($N_s = 1$, $D_s = 0$, $\Delta_s = D = 2$, $c(\gamma_s)=2$), we estimate with the universality relations (eqs. 2.11 and 2.12) that $\gamma_S = 0.9$. from $q_s = c'(\gamma_s)$ we obtain $q_S = 7.3$. However we already mentioned that $c(\gamma)$ manifest a linear behavior before reaching this limit. We interpret this result as a manifestation of a first order phase transition with: $q_D \approx 3.6 \pm 0.1$; $c(\gamma_D) \approx 1.1$; $\gamma_D \approx 0.7$. This is in agreement with the observed probability tail (fig. 3-6) reported for a scale in the scaling regime (we estimated $q_D \approx 3.7 \pm 0.1$).

III.2.2.4 Trace Moments:

This is a technique that deals directly with multifractal measures. It is a generalization of the partition function approach of Hentschel and Procaccia [43], Grassberger [41], and Halsey-et-al [42], although since we are dealing with stochastic processes, it also involves ensemble averaging. In this method, contrary to the double trace moment method (DTM), no functional form of K(q) is assumed. It is only in a second step that claims about universality could be made.

The simplest method we used to obtain the scaling exponents K(q) is to estimate the statistical moments of order q at different resolutions. Since our data set is distributed over a sphere, we first have to define the field at a resolution λ. We chose to use grids such that each box has the same area. This is easily accomplished. We partitioned the axis of the globe into slices of equal z (where z is the length of the projection of the slice onto the axis that goes from the center of the earth to the north pole) so that the area of the intersection of each slice with the earth's surface will be the same. We partitioned the globe in slices of equal longitudes. The intersection of those two partitions gives a covering with boxes of equal areas. We also tried displacing the poles of this partition to check for possible N-S/E-W dependence on the grid chosen due to the fact that the boxes do not all have the same shape (boxes near the poles are elongated in the north-south direction while boxes near the equator are elongated in the east-west direction). No significant differences were observed. The coarse graining process is performed in an isotropic manner. It doesn't matter that the boxes have a preferred orientation. We should also not confuse this with possible anisotropy of the field under study. For example, the raingage network shows some anisotropy that manifests when we perform quasi-1D analysis like the one that is presented in appendix B.

At a certain box size λ for a series of values of q we estimate:

$$\left\langle \rho_\lambda^q \right\rangle = \frac{1}{N_b(\lambda)} \sum_{i=1}^{i=N_b} \left(\frac{n_i}{\lambda^{-2}} \right)^q \tag{3.20}$$

where ρ_λ is the density of stations ($= n_i / \lambda^{-2}$ for the box i) and N_b is the number of boxes needed to disjointly cover the set. Then we repeat the procedure for different box sizes λ. This procedure was implemented in a very efficient manner, that avoids spending calculation time on empty boxes, using the Hunt and Sullivan [49] algorithm (explained in appendix A). Figure 3-7 shows the results of this analysis for a few values of q. We can see that the scaling is observed in the range $0 \leq \log \lambda \leq 2.0$ (200 to 20 000 km: roughly the same as before). In previous section we mentioned that for a multifractal field $\left\langle \rho_\lambda^q \right\rangle \sim \lambda^{K(q)}$ so by taking the slope of the curves of fig 3-7 in the scaling region we can deduce the K(q) function that is shown on fig. 3-8.

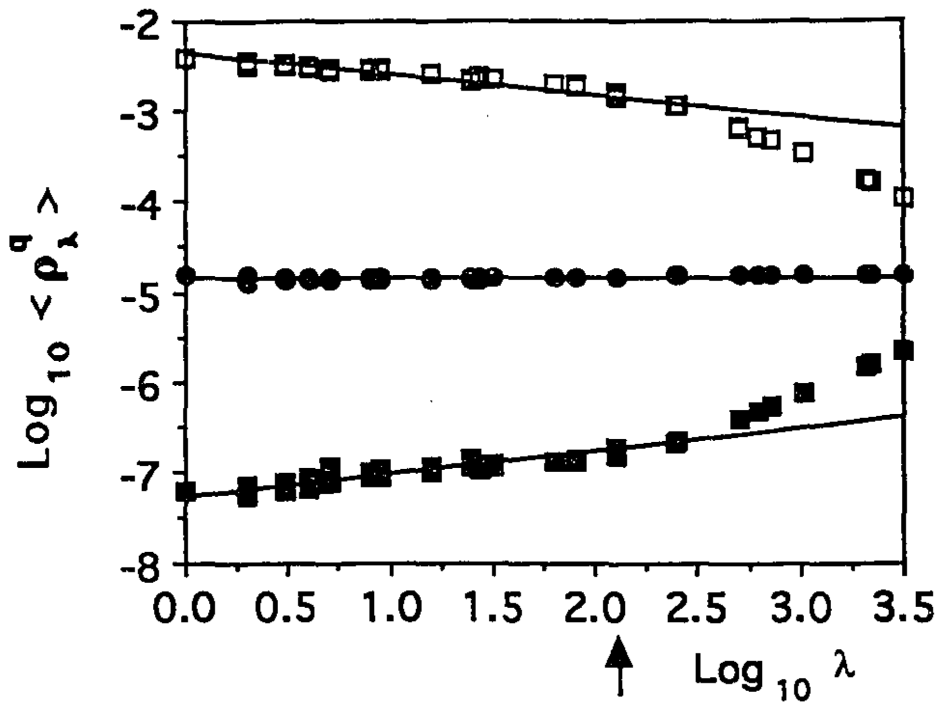

Figure 3-7: Log of the statistical moments against Log of the scale ratio λ for the network for moments of order $q = 0.5$ (empty squares), $q = 1.0$ (filled circles) and $q = 1.5$ (filled squares). The arrows indicate the limits of the scaling region. $\lambda = 1$ corresponds approximately to 20 000 km.

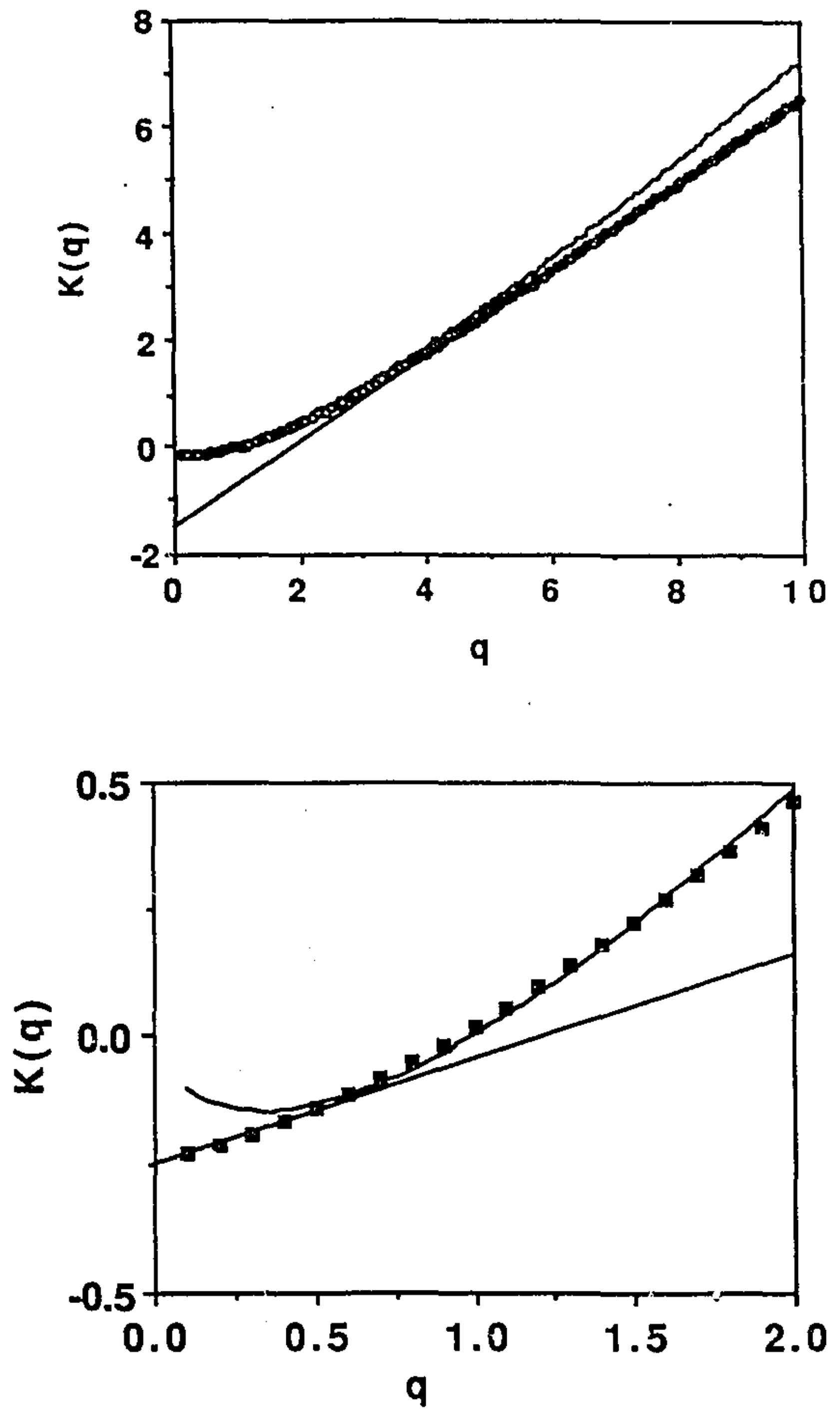

Figure 3-8: The scaling exponent K(q) vs. q with the fitting curve having scaling parameters $\alpha = 0.85$ and $C_1 = 0.37$. On the top figure the asymptotic linear region (after a multifractal phase transition) is fitted to a straight line of slope $\gamma_{d,s} = 0.8 \pm 0.1$. On the bottom figure, the linear region for small q is fitted to a straight of slope $\gamma_{min} = 0.2 \pm 0.1$

We fitted the K(q) function to the form given by eq. 2.12 by the Levenberg-Marquant Method (Press et al. [98]) using the portion of the curve expected to follow this relation. We obtained $\alpha = 1.0$ and $C_1 = 0.23$. The theoretical curve for these parameters is also reported in fig. 3-8. On this figure we observe for large q a linear behavior, the multifractal phase transition explained before, for $q > q_D \approx 3.6$, and as expressed by relation 3.18 whose slope is estimated as $\gamma_{d,s} = 0.8 \pm 0.1$. This is comparable to what can be directly observed in fig. (i.e. $\gamma_{d,s} \approx 0.9$). For small values of q the fitted K(q) doesn't follow the experimental data points either. This can be explained by the fact that this portion of the curve is determined by small values of the field, since the number of stations is an integer number we miss very small values of the multifractal field. This implies an effective detectability limit that can be expressed by a minimum correctly estimated moment q_{min} and correspondingly a γ_{min}. We estimate γ_{min} by the slope of the linear portion in the small q region and we obtain $\gamma_{min} = 0.2 \pm 0.1$ from which we deduce $q_{min} = 0.6 \pm 0.1$. This effect will be further discussed in a following section were we build up a simulated network.

III.2.2.5 Double Trace Moment Analysis of the network

We wish to apply the same technique that we used on reflectivity fields (previous chapter) to estimate the universal multifractal parameters describing the scaling of the raingage network. The first step in applying the DTM technique is to check the scaling range of various moments. Figure 3-9 shows $\log \mathrm{Tr}\left(\left(\varphi_\lambda^\eta\right)^q\right)$ vs. $\log \lambda$ for $q = 2$. We used a 256 x 256 regular grid (sinusoidal projection) to analyze the density of stations. As we can see, scaling is observed for log Trace moment vs $\log \lambda$ (for different values of q, $\eta = 1$) in the range $0 \le \log \lambda \le 2.2$ which, as expected, is roughly the same as what we deduced from fig. 3-7. From these curves we obtain by linear regression over the scaling region the double trace moment that we show on fig. 3-10. On this graph we have plotted $\log |K(q, \eta)|$ vs. $\log \eta$. From a regression on the straight portion of this curve we deduce that for the network $\alpha = 0.85\pm0.2$ and $C_1 = 0.35\pm0.1$. On the same figure we have plotted the result of the analysis for a simulated field using the estimated parameters and a simulated network consisting of 7077 stations generated from this simulated field (details of the simulation are given in the next section). These three curves will serve to illustrate two important points about the double trace moments technique. First we note that for high values of η all the curves become flat. This is because eq. 2.20 breaks down whenever $\max(q\eta, q) > \min(q_s, q_D)$. We observed a break in $K(q)$ for $q_D = 3.6 \pm 0.1$. This break was interpreted as a first order phase transition. It is reflected in $K(q,\eta)$. For the value of q that we used ($q = 2.0$) we expect the break to occur for $\eta \approx 3.6$ ($\log \eta \approx 0.55$) which is observed. The second point that fig. 3-10 illustrates is the behavior of the moments for low values of η. The curves for the real and the simulated network depart from linearity. In this region of the curve the analysis depends on low values of the field and since we only have a finite number of stations the low values of the density field will be badly estimated leading to a departure from linearity in the $\log |K(q, \eta)|$ vs. $\log \eta$ curves. This effect will show whenever $\max(q\eta,q) < q_{min}$. In the previous section we estimated that $q_{min} = 0.6 \pm 0.1$ and indeed this corresponds to the break observed in the $K(q,\eta)$ curve.

Now that we have an estimate of the α and C_1 parameters ($\alpha = 0.85\pm0.2$ and $C_1 = 0.35\pm0.1$) and that we know the spectral slope β we are able to determine the third parameter H. By the use of equation 2.21 we obtained $H = 0.05 \pm 0.1$.

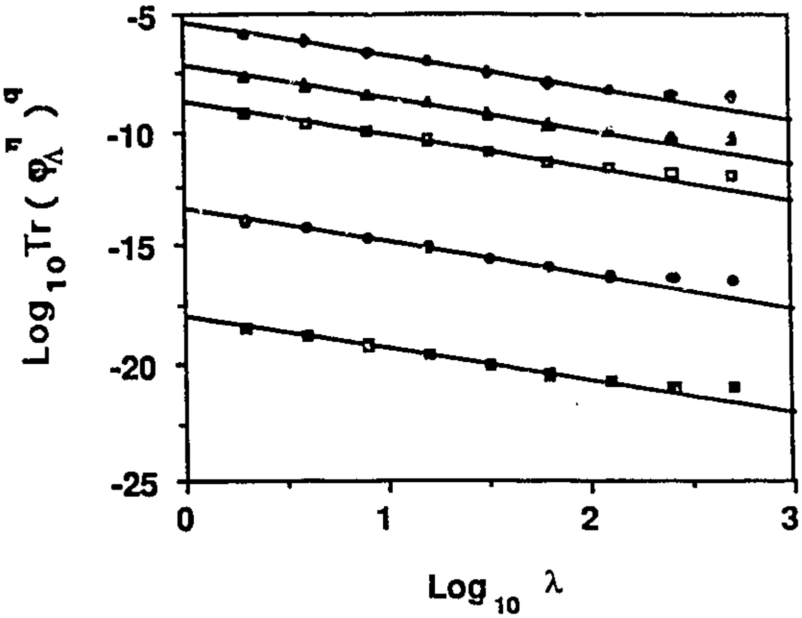

Figure 3-9: $\log\left(\mathrm{Tr}_{\lambda}\left(\varphi_{\lambda}^{\eta}\right)^{q}\right)$ versus $\log(\lambda)$ for several values of η (from top to bottom, $\eta = 1.2, 0.7, 0.3, 0.1$) for the network , We used $q = 2$, and the scale ratio $\lambda = 1$ for a distance of 20 000 km.

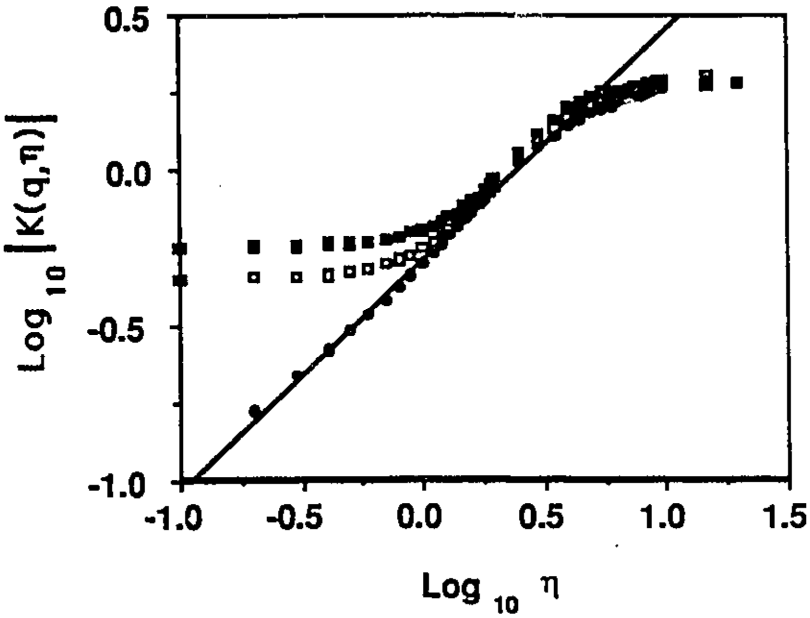

Figure 3-10: $\log |K(q, \eta)|$ vs. $\log \eta$ for the network (filled squares), a field (without any minimum thresholding) having the same parameters as the network (filled circles) and a simulated network obtained from the simulated field (empty squares).

III.2.2.6 Simulation of the network

In the previous sections we presented some results for a simulated network. These simulations were mainly used to test the different methods and to verify our understanding of the different techniques. In this section we will present some more details on the method used to produce those simulations and some further results. We show a simulated network in fig. 3-11

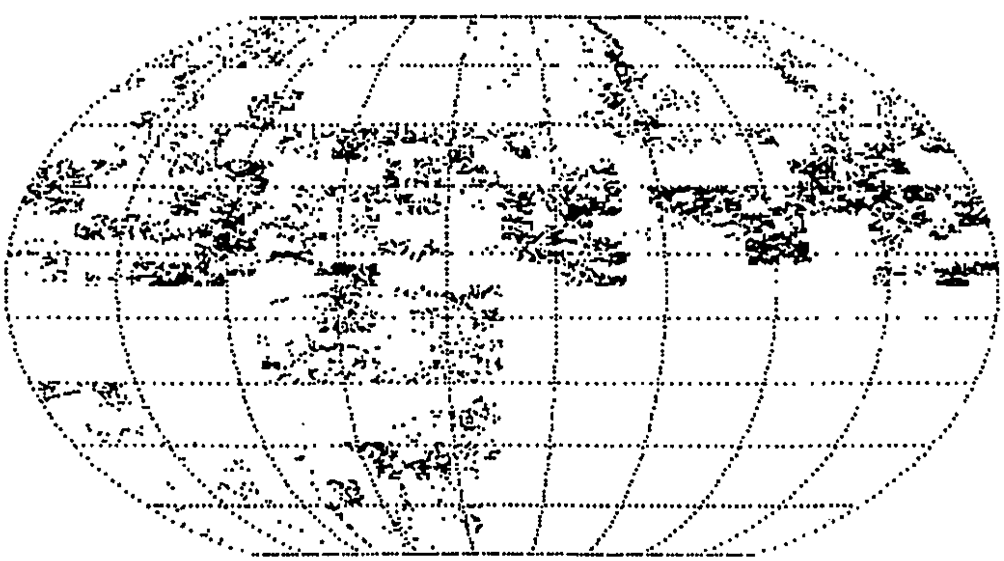

Figure 3-11: Position of the 7077 stations for the simulated network used for testing the different methods.

The simulations were performed using a discrete cascade (Schertzer and Lovejoy [109]) on a 256x256 grid (this is roughly the observed range of scaling found empirically for the network, see fig 3-9). The field produced by the simulation with the parameters deduced by the DTM method was taken as the density field. We multiplied this field by the expected total number of stations in order to obtain a simulated network with a total number of stations near the total number of stations in the real network that we analyzed. With the same total number of stations we should be able to reproduce roughly the same

γ_{min} as the real network since $\gamma_{min} \approx \log \rho_{min} / \log \lambda$. We rounded the number of stations in each box to the nearest integer value. Within each box we distributed the stations according to a uniform random distribution and then extracted a database with the same resolution as the real network. Note that both the total scaling range as well as the total number of stations are important parameters in the simulation.

We estimated the usual statistical moments using the regular grid (fig 3-12). As we can see the simulation is in very good agreement with the scaling properties of the real network. We were even able to reproduce the scaling break due to the finite number of stations (introducing the homogeneity scale). Figure 3-13 shows the c(γ) curve obtained by the PDMS method. Here again the empirical and simulated curves are in good agreement. From the statistical moments on a regular grid of fig. 3-12 we produced the K(q) curve for both networks (fig. 3-14). We can see that except for small differences for large q, both curves fall on top of one another. It is also the case for the DTM technique shown in the previous section (fig. 3-10). The departure from the theoretical curve is due to the finite number of stations which result in a minimum value of q and γ for the analysis is valid (as discussed in section III.2.2.4).

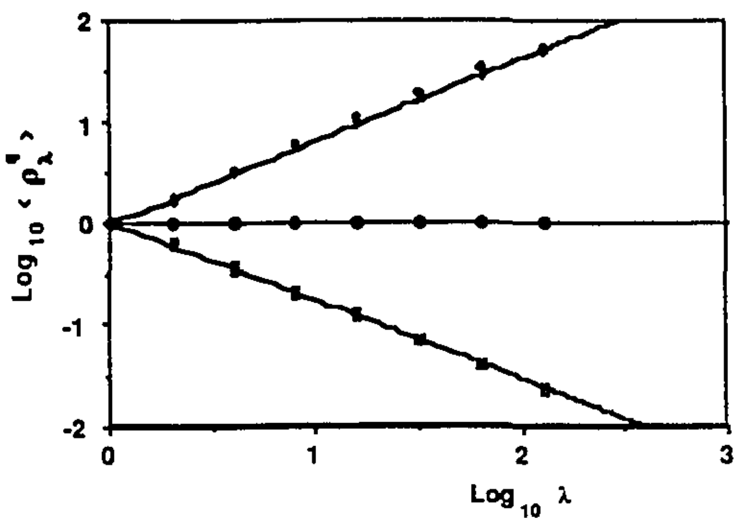

Figure 3-12: Log of the statistical moments against Log λ for the network. q = 0.5 (empty diamonds for real network, plus sign for the simulated network), q = 1.0 (empty circles for the real network and x for the simulated network) and q = 1.5 (empty squares for the real network and ⁎ for the simulated network).

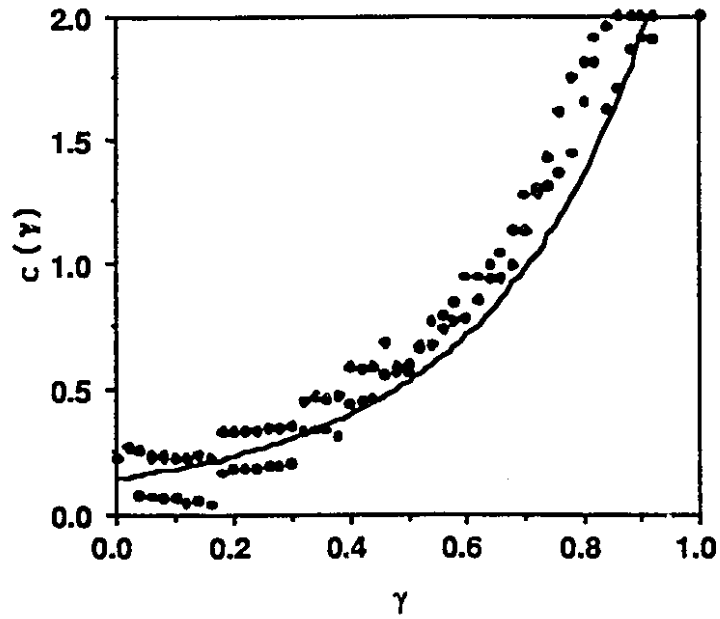

Figure 3-13: c(γ) vs. γ for the real network (filled circles) and for the simulated network (empty diamonds). The solid line is the theoretical curve for the K(q) function using the parameters determined by the double trace method. i.e. $\alpha = 0.85$ and $C_1 = 0.35$.

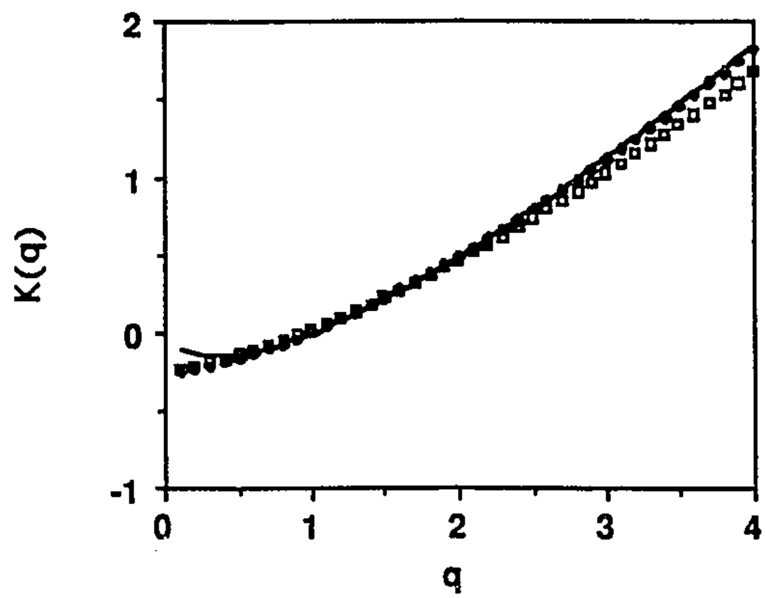

Figure 3-14 : K(q) vs. q for a simulated network of 7077 stations having parameters $\alpha = 0.8$ and $C_1 = 0.4$ (diamonds) and the same function for the real network (empty squares). We also show the theoretical curve for $\alpha = 0.85$ and $C_1 = 0.35$.

III.3 Obtaining Information About the Measured Field: The Example of Rain

III.3.1 Corrected Double Trace Moment Analysis of the rainfield

Now that we have a well characterized network it is possible to get some information about the statistical properties of the spatial distribution of the field of interest: here the rain field. To extract the information for the rain from the network, we assume (as a first approximation) that the rain and the network are totally uncorrelated phenomenon, e.g. we ignore the problem of correlations between rain events and the physical location of the stations (such as the so-called "island effect" which may give subtle biases to rain estimates over the ocean, etc..). In future, the problem of correlations between the network and climatological rainfall which theoretically can be dealt with by considering joint probability distribution between rainfall and the network and using vector singularities as outlined in Schertzer and Lovejoy [115, 118].

A station measures the rainfield only over a finite area around its location. Consider the sum over the i[th] grid box (or circle) scale λ $(B_{\lambda i})$ of the raw rainfall[5] $\left(M_\Lambda^\eta\right)$ accumulations raised to a power η : $\sum_{B_{\lambda}} M_\Lambda^\eta$. The subscript Λ is used in the same sense as eq. 2.17 for the DTM, it is the spatial scale associated with the (daily) accumulation period (averaging in time will smooth in space at a scale determined by the corresponding space/time transformation). Perhaps the simplest derivation is as follows (see Tessier et al [129] for a slightly different presentation). Consider that at the finest resolution Λ the station density is an indicator function ρ_Λ of the measurements of R_Λ; at scale λ, the measured rain is the product: $M_\lambda = \rho_\lambda R_\lambda$. The trace moments are given by:

$$\mathrm{Tr}_\lambda\left(M_\Lambda^\eta\right) = \mathrm{Tr}_\lambda\left(\rho_\Lambda^\eta R_\Lambda^\eta\right) = \lambda^{K_M(q,\eta)-(q-1)D} = \lambda^{K_r(q,\eta)+K_R(q,\eta)-(q-1)D} \qquad (3.21)$$

It is now straightforward to see that

$$K_M(q,\eta) = K_R(q,\eta) + K_\rho(q,\eta) \qquad (3.22)$$

[5] We consider that the original measurements M_i have an intrinsic (generally unknown) resolution Λ To circumvent this problem we raised the raw data to the power η.

since ρ_Λ is an indicator function, we can make the following approximation:

$$K_\rho(q,\eta) = K_p(q,1) \tag{3.23}$$

Note that this approximation only holds at the scale Λ where ρ_Λ is necessarily a 1 or 0; $\rho_\Lambda^\eta = \rho_\Lambda$

The measured multiple scaling function $K_M(q,\eta)$ can readily be used to determine $K_R(q,\eta)$ by exploiting the fact that $K_R(q,0) = 0$, hence:

$$K_M(q,0) = K_p(q,1) \tag{3.24}$$

$$K_R(q,\eta) = K_M(q,\eta) - K_M(q,0) \tag{3.25}$$

The $\log\left(Tr_\lambda\left(\varphi_\Lambda^\eta\right)^q\right)$ versus $\log(\lambda)$ before corrections are shown on fig 3-15. We can see that scaling is observed over a large region. From such an analysis we obtain the (network corrected) values $\alpha = 1.35 \pm 0.1$ and $C_1 = 0.15 \pm 0.05$ as may be seen on fig. 3-16 where we have plotted $\log|K(q,\eta)|$ vs. $\log\eta$ for $q =$ 0.5, 1.5 and 2.0. The $\log\eta$ horizontal asymptote at $K \approx 1$ is close to the accuracy of the estimates of K.

The third parameter H also needs corrections that can be obtained from the following:

$$\lambda^{H_M} M'_\lambda = \lambda^{H_p} \rho'_\lambda \lambda^{H_R} R'_\lambda = \lambda^{H_p + H_R} \rho'_\lambda R'_\lambda \tag{3.26}$$

where the primes designate the corresponding conserved quantities. Here the degree of non-conservation H for the "true" process is simply given by the difference $H_M - H_p = \frac{1}{2}\left(\beta_M - \beta_p\right)$ which can be deduced with the formula 2.21. In the determination of β_M (see fig. 3-17) we fitted only the region over which good scaling was observed with other methods (i.e. 400 to 8000 km). The estimated spectral slope is $\beta_M = 0.2 \pm 0.2$. Since we have already estimated (from fig. 3-3) that $H_p \approx 0 \pm 0.1$ and $K_M(2) \approx 1 \pm 0.1$ we therefore obtain $H_R \approx 0.2 \pm 0.3$.

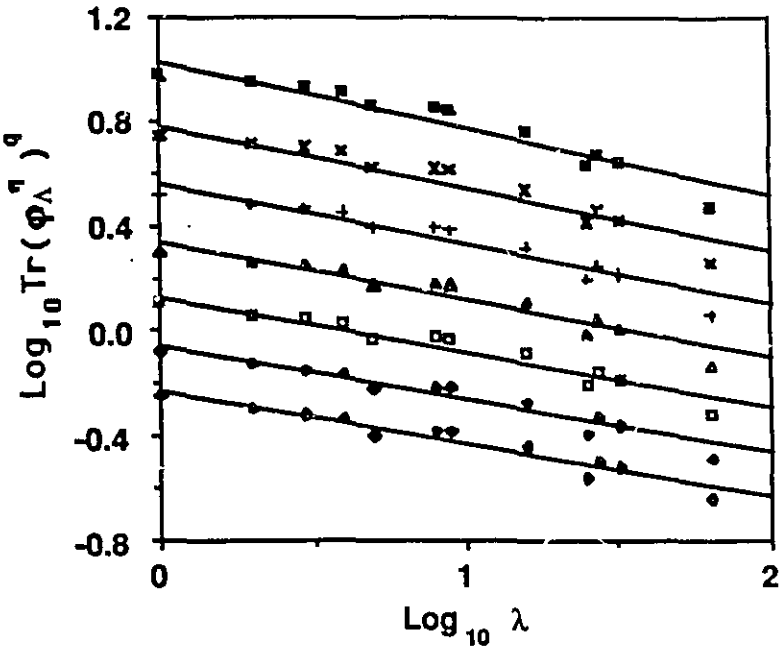

Figure 3-15: $\log\left(\mathrm{Tr}_\lambda\left(\varphi_\Lambda^\eta\right)^q\right)$ versus $\log(\lambda)$ for several values of η (from top to bottom, η = 1.2, 0.7, 0.3, 0.1) for daily rainfall accumulations on a global network .

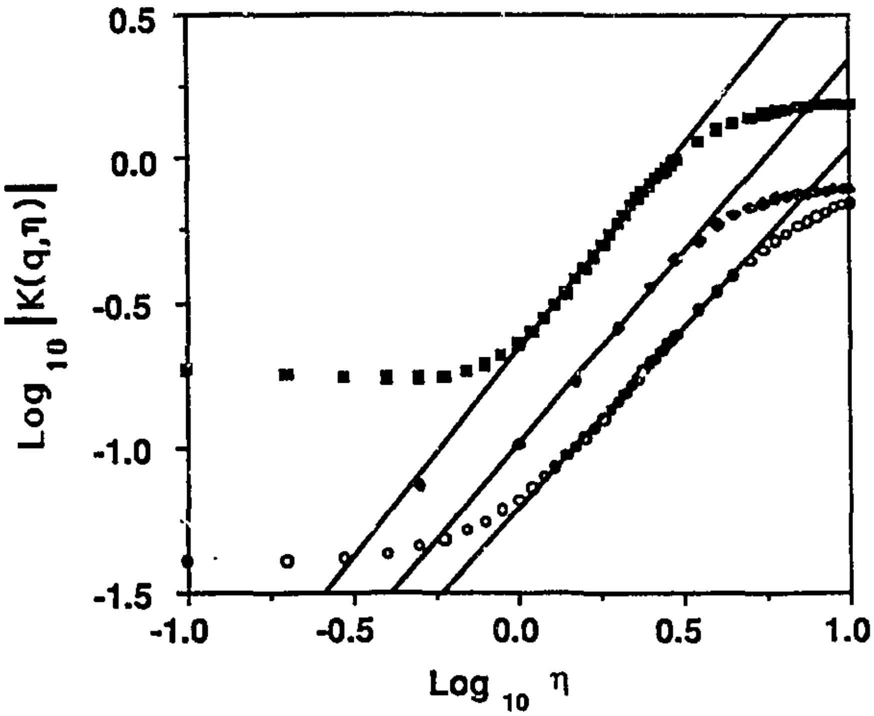

Figure 3-16: $\log(|K(q,\eta)|)$ versus $\log(\eta)$ for daily rainfall accumulations on a global network after the needed corrections explained in the text. From top to bottom curves for $q = 2.0$, 1.5 and 0.5 are shown. The regression lines on the different curves give a value of $\alpha = 1.35 \pm 0.1$ and $C_1 = 0.15 \pm 0.05$.

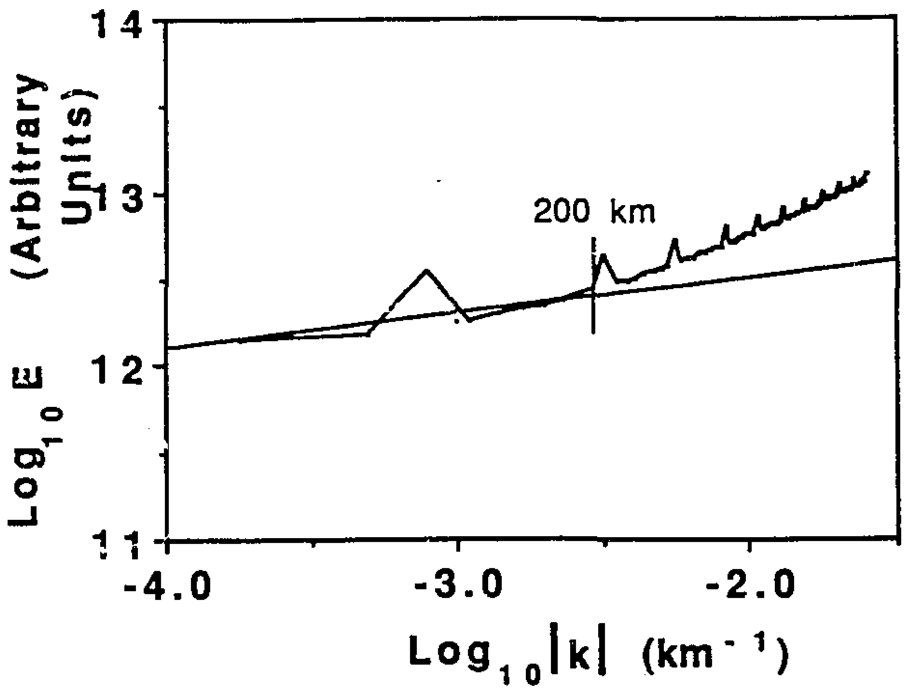

Figure 3-17: Power spectrum for daily rainfall accumulations as measured by a global network. The regression line for the region from 400 km to 8 000 km gives a spectral slope ≈ 0.2±0.15.

III.3.2 Trace Moment Analysis of the Rain

As we have seen with the analysis of the network, more information could be gained with the (single) trace moments. In particular a better estimate of the range of validity of universal relations (eqs. 2.12).The correction scheme we have developed for the double trace moment could also be applied to regular trace moments. Taking $\eta = 1$, in equation (3.25):

$$K_R(q) = K_M(q) - K_\rho(q) \tag{3.27}$$

The $\log\langle M_\lambda^q \rangle$ versus $\log\lambda$ curves are shown in fig. 3-18. The scaling range is slightly smaller than for the network. We observe scaling over the range: $0 \le \log \lambda \le 1.8$. From this we deduce the $K_M(q)$ function which is shown in fig. 3-19. Also shown in this figure are $K_\rho(q)$ and $K_R(q)$.

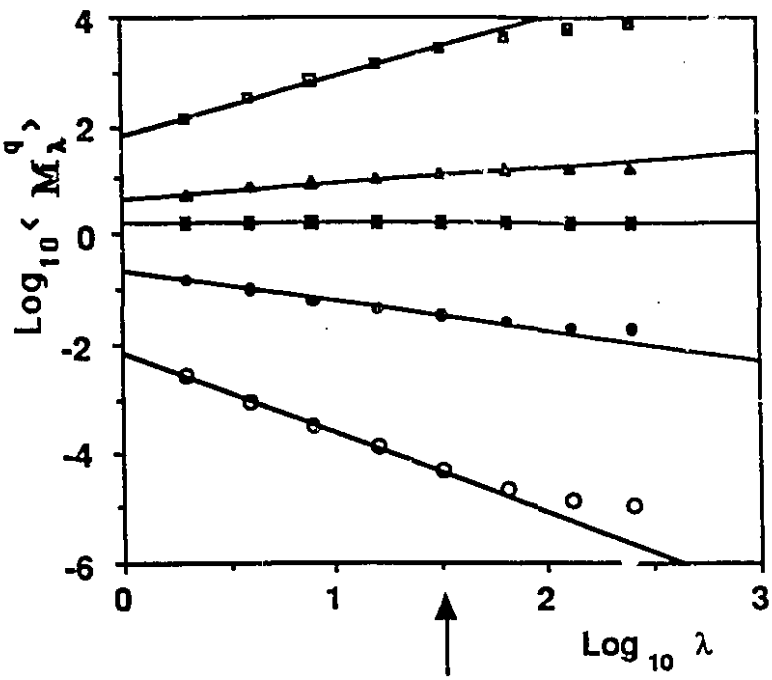

Figure 3-18: Log of the statistical moments against Log of the scale ratio λ for the network for moments of order q = 0.3, 0.8, 1, 1.4, 2.1 (from top to bottom). The arrow indicates the approximate lower limit of the scaling range of the rainfield.

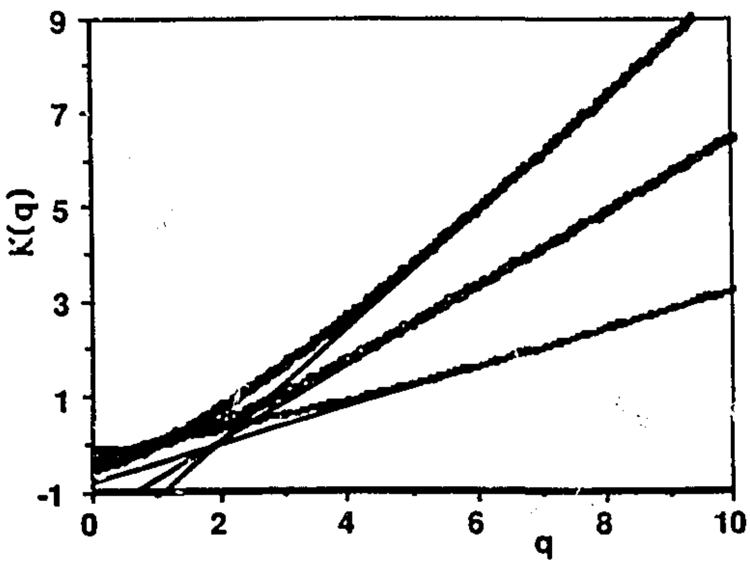

Figure 3-19: K(q) vs. q for the measured rainfall (filled diamonds), the network (empty circles) and the corrected rainfall (filled squares). In the high q region straight lines have been fitted in order to obtain $\gamma_{R\ d,s}$, $\gamma_{M\ d,s}$, $\gamma_{\rho\ d,s}$.

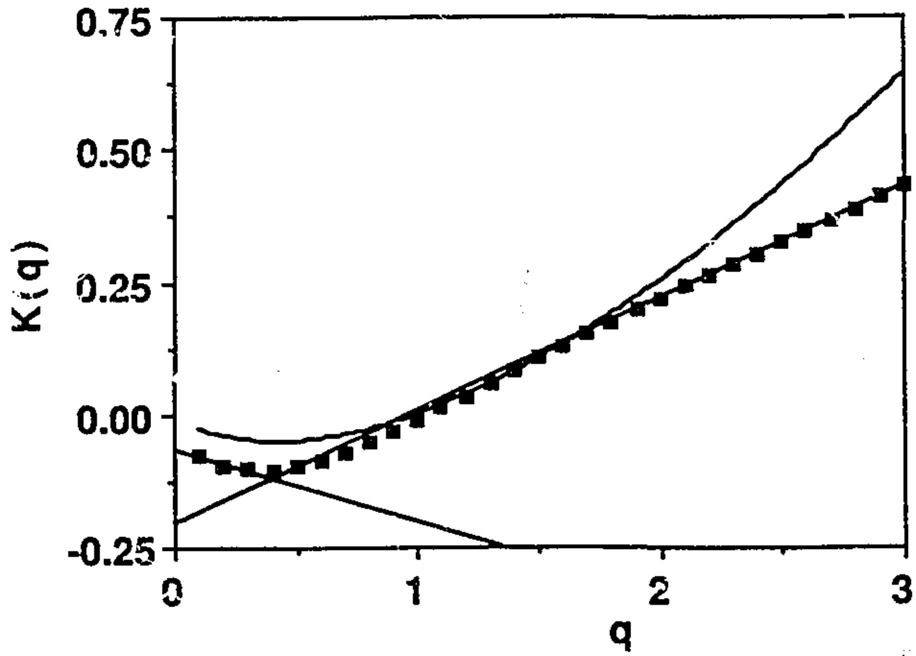

Figure 3-20: K(q) vs. q for the corrected rainfall determined using the regular grid showing the asymptotic linear regions of the curve whose slopes give $\gamma_{min} = -0.13$ (small q) and $\gamma_{d,s} = 0.21$ (large q). The continuous line was calculated using the parameters α and C_1 obtained by the DTM method.

In order to interpret the empirical K(q), we estimate the maximum value of q attainable (due to sampling effect) with the dataset. The number of realizations investigated is 365 (one each day for a year) but since we observed a scaling break at time scales of roughly 16 days (see chapter IV), if we interpret this as an outer scale for the scaling regime we obtain:

$$N_s = \frac{365}{16} \approx 23$$

where N_s is the number of independent realizations since we observed scaling of the network for $0 > \log \lambda > 1.8$:

$$D_s = \frac{\log 23}{1.8} = 0.76$$

the dimension of the embedding space is 2, $\Delta_S = D + D_S = 2.76$

With the fitted parameters for the rainfield (i.e., α = 1.35, C_1 = 0.16 we therefore estimate that $\gamma_s = 0.95$ and $q_s = c'(\gamma_s) = 7.0$. However the rainfield manifests a divergence of moments for $q_D < 7$. The point where the curve calculated from the estimates of α and C_1 obtained with the DTM method and the experimental points depart indicates a value of $q_D \approx 2$ corresponding to $\gamma_D = 0.3$. Many estimates of q_D (mainly from histograms) can be found in the literature (see table 3-2). Our estimate is comparable to the ones cited. At the present time, it is still not clear if the spread in the different estimates is due to the accuracy of the different evaluations or if reflect more profound differences between the dataset used. From the asymptotic slope of K(q) (large q region) we can estimate a $\gamma_{d,s}$ for each of the three curves of fig. 3-19. We obtain $\gamma_{M\ d,s} \approx 1.1$, $\gamma_{\rho\ d,s} \approx 0.8$ and $\gamma_{R\ d,s} \approx 0.3$. With eqs. 3.18 and 3.27 we can see that: $\gamma_{R\ d,s} = \gamma_{M\ d,s} - \gamma_{\rho\ d,s}$ is approximately verified. In the small q region (fig. 3-20) we calculate the minimum observable singularity, $\gamma_{min} \approx -0.13 \pm 0.1$. As before, using $q = c'(\gamma)$ we deduce $q_{min} \approx 0.2$. Table 3-1 summarizes all the quantities we have estimated for the raingage network density field and the rainfield.

	α	C_1	H	q_S	γ_S	q_D	γ_D	$q_{d,S}$	$\gamma_{d,S}$	q_{min}	γ_{min}
Network	0.85	0.37	0.05	7.3	0.91	3.6	0.74	3.1	0.7	0.6	0.2
Rain	1.35	0.15	0.2	7.0	0.95	2.0	0.30	2.0	0.4	0.2	~0.1

Table 3-1: Summary of the universal multifractal parameters estimated for the raingage station density and the rainfield as well as phase transitions critical points for these fields.

Data Types	Locations	q_D	References
Radar rain differences (space)	Tropical Atlantic	2	Lovejoy, 1981 [62]
Radar rain differences (time)	Tropical Atlantic	1.7	Lovejoy, 1981 [62], Lovejoy and Mandelbrot, 1985 [66]
Radar reflectivity	Montréal	1.1	Schertzer and Lovejoy, 1987 [109]
Vertical pointing radar reflectivity	Montréal	3.0 (rain) 2.4 (snow) 3.9 (bright band)	Duncan et al., 1992 [28]
Daily raingages accumulations	Nîmes-Courbessac	2.6	Ladoy et al., 1991 [55]
Tipping bucket gages	Montréal	2	Zawadzki, 1987 [142]
Tipping bucket gages	Western Canada	2.5±0.5	Segal, 1979 [124]
Rain drop volumes	Hawaii	1.9±0.5	Blanchard, 1953 [8]
Daily raingages accumulations	World	2.0	This thesis

Table 3-2: A comparison of various empirical estimates of the divergence of moments exponents q_D. Adapted from Lovejoy and Schertzer [74].

III.4 Conclusion

The inhomogeneity in the spatial distribution of stations of geophysical networks has always been a problem. Different techniques have been used to attempt to solve this problem but the recognition of the scale invariant properties of at least some of these networks is very recent. The first scaling attempts treated the problem by considering the location of stations as a set of points with fractal properties. We proposed a different approach. What matters is the density of stations field underlying this set. This field can be multifractal. For the global raingage network we have shown that it is the case. We established that scaling is observed over the range of scales of 200 km to 8 000 km. Using different techniques: (single and double) trace moments, PDMS and spectral analysis, we were able to estimate that the universal multifractal parameters for this network density field, which are $\alpha = 0.85\pm0.2$, $C_1=0.4\pm0.2$ and $H = 0\pm0.2$. This universal multifractal behavior could be observed for K(q) between q_{min} = 0.5±0.6 and q_D = 3.6±0.5. Below q_{min} there are not enough stations to get a good estimate of the scaling function and above q_D divergence of moments causes a first order phase transition in the scaling functions. These transition points have analogues in the singularity space. By Legendre transformation we could derive the minimum observable order of singularity γ_{min} = 0.2±0.1 and the maximum observable order of singularity is $\gamma_{d,s}$ = 0.7±0.1.

In the previous chapter we presented evidence for multifractal behavior of different remotely sensed fields related to atmospheric water. Based on some early analysis (Hubert and Carbonnel [45, 46, 47], Lovejoy and Schertzer [71, 73], Schertzer and Lovejoy [109]) pointing in the direction that surface rainfall should also be a spatio-temporal multifractal field. Removing the network bias with the help of a new framework ("multifractal objective analysis") amounts to replacing the usual small scale homogeneity and regularity assumptions (implicit in standard "objective" techniques such as Kriging) by more realistic scaling (inhomogeneity) assumptions. We introduced the idea that the measured field is the product of two multifractal fields: the density of stations and the analyzed field (in our case the daily rainfall accumulations). The corrections could then be expressed as simple subtraction of scaling exponents and spectral slopes. We tested this technique, and found that it seems to hold fairly well over the range of scales of 400 km to 8000 km. We estimated the universal multifractal parameters and obtained α = 1.35±0.2, C_1=0.15±0.1 and H = 0±0.3. These values of α and C_1 are compatible with estimates of these parameters for the spatial variability of radar reflectivities. It could be justified by the fact that a transformation such as the semi-empirical Marshall-Palmer relation which is widely used for converting reflectivities into rainrate ($Z=aR^b$) conserves the value of α. The limits to this universal multifractal behavior are q_{min} = 0.2±0.5 and q_D = 2.0±0.3. The corresponding point in the singularity space gives a minimum observable order of singularity γ_{min} = -0.1±0.1. and the maximum observable order of singularity $\gamma_{d,s}$ = 0.3±0.1.

We developed a new method to treat the problem of multifractal fields sensed by inhomogeneous (multifractal) networks. We applied it to global rainfall but we think that the method will be most helpful for the analysis of many other geophysical fields that presents the same difficulties such as the temperature, pressure, pollution records, earthquakes and many others. The interpolation problem which has been up to now the work-horse of the objective analysis practitioner will certainly have to be revisited since all the usual methods do not consider the basic scaling properties of both the measuring network and the analyzed (but this is at least another thesis!).

Chapter IV

The Temporal Scaling of Water Fields

IV.1 Spatial and temporal scaling:

We have discussed the spatial variability of various fields related to the distribution of water in the atmosphere, we now turn our attention to the problem of temporal variability. There are many reasons for studying this variability. In many applications knowledge of how the rainfall intensity at a point varies with time is an important issue all by itself. More fundamentally, the relation between the spatial and the temporal variability of turbulent fields is an outstanding theoretical problem. An understanding of the space/time relation is necessary in estimating water budgets as well as in making predictions (as is already recognized by various data assimilation schemes). Probably the most cited and widely used method of relating time and space is "Taylor's hypothesis of frozen turbulence" (Taylor [128]) which basically states that temporal (t) and spatial averages (l) are related by a constant velocity (v) in a relation of the form l = vt. Although this hypothesis has been widely used since the 30's in both atmospheric and laboratory turbulence, Zawadski [141] was the first to give it a (limited) test in rain using radar data. Although turbulence in the atmosphere is not "frozen", a statistical version of the hypothesis might still apply: i.e. the statistical properties in space and time are the same (if appropriately rescaled using a velocity parameter). If this statistical version held then rain would be isotropic in space-time. Recently Lovejoy and Schertzer [73] have analyzed lidar data of rain indicating that an anisotropic generalization of Taylor's hypothesis (discussed below) based on a turbulent (i.e., scale dependent) velocity is more appropriate than assuming frozen turbulence and space-time isotropy. Below we do not presuppose any specific relation between time and space: we seek to determine the universal parameters characteristic of the process in time and in space separately. This will provide us with some of the information needed to determine the space-time transformation operator, an issue that is still under active development.

IV.2 Functional Box Counting on time series

The first analysis we performed in the time domain was using Functional Box Counting analysis (Lovejoy et al. [70]). It consists in performing ordinary box-counting on sets obtained by thresholding the time series. In this analysis the distance used was the difference in time between events, we did this for every station, and accumulated the number of events for all stations (this corresponds to intersection of the measurements with the time axis). As we can see on figures 4-1 and 4-2 when the threshold value is 0 we get a dimension of nearly 1 which is to be expected since it only means that reports were distributed uniformly (missing reports were uniformly distributed in time; there was no significant clustering). The dimension decreases as expected, as we increase the threshold, this is because the exceedance set for large thresholds are sub-sets of those of small thresholds. As we increase the threshold an interesting phenomenon appears: we get a break in the scaling at times between 10 and 20 days, It is interesting since this time duration corresponds to the so called "synoptic maximum" (Kolesnikov and Monin [52]) which is generally interpreted as being the time that takes a perturbation to spread all over the world. This makes sense in the context of Taylor's hypothesis of frozen turbulence where each space scale has a corresponding time scale. We can see two different scaling regimes; the first for times smaller than the synoptic maximum and the second for times longer than this. Hubert and Carbonnel [45] also observed a scaling break at time scales comparable to what we obtained; they got a break around 8 to 16 days for their daily rainfall accumulations for a time series of 2^{14} days compiled for Dedougou (Burkina Faso), and they observed a break between 5 and 11 days for their hourly time series compiled for a nearby location. Larnder and Fraedrich [57] observed a break for the same period in a spectra for daily rainfall accumulation on a 45 year period for a station in Germany. Lovejoy and Schertzer [69] and Ladoy et al. [55] obtained a similar result for surface temperature spectra in France.

Although it would be possible to estimate the K(q) scaling function and then the universal multifractal parameters with this technique experience proved that it is not efficient to do so. These results are presented because they constitute one of the best demonstration of the two scaling regimes present in temporal series of rain. The universal multifractal exponents will be estimated with the Double Trace Moment, as before.

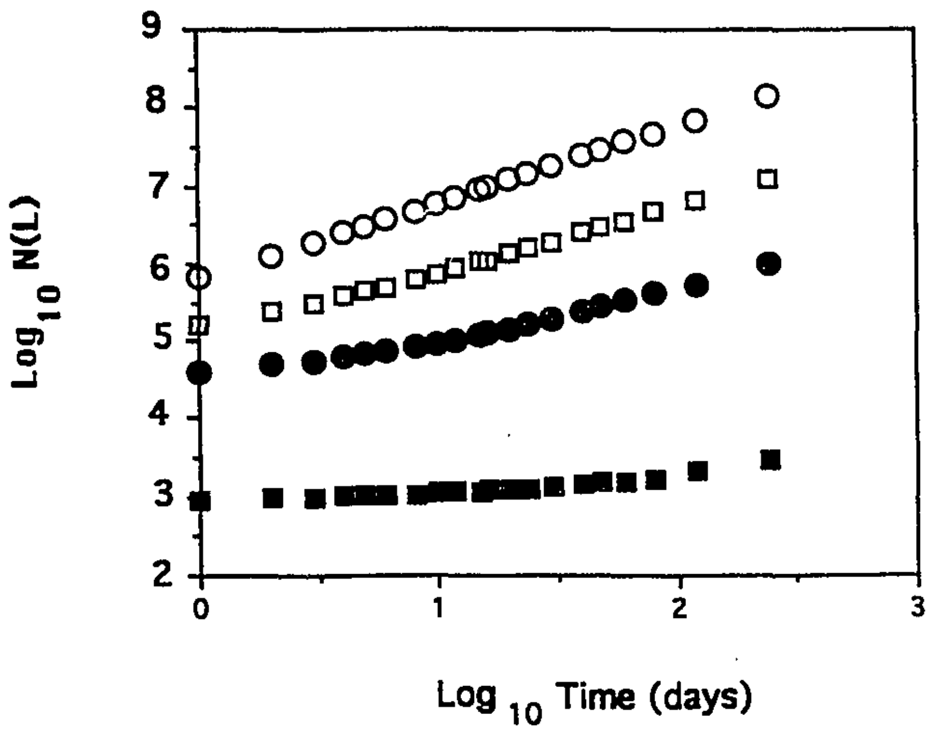

Figure 4-1a: Log of the number of events above a certain threshold against the log of the time interval (in days) for different threshold: 0 mm (empty circles), 0.1 mm (empty squares), 12.8 mm (filled circles) and 10.24 cm (filled squares).

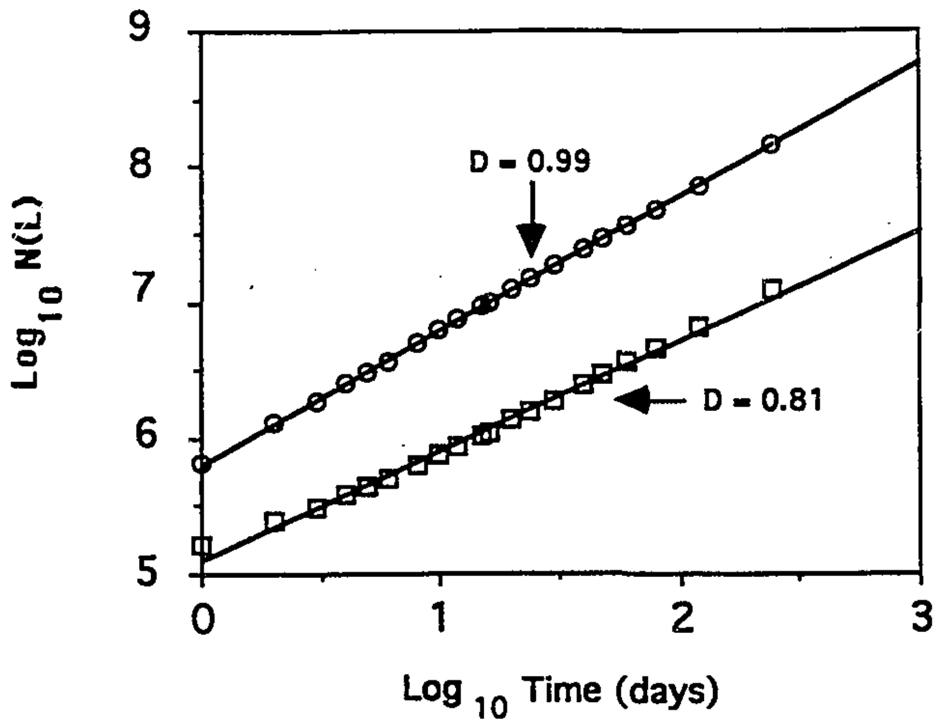

Figure 4-2a:

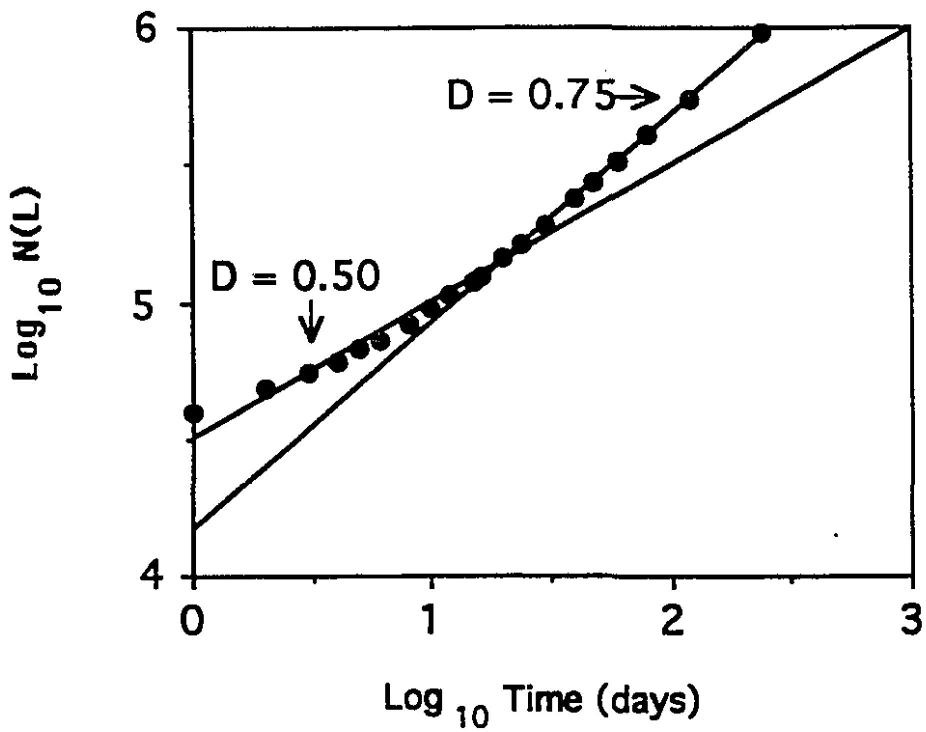

Figure 4-2b:

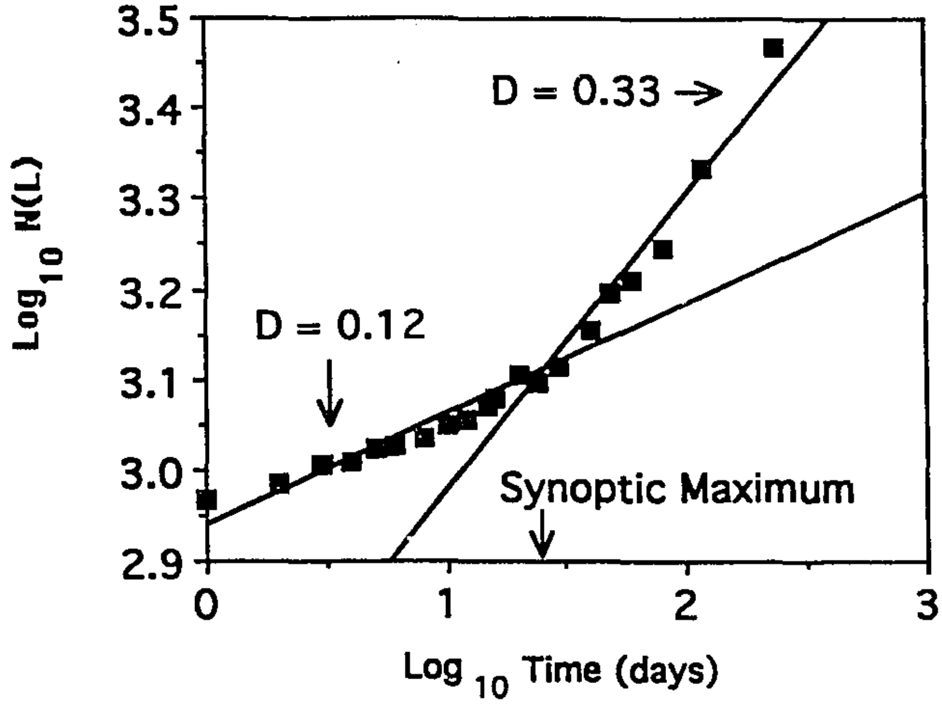

Figure 4-2c: Same as the previous graph but divided into different figures according to the different threshold: a) 0 mm (empty circles), 0.1 mm (empty squares) b) 12.8 mm c) 10.24 cm. There is a scaling break at time of the order of 10 to 20 days corresponds to the synoptic maximum.

IV.3 Power Spectrum Of Daily Accumulation Records

Another confirmation of the 1 to ~20 day scaling regime comes from inspection of the power spectrum (square of the modulus of Fourier amplitudes) which is shown on fig. 4-3. We had to compromise between the length of the series available without missing data and the number of reports. The best compromise we could obtain is with 2000 stations reporting for 128 consecutive days. In this scaling regime the spectral slope (fig. 4-3) estimated by linear regression is $\beta \approx 0.4$. We will use this value later in conjunction with estimation of α and C_1 to compute the parameter H. It will certainly be interesting in future studies to extend this analysis in both directions, especially if we consider that both (most obvious) forcing frequencies of the system are missed. i.e. the daily and annual cycles.

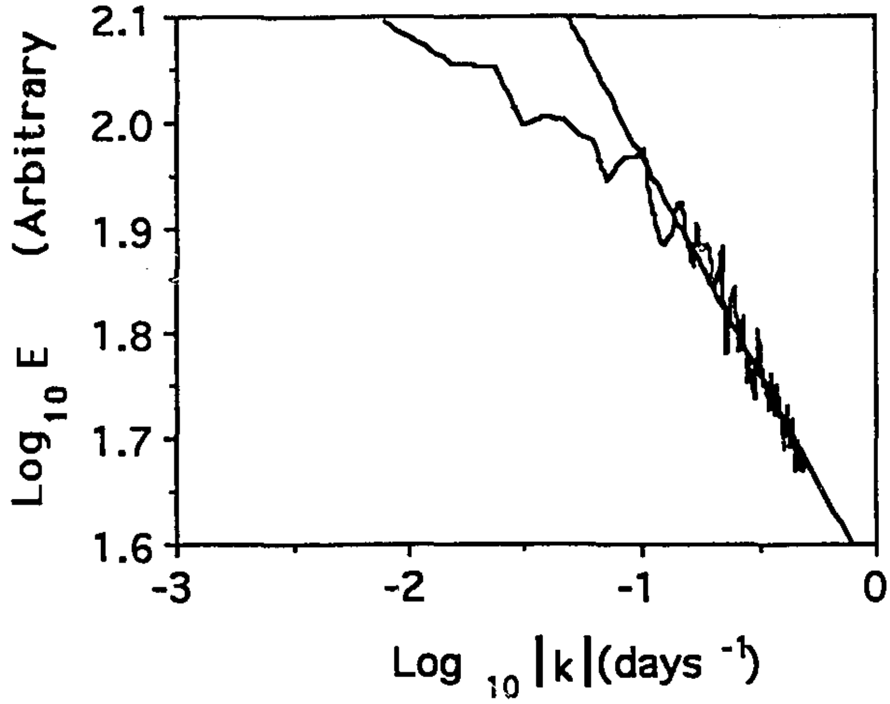

Figure 4-3: Averaged power spectrum for 128 days time series of 2000 sites around the world. The estimated spectral slope is $\beta \approx 0.4$.

IV.4 DTM analysis of raingage data

The estimation of the universal multifractal parameters is one of the most interesting points. For α and C_1 it could be most efficiently performed by the DTM method that we already used in preceding chapters. We calculated the double trace moment in 1D for a period of 128 days, accumulating histograms for 2000 stations. Figure 4-4 shows log $\mathrm{Tr}\left(\left(\varphi_\lambda^\eta\right)^q\right)$ vs log λ for $q = 2.0$. Again, we observe a break around 16 days in the scaling. In order to increase the statistics we performed the DTM on series of 64 days for 4000 stations. Since the log $\mathrm{Tr}\left(\left(\varphi_\lambda^\eta\right)^q\right)$ vs log λ curves looked very similar to the 128 day case we produce only the log $|K(q, \eta)|$ vs log η curves on figure 4-5. From these we deduce, using the 1 to 16 days region, $\alpha \approx 0.5$, $C_1 \approx 0.6$, Recently, many other analyses have corroborated this estimate. Glancing at table 4-1 should provide convincing evidence that α lies in the vicinity of 0.5. We also report a figure (fig. 4-6) taken from Schmitt et al where the same values are observed for a 40 years series recorded in Nîmes (France) The third parameter H can easily be determined by formula 2.21. We obtain H ≈ 0.05±0.1.

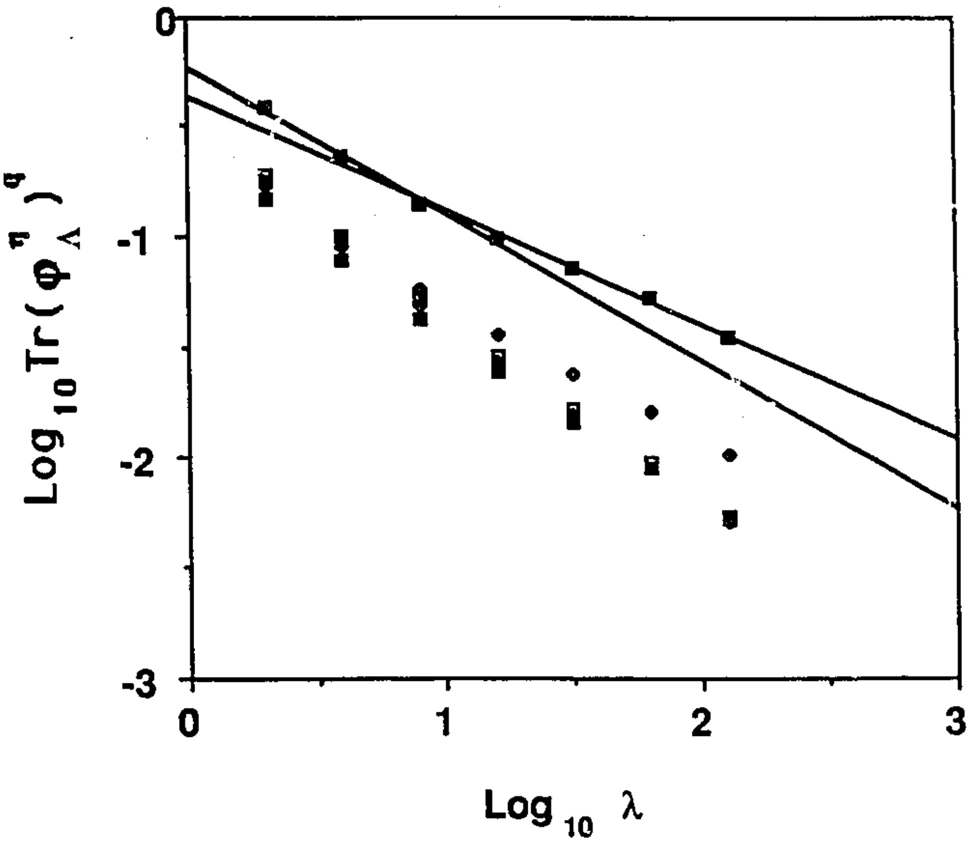

Figure 4-4: $\log\left(\mathrm{Tr}_\lambda\left(\varphi_\Lambda^\eta\right)^q\right)$ versus $\log(\lambda)$ for several values of η (from top to bottom, η = 1.2, 0.7, 0.3, 0.1) for time series of rainfall 128 days for 2000 stations, We used $q = 2.0$.

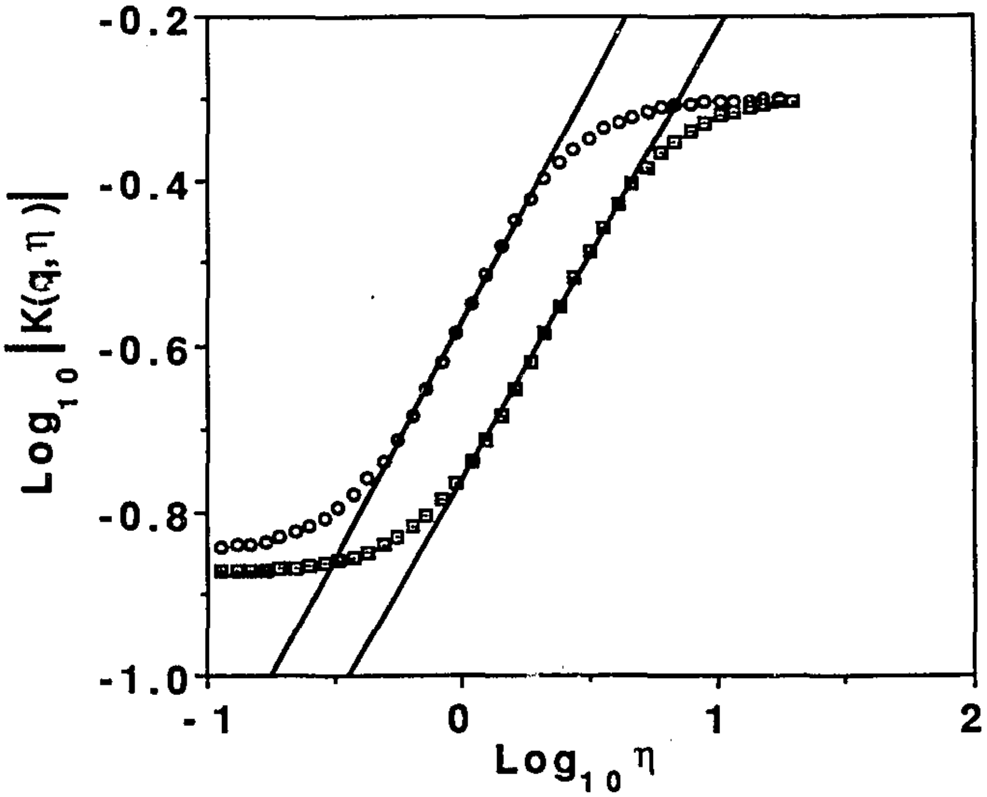

Figure 4-5: log(|K(q,η)|) versus log(η) for daily rainfall accumulations on a global network were we have considered the time series of 64 days for each station and accumulated statistics for 4000 stations. We used $q = 2.0$ (circles) and $q = 0.5$ (squares). The regression line gives a value of $\alpha = 0.5$ and $C_1 = 0.6$.

	Gage, daily accumulation	Gage, 6 minutes resolution	Gage, daily accumulation	Gage, daily accumulation	Gage, 15 minutes resolution	Mean and standard deviation
Location	Global Network	Réunion Islands (France)	Nîmes (France)	Dédougou (Burkina Faso)	Alps (France)	
Stations	4000	1	1	1	28	
Duration	1 year (scaling regime up to 16 days	1 year (scaling regime up to 30 days	40 years (scaling regime up to 16 days	45 years	4 years	
α	0.5	0.5	0.45	0.59	0.50	0.51±0.05
C_1	0.6	0.20	0.6	0.32	0.47	0.44±0.16
γ_0	1.20	0.40	1.09	0.78	0.94	0.88±0.30
γ_s	0.84	0.36	0.83	0.57	0.72	0.66±0.18
reference		Hubert et al [48]	Ladoy et al [121]	Hubert et al [48]	Desurosne et al [24]	

Table 4-1: Values of the universal multifractal parameters as evaluated by different authors on different data sets.

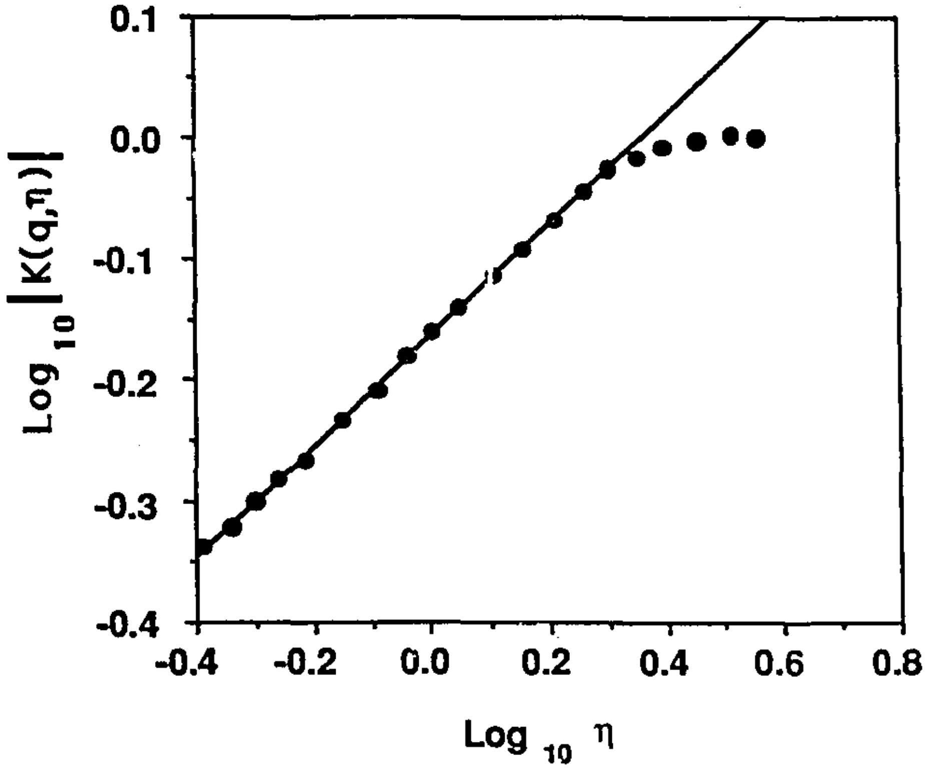

Figure 4-6: log(|K(q,η)|) versus log(η) with q = 2.0, for daily rainfall accumulations recorded in Nîmes (France) for a period of 30 years. The regression line gives a value of $\alpha = 0.5$ and $C_1 = 0.6$. (Kindly provided by F. Schmitt, P. Ladoy).

IV.5 Extreme Rainfall Events

In Hubert et al [48] we used the empirical evidence for a value of $\alpha \approx 0.5$ independent of the geographic location to explained a curve that could be found in just about any hydrology book (Jennings [51], Gilman [38], Paulhus [95], Remenieras [100], Raudkivi [99]) but that still lacked an explanation. We reproduce this curve on fig. 4-7. On this graph we see that for world record rainfall events the log of the accumulated rain against the log of the duration of the events seems to fall more or less on a line of slope near 0.5. This could be explained in the following manner: consider the extreme rainfall events occurring within a duration τ. Whenever there is a maximum order of singularity γ_{max}, then the maximum accumulation A_λ will be:

$$A_\lambda = \lambda^{-1} R_\lambda \approx \lambda^{\gamma_{max}-1} \approx \tau^{1-\gamma_{max}} \tag{4.1}$$

which gives a straight line of slope $(1-\gamma_{max})$ in log-log ($\gamma_{max} = 0.5 \pm 0.1$).

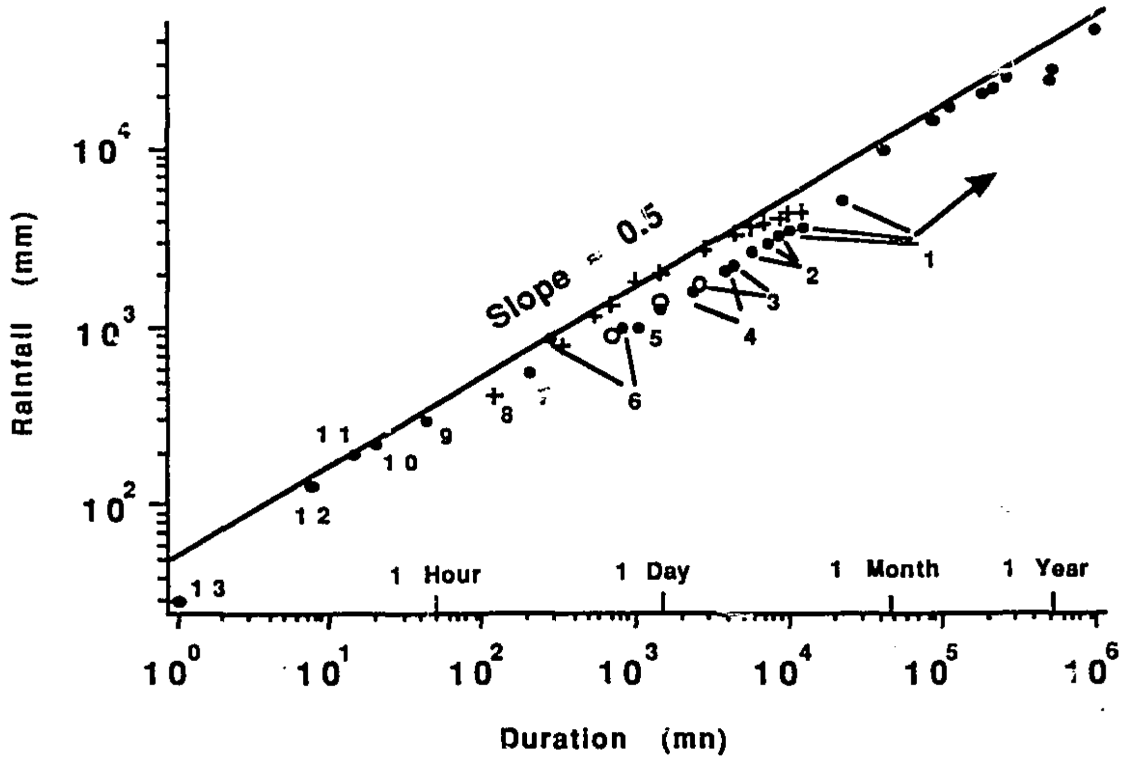

Figure 4-7: The world's record point rainfall values, reproduced from Raudkivi [99]. 1 - Cherrapunji, India; 2 - Silver Hill Plantation, Jamaica; 3 - Funkiko, Taiwan; 4 - Baguio, Philippine Is.; 5 - Thrall, Texas; 6 - Smethport, Pa; 7 - D'Hani, Texas; 8 - Rockport, W.Va; 9 - Holt, Mo.; 10 - Cutea de Arges, Romania; 11 - Plumb Point, Jamaica; 12 - Fussen, Bavaria; 13 - Unionville, Md.; values from Jennings Jenning, [51]. (+) La Reunion, France; (o) Paishih, Taiwan; values from Paulhus [95]. Reproduced from Hubert et al [48].

There are many mechanisms which can give rise to finite γ_{max}. For universal multifractals, when $\alpha \geq 1$, the orders of singularities are unbounded, however when $0 \leq \alpha \leq 1$ there is a finite maximum order of singularity γ_0 given by:

$$\gamma_0 = \frac{C_1}{1-\alpha} \tag{4.2}$$

The limitation of the observable space due to a finite sample that has been discussed in section III.2.2.3 could also produce a γ_{max}. Again, using the concept of sampling dimension $D_s = \log N_s / \log \lambda$ where N_s is the number of samples and λ the ratio between the largest and smallest scales. The dimension of the probability space explored is $D+D_s \leq c(\gamma)$. For time series $D = 1$. The maximum attainable γ yielding a non-negative dimension is

$$\gamma_s = c^{-1}(D+D_s) = \gamma_0\left[1-\alpha\left(\frac{C_1}{D+D_s}\right)^{-1/\alpha'}\right] \tag{4.3}$$

for $\alpha < 1$, $\alpha'<0$ the following inequality is satisfied:

$$\gamma_0\left[1-\alpha\left(\frac{C_1}{D+D_s}\right)^{-1/\alpha'}\right] \le \gamma_s \le \gamma_0 \tag{4.4}$$

where the upper bound corresponds to an infinite sample size ($D_S \to \infty$) and the lower bound to a single sample ($D_S = 0$).

From table 4-1 we obtain that $\alpha = 0.51 \pm 0.05$, $C_1 = 0.44 \pm 0.18$. Using the α and C_1 values (and with $D = 1$, $D_S = 0$), we can make the various estimates of γ_0, γ_s reported in table 4-1 from which we get $\gamma_s = 0.54 \pm 0.20$. We see that within one standard deviation this is equal to the value deduced from fig. 4-7 ($\gamma_{max} = 0.5 \pm 0.1$). The estimates from γ_0 are also quite compatible $(1-\gamma_0) = 0.88 \pm 0.31$).

There exist presently two rather opposite views on extreme precipitation. One school of thought relies deeply on the notion of the "possible maximum precipitation" (PMP) considered as a physically based notion. In order to estimate the possible maximum precipitation at a given location (and implicitly at a given scale) a sophisticated analysis of the rainfall process in an attempt to address all its relevant and physical aspects (meteorology, orography, etc.) is required. However, such an approach is often considered as remaining too speculative or qualitative, especially with respect to engineering needs.

On the other hand, supporters of statistical analysis consider rainfall rate as a random variable and time series as a stochastic process. Statistical approaches lead to rainfall rate probabilities useful in engineering designs. However, without any reference to any physical processes, the role of hydrologists could easily be reduced to fitting empirical data to ad hoc statistical laws.

These early results may help to reconcile the two points of view since they are based on both physics and statistics. Indeed, in our approach the multiplicative cascade accounts for turbulent processes resulting from nonlinear interactions between different scales and fields and leads to the statistical description of rainfall (eqs.2.4, 2.11, 2.12). We are thus able to give a precise (statistical) definition of the possible maximum precipitation at a given scale: we not only clarify the role of scales for the definition of the PMP, but also the role of the limited size of samples used for its estimation. We furthermore showed that the two basic multifractal exponents (C_1, α) determine the maximum attainable singularities (γ_0 and γ_s) and hence the possible maximum precipitation at a given scale and on a given sample.

IV.5 Scaling Limits and Phase Transitions

It is important to identify when universality is respected, when it is not and the statistical mechanism responsible for breaking universality. In this section we will argue that divergence of moments cause a first order phase transition in the scaling functions. As explained in the previous chapter this can be seen on the $c(\gamma)$ vs γ curve (fig. 4-8). On this curve divergence of moments is manifested by a linear behavior of slope q_D = 1.9±0.2 following the tangent (at the point γ_D) to the theoretical curve calculated using the parameters $\alpha = 0.5$ and $C_1 = 0.6$ (obtained by the DTM method) and formula 2.11 from which we also deduce that $\gamma_D \approx 0.8$. This transition can also be observed on K(q) (fig. 4-9) At the point $q = q_D$ the slope is $\gamma_D = 0.8\pm0.1$ in agreement with estimates from $c(\gamma)$. However, the experimental points seem to follow reasonably well the theoretical curve for K(q) (without divergence) far above this limit. There is also appearance of linearity in K(q) for large q. This is expected since in the limit $q \to \infty$, for $\alpha < 1$, K(q) becomes linear with a slope of $C_1\alpha'/\alpha \approx 1.2$ (around q =10 it looks like a linear region of slope ≈ 1.0). We think that using a larger sample (a few orders of magnitude larger) should make the divergence more apparent. In the low q region using the first few points of K(q) (fig. 4-10) we can get a rough estimate of the smallest γ that can be detected because of noise problems. We estimate this limit to be of the order of $\gamma_{min} \approx 0.09$, using universality relations (eq. 2.11) it corresponds to $q_{min} \approx 0.3$.

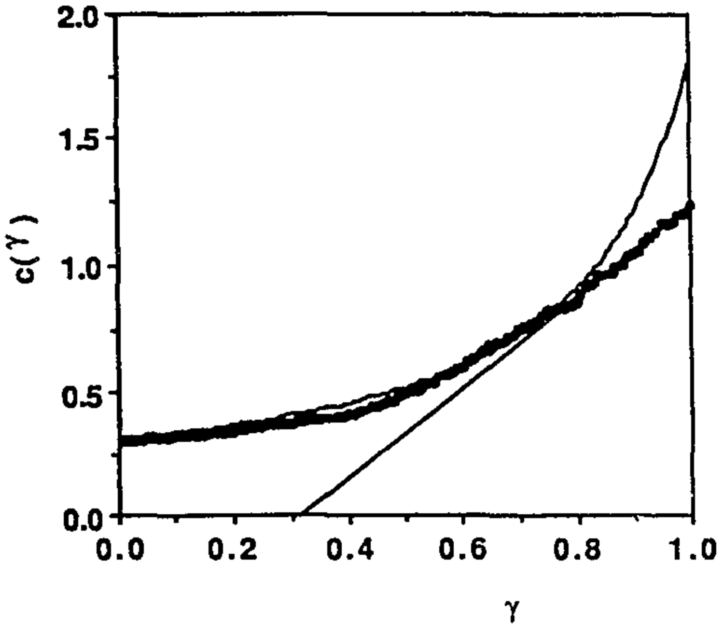

Figure 4-8: $c(\gamma)$ vs γ for 1-16 days scaling regime of 4000 stations around the world. The straight line as slope slope $q_D = 1.9 \pm 0.2$.

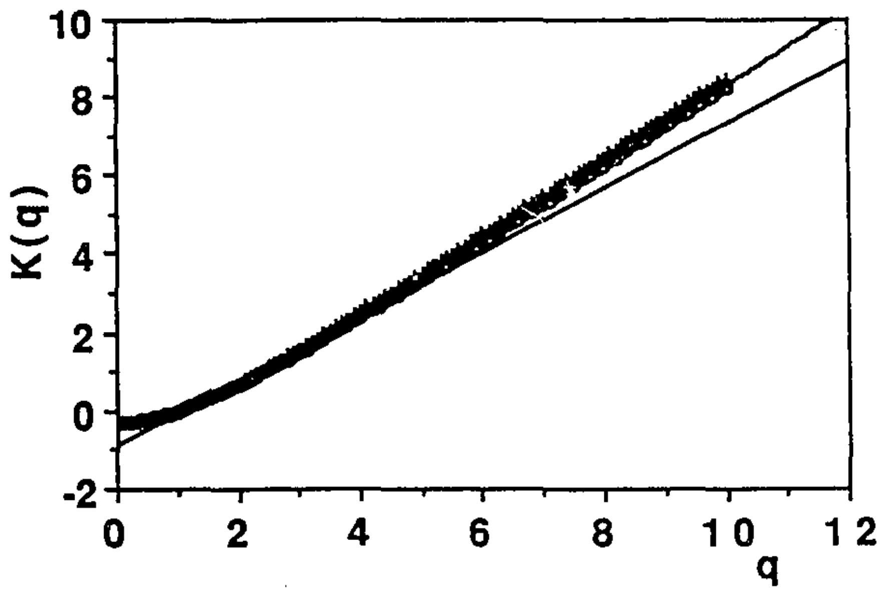

Figure 4-9: $K(q)$ vs q for 1-16 days scaling regime of 4000 stations around the world. The theoretical curve for $\alpha = 0.5$ and $C_1 = 0.6$ is given by the dashed line and the tangent at the point $q = q_D = 1.9$ is given by the straight line.

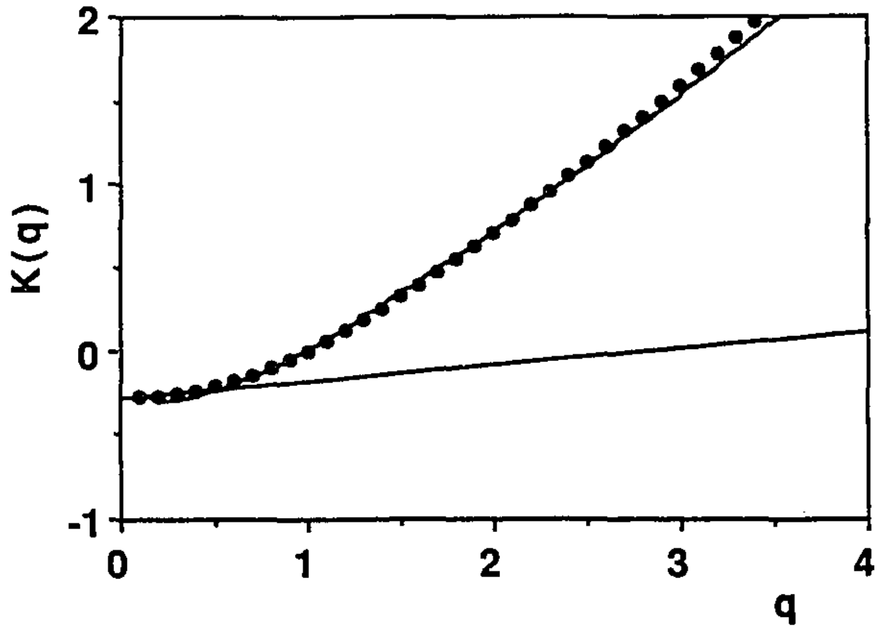

Figure 4-10: K(q) vs q for 1-16 days scaling regime of 4000 stations around the world. The line of slope $\gamma_{min} \approx 0.09$ is also shown.

IV.6 DTM on radar reflectivities:

The fixed vertical radar offered the possibility to study the scaling in the vertical direction but it also provided good temporal data of the reflectivities that we had just begun to explore in chapter 2. We will now estimate the universal multifractal parameters for this dataset. We have already indicated that the temporal scaling is well respected (fig. 2-24). We applied DTM analysis (on the modulus of the gradient) of a section of duration 8192 x 2.5 secs (i.e., 5 hr., 41 min., 20 sec.) and we accumulated statistics for the 256 levels closest to the ground. In fig. 4-11 we show the log of the trace moment of order q against the log of the scale ratio λ for different values of the exponent η. Again, it can be seen that we obtained scaling over the range of 3 orders of magnitude in λ (60 to 20,000 sec). In fig. 4-12 we show log $|K(q,\eta)|$ vs. log η for q = 0.5 and q = 2.0 from which we deduce $\alpha \approx 0.7\pm0.2$ and $C_1 \approx 0.5\pm0.2$. The spectral slope for the radar scans was already found to be $\beta \approx 1.2$ (fig. 2-24) which gives (using the above values of α and C_1) a value of $H \approx 0.4$ (this is close to the value $H \approx 0.5$ found in Lovejoy [62] for isolated rain storms evolving in time using probability distributions, see Lovejoy and Mandelbrot [66]).

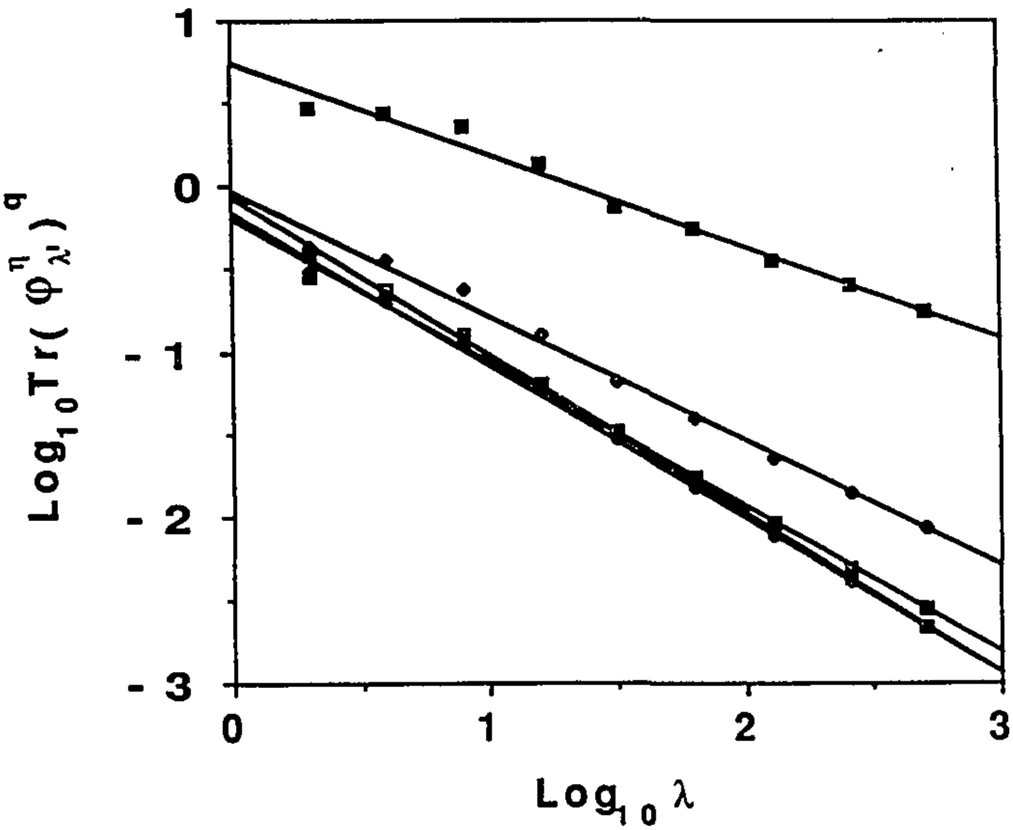

Figure 4-11: $\log\left(Tr_\lambda\left(\varphi^{\eta}_{\lambda'}\right)^q\right)$ versus $\log(\lambda)$ for several values of η (from top to bottom, η = 2.1, 1.1, 0.6, 0.4, 0.2) for the gradient of radar reflectivities against time and statistics accumulated for different elevations. We used $q = 2.0$.

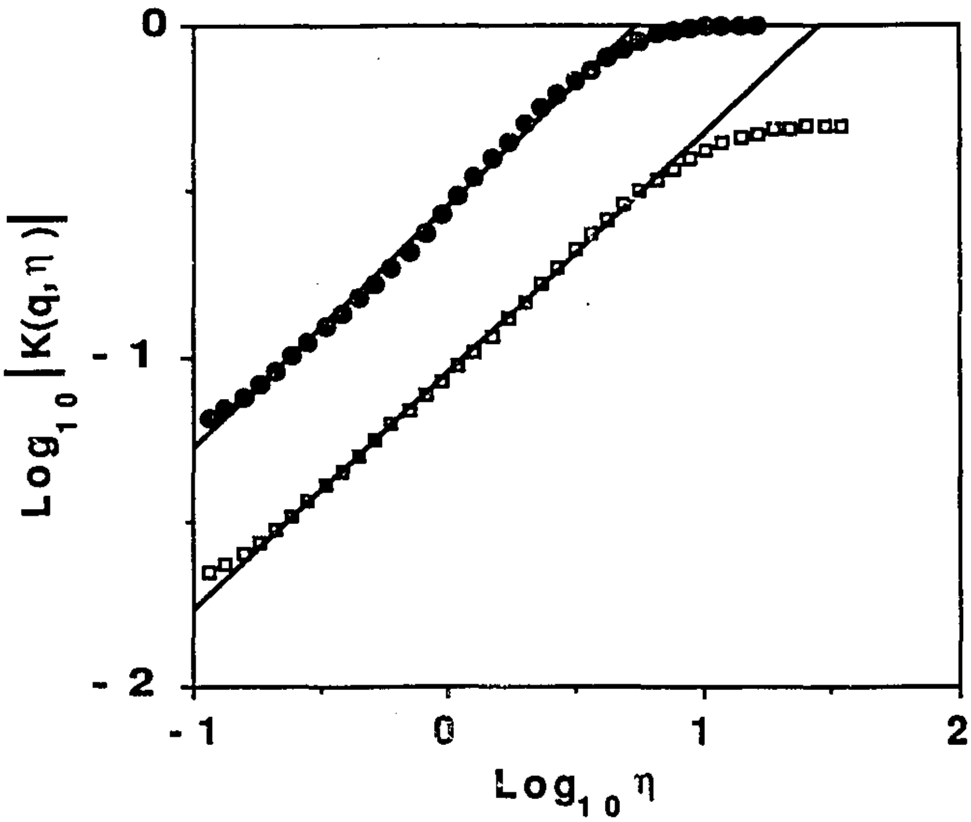

Figure 4-12: log(|K(q,η)|) versus log(η) for the gradient of the radar reflectivities against time and statistics accumulated for different elevation. The empty squares are for $q = 0.5$ and the filled circles are for $q = 2.0$. From the regression lines we deduce $\alpha = 0.7$ and $C_1 = 0.3$.

IV.7 The theoretical Framework for space/time transformations: Generalized Scale Invariance

If, as we argued, the scaling of cloud radiance, rain reflectivities and other atmospheric fields continues from small scales right through the mesoscale (there is no mesoscale gap), then no large scale forcing velocity can be appealed to in order to transform from space to time, and turbulent velocities must be used instead. At scale λ they will have amplitudes $v_\lambda \approx \langle\varepsilon_\lambda{}^{1/3}\rangle\lambda^{-1/3}$ where λ^{-1} is the scale of the eddy, ε_λ is the energy flux through the eddy to smaller scales (eq. 2.1 with $l = \lambda^{-1}$). Although $\langle\varepsilon_\lambda\rangle$ is scale independent, $\langle\varepsilon_\lambda{}^{1/3}\rangle \approx \lambda^{K(1/3)}$. Since K(1/3) is small compared to 1/3, we will write it as δ. Rather than being scale independent, the space-time transformation will thus have a scale dependent velocity[1] $v_\lambda \approx \lambda^{-H}$ with $H \approx 1/3+\delta$. The two geophysically relevant Taylor's hypotheses therefore correspond to H=0 or $H=1/3+\delta$ depending on the existence (or not) of the "gap".

The theoretical arguments mentioned above make it clear that the turbulent velocity is likely to be the relevant one for space-time transformations. The space-time transformation we infer from the turbulent value of H ($\approx 1/3$) can be easily expressed in the formalism of Generalized Scale Invariance. Consider (x, y, t) space, the space-time transformation can be simply expressed by statistical invariance with respect to the following transformation: $x \to x/\lambda$, $y \to y/\lambda$, $t \to t/\lambda^{1-H}$ or using the notation $r=(x,y,t)$, $r_\lambda = \mathbf{T}_\lambda r_1$ with $\mathbf{T}_\lambda = \lambda^{-G}$ and:

$$G = \begin{bmatrix} 1 & 0 & 0 \\ 0 & 1 & 0 \\ 0 & 0 & 1\text{-}H \end{bmatrix} \tag{4.5}$$

The matrix G could also have off diagonal elements to account for stratification and rotation. The elements of this matrix G could be identified using the Monte-Carlo Rotating ellipse technique. Pflug et al. [97] used successfully this technique to classify satellite cloud images according to the amount of stratification and rotation present. This formalism when applied to the space-time problem is expected to be quite complex since α for the velocity field is ~ 1.3 (Schmitt et al. [119]) and we have already seen that α is different in time and space for the rain field.

IV.7. Comparison of Temporal and Spatial scaling exponents

In our analyses we obtained $\alpha \approx 0.6 \pm 0.2$ for all the time series of fields related to rainfall that have been analyzed. In spatial analysis radar scans and daily rainfall accumulations both give $\alpha \approx 1.4 \pm 0.1$. The agreement on the values of this fundamental parameter coming from disparate types and sources of data gives us confidence in these

---

[1] Each moment of the rain field will require a different δ. For simplicity, we ignore this complication here.

values, although the theoretical reasons why we should get agreement between doesn't stand on firm ground. It is interesting to compare these results to those obtained for cloud radiances. If we take the mean of all the visible and near infra red images we get $\alpha \approx 1.15 \pm 0.2$ and if we take the mean of all the thermal IR images we get $\alpha = 1.3 \pm 0.2$ which are both (to within statistical uncertainty) close to the $\alpha = 1.4$ value, especially if we consider all the poorly understood effects that could bias our estimates of α discussed in section 4.1. In this case there is less *a priori* reason to expect the existence of simple statistical relation between rain and radiance singularities, although if the values of α were the same such a relation might indeed exist.

The finding that the values of α for spatial and temporal processes belong to qualitatively different classes of probability distribution (unconditionally hard, $\alpha > 1$, conditionally soft, $\alpha < 1$) has profound consequences because it means that we will observe qualitatively different multifractal behavior in space and in time. Since $\alpha < 1$, there will be a maximum order of singularity $= C_1/(1-\alpha) \approx 1.2$ in time (see section 2.3) whereas in space, γ is unbounded (actually in both cases we will obtain hard multifractal processes since even in time $C_1/(\alpha-1) > 1$ implies a finite q_D. We classify the multifractals in time as being conditionally soft and those in space as being unconditionally hard. This distinction may also have consequences for the interpolation and extrapolation problem ("objective analysis" and "forecasting").

Chapter V

Conclusion

In times of the ecological awareness of society it becomes very important to recognize the basic properties of the atmosphere. We realize the immensity of this task, even concentrating on a single constituent (water), it is still a formidable enterprise. The fundamental knowledge of invariant properties of atmospheric fields, and water in particular, are still debated. The standard model of atmospheric motions proposed two regimes, one of two dimensional and one of three dimensional turbulence separated by a transition zone (the mesoscale gap). It will certainly be very hard to reconcile this theory with the experimental evidences presented here indicates the absence of this gap. In view of this we adopted the alternative unified scaling model, that involves no such transition. In this model, turbulent fields that are produced by cascade processes and generally result in universal multifractals. The different analyses we performed convinced us that the different fields related to atmospheric water are good examples of such turbulent fields.

We applied conventional energy spectra on a significant number of NOAA-9 AVHRR images which covered scales (1-512 km) where the standard model predicted a scaling break ($\approx$ 10 km). We extended the investigated range with a few LANDSAT MSS and METEOSAT images. We effectively studied scaling from 160m to 4000 km and no evident scaling break was found, this is a strong support of the unified scaling model. We also used the new Double Trace Moments method to analyze scaling. With this method we showed that the cloud radiances in all available wavelengths are consistent with universal exponents α between 1.1 ± 0.05 and 1.35 ± 0.05, $C_1 = 0.1 \pm 0.02$ and H between 0.3 ± 0.05 and 0.5 ± 0.05 with some variations depending on the wavelength of the sensors. Although we conclude that the evidence for horizontal scaling is good, it should be stressed that enormous, systematically sampled data sets will be needed to fully characterize the scaling of atmospheric fields as well as their limits. This study provides an early exploration of what is largely unknown territory.

Moving on from the horizontal scaling of cloud radiances, we analyze data from a vertically pointing radar measuring reflectivities of rain with a resolution of 2.5 seconds in time, 21m in space. Here the corresponding scale ratios (the largest divided by the smallest scale) were 2^{13}, and 2^{8} respectively. In time, the scaling was well followed over the range of nearly ~20 to 20000 secs. In the vertical, the scaling was followed at high frequencies, but we found a spectral bump corresponding in size ($\approx$1 km) to the thickness of the bright band which was present throughout the sequence. Since other studies with larger samples (e.g., 20 cases instead of one) found vertical scaling over the corresponding range, the bump is likely to be consistent with statistical (sample to sample) fluctuations. This conclusion is supported by a space/time DTM analysis which yielded very similar universal multifractal parameters in global daily rainfall accumulations (for 1983). Specifically, the degree of multifractality (characterized by α) was found (within experimental error) to be the same for the in situ gage measurements and the radar reflectivities. We estimated that $\alpha \approx 0.5$ in time and 1.4 in space. This is perhaps not surprising since α is invariant under the operation of taking powers (such as the Marshall-Palmer Z-R relation).

The search for spatial scaling from records of daily rainfall accumulation lead us to consider the problem of removing the bias introduced by the presence of a sparse measuring network. We realized that conventional objective analysis methods for treating the problem such as Kriging made the more or less implicit unrealistic assumptions of homogeneity and regularity of the field and the network. We developed a new method that replaces these by scaling assumptions. We called this technique "multifractal objective analysis". Further more, in these conventional methods the network is generally considered as a fixed ("deterministic") object, we considered it as a realization of a stochastic multifractal process. This hypothesis seemed to be justified over the range of scales from 200 km to 8000 km. Furthermore, it could be well described with universal scaling exponents $\alpha = 0.85\pm0.2$, $C_1 = 0.2\pm0.1$ and $H = 0.0\pm0.1$. This is also an improvement on (mono)fractal, since with these parameters all the statistical moments of the density of stations field could be obtained. Since the resulting field is certainly dressed, this description is valid between moments of order $q_{min} = 0.6\pm0.2$ and $q_D = 3.6\pm0.1$, at these points phase transitions occurs due to detectability (noise) limits (q_{min}) and to divergence of moments (q_D) that cause a first order transition thus limiting the range of q where universality can be observed.

There is more and more evidence, including that presented in this thesis, that different fields related to atmospheric water are multifractal. It seems natural to suppose that the rainfield is no exception. The objective analysis problem can be stated in terms that are very likely shared by numerous geophysical experimentation: how to get the most information on a multifractal field with a multifractal network. In this first study we assumed uncorrelated field and networks (leaving for future development this problem). In this view, the measured field is the product of the analyzed field and the density of stations. This leads us to simple additive corrections on the scaling exponents describing the scaling of the different statistical moments. It allowed us to deduce the scaling properties of the analyzed field from the scaling properties of the measured field and the network. Scaling was observed on the measured field in the range of scales from 400 to 8000 km. The universal multifractal exponents obtained after correcting for the presence of the network are $\alpha = 1.35\pm0.2$, $C_1 = 0.15\pm0.1$ and $H = 0.2\pm0.3$. The critical order of statistical moments are the detectability lower limit $q_{min} = 0.2\pm0.3$ and the divergence of moments (first order) phase transition point $q_D = 2.0\pm0.3$.

We discussed at length the spatial properties but all these fields vary considerably in time. Global rainfall daily accumulations provided important information on this aspect also. We observed that in time there are two distinct scaling regimes with a transition at time scales of 10 to 20 days which corresponds to the "synoptic maximum" where such a symmetry break is expected due to the finite size of the earth. Using the time series we got $\alpha = 0{,}5$, $C_1 = 0.6$ which is in agreement with other works. Again three regions were seen. One below $q_{min} = 0.3 \pm 0.1$, one above $q_D = 1.9 \pm 0.1$ and one between where the bare and dressed properties are the same.

The fact that α and C_1 for the rainfield are so different when evaluated from a time series and when evaluated from a spatial field called for a review of the theories about space-time transformation of a turbulent field. Such transformations like the Taylor's "frozen turbulence" concept needs to be revisited to account for theses different statistical behavior. Another question that we will have to address is: what is exactly the accuracy of the method? The answer to this question will have to rely on simulation and further theoretical development. For the moment, simulating the field and the measuring process is the easiest way to get a good idea of the accuracy of the parameters we have estimated.

We sketched how our empirically determined multifractal exponents, combined with appropriate space/time transformations can enable us to make dynamical multifractal simulations. These simulations will be necessary to further our understanding of the underlying atmospheric dynamics. They will help us tame the ubiquitous extreme atmospheric variability, and may have far reaching implications for remote sensing, objective analysis, and (stochastic) forecasting.

Also being able to do simulations which have realistic variability and scaling behavior, that are able to explain even the scaling breaks induced by the measuring network will be of great help in designing and exploiting measurement networks for geophysical quantities. It will also help in testing and improving the current and future objective analysis schemes used to produce maps used in weather and hydrologic forecasting.

We identified the range of scales where scaling is observed for different fields related to atmospheric water. We calculated the universal multifractal exponents for these fields and identified different phases of scaling and their critical points. The exact numerical value of the parameters may prove to be not so important but a fundamental point that should be remembered is that scaling symmetries which were mostly hypothesis derived from phenomenological models of turbulence showed up in the fields we analyzed. These symmetries can be exploited. As an example, we used the scaling symmetries of a sparse network to deduce the symmetries of the rainfield. In the future, these properties will certainly prove useful in estimating missing data points (the old concept of objective analysis) and in prediction scheme. The utility of such objective analysis techniques will certainly outpass the hydrometeorologic studies on which this thesis was centered and find applications in many fields where a sparse network is used to collect measurements. The knowledge gained on the variability of atmospheric water fields should also be considered in planetary water, radiation and energy budget which are so important for global warming (or cooling) studies.

Appendix A

Faster Box-Counting Algorithm

A.1 The Hunt and Sullivan Algorithm

When dealing with very large dataset in more than one dimension performing calculations of the box-counting type could easily become out of hands. The algorithm presented in this section greatly reduce the memory requirement and the speed of computation. When performing computations like box-counting or evaluating diverse statistical moments at different resolution (like we did in the trace moment analysis) the majority of boxes are empty. These zeros take a lot of place (and time) this algorithm adapted from the box-counting algorithm of Hunt and Sullivan [49] present an efficient way to avoid allocating memory and spending computation time on the zeros.

For purpose of exposition we take the embedding dimension d = 1 and Q ∈ [0,1], where Q is a compact point set contained in the unit cube of Euclidean dimension d. The interval [0,1] can be associated with a binary tree. On the first level is the entire interval. Level 1 has two branches for the half intervals; level two has four branches, etc.

Each point x of Q is associated with a path p(x) in this tree determined by the binary expansion of x. Since the position of x has finite precision, the tree has only finitely many levels. If Q is a set of uniformly distributed random numbers, all paths in the finite tree are equally likely. In case Q is not uniformly distributed the situation is different, paths do not have equal weight, and in fact some paths never occur.

The following method was developed: Begin with an empty tree. For each x ∈ Q create a path p in T by adding nodes and left or right branches as needed, according to the binary expansion of x. As new nodes are added record their levels. Early in the computation when only a few elements of Q have been added to the tree, most branches will call for the creation of new nodes. Later many nodes will be already occupied. As the calculation proceed it is easy to keep a record of the total number of paths which have passed through a given node. After the tree has been constructed statistics can be gathered.

For the points distributed on a sphere, assume that $Q \in [0,2\pi] \times [-1,1]$. Each point is a pair (θ,z) of real numbers. Denote the binary expansion of θ by $b_1b_2......b_k....$ and the expansion of z by $a_1a_2.....a_k....$ A unique base-4 number q with expansion $q_1q_2....q_k....$ can now be generated according to the prescription

$$q_k = b_k + 2a_k \quad (4.19)$$

Now, sort the base-4 numbers for the different measurement points. As you inspect this array at a certain level ℓ you know that you hit a "box" that has not been visited if the expansion of the coordinate of the point is not the same as the expansion for the coordinates of the previous point. Calculating the statistical moments of order q at a resolution k is simply done by adding all the measurements with the same address, take the q^{th} power and average for all the boxes, but don't forget the empty boxes!

Proceeding in such a manner has the great advantage that you allocate memory space only for non-empty boxes Regardless of the embedding dimension the algorithm will perform at the same speed for the same number of measurement points. This is sometime a limiting factor in this type of analysis.

To get statistics at other scale λ what can be done is to perform other expansion of the coordinates than just binary. For example in our study we also used base 3 and base 5 expansions.

Appendix B

Digression On Anisotropy

B.1 The Anisotropy of the Network

In order to quantify the anisotropy in the scaling of the measuring network we partitioned the axis of the globe into slices of equal z (where z is the length of the projection of the slice onto the axis that goes from the center of the earth to the north pole) so that the area of the intersection of each slice with the earth's surface will be the same. We partitioned the earth in such a fashion because we need to perform the analysis on one dimensional intersections of the original set. The codimensions are invariant under intersection, so that corresponding dimensions will simply be reduced by 1. In contrast taking one dimensional projections (i.e. just considering the latitudes of stations irrespective of longitude will have dimension 1, since the measuring stations have dimension > 1, and hence will be uninteresting. We performed a regular box-Counting analysis on each slice using the definition of distance that $L = |\theta_1 - \theta_2|$ and then we averaged the N(L) value for all slices. We then rotated the coordinate system and performed the same analysis in the other direction . For both analysis the results are shown on figure B-1. It could be seen that there is a small anisotropy in the measuring network since the fractal dimension calculated in the North-South direction is 0,85 and in the East-West direction we get 0,77. The anisotropy of the network could further be characterized by the use of the elliptical dimension D_{el} (Lovejoy et al. [1987], Schertzer and Lovejoy [1985, 1987]) which in this case is given by:

$$D_{el} = 1 + \frac{C_{N\text{-}S}}{C_{E\text{-}W}} = 1 + \frac{0.185 \pm 0.0035}{0.23 \pm 0.005} = 1{,}70 \pm 0.06 \qquad (2.2)$$

where $C_{N\text{-}S}$ and $C_{E\text{-}W}$ are the codimension in the north-south and east-west directions respectively; the codimension is the difference between the dimension of the embedding space (in our case 1.0) and the fractal dimension. If the network was isotropic we would have obtained $D_{el} = 2.0$. The accuracy of D_{el} is evaluated by assuming an accuracy of 1% on individual points from which we evaluated a minimum χ^2 line.

One way to generalize these results would be to introduce a scale changing operator (T_λ) where λ is the ratio between the two scales. Consider $r = (\theta,\varphi)$, $r_\lambda = T_\lambda r_1$ with $T_\lambda = \lambda^{-G}$ and: $G = \begin{bmatrix} a & b \\ c & d \end{bmatrix}$. The diagonal elements of the matrix G are related to the fractal dimension and the offdiagonal elements accounts for stratification and rotation. This formalism is known as generalized scale invariance. For satellite pictures, Pflug et al [96, 97] identified the elements of the matrix G using the Monte-carlo rotating ellipse technique. They used this to classify cloud images according to the amount of stratification and rotation present. This will very likely be the next step in the caracterization of the anisotropy of the network.

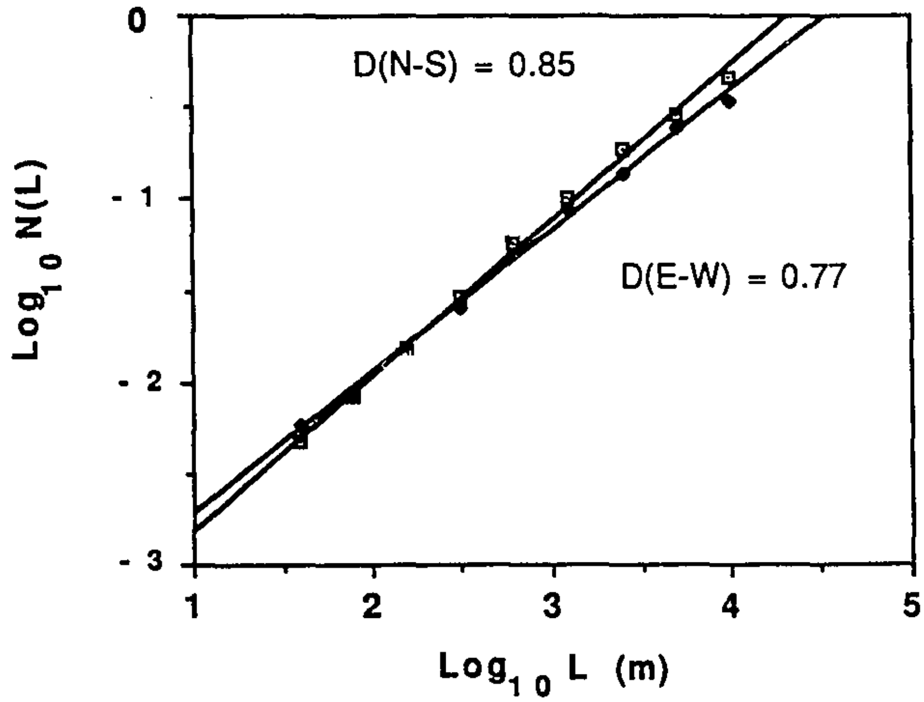

Figure B-1: Log of the number of pairs of station divided by the total number of boxes within a certain "Slice" averaged over all slices against the log of the distance for North-South oriented slices (empty squares) and East-West oriented slices (filled triangle.

Bibliography

[1] Atmanspacher, H., H. Scheingraber, and G. Weidenmann, "Determination of f(α) for a limited random point set," *Phys. REv. A*, vol. 40, 3954, 1989.

[2] Bacry, A., A. Arneodo, U. Frisch, Y. Gagne, and E. Hopfinger, "Wavelet analysis of fully developed turbulence data and measurement of scaling exponents," in *Turbulence and coherent structures*, Lessieur, M. and O. Metais, Eds. Kluwer, 1989, pp. 703-718.

[3] Bak, P., C.Tang, and K. Weiessenfeld, "," *Phys. Rev. Lett*, vol. 59, 381, 1987.

[4] Barnsley, M., *Fractals EveryWhere*. San Diego, Ca: Academic Press, 1988.

[5] Bellon, A., S. Lovejoy, and G.L. Austin, "A short term precipitation forecasting procedure using combined radar and satellite data," *Mon. Wea. Rev.*, vol. 108, 1554-1566, 1980.

[6] Beltrami, H., D. Lavallée, C. Hooge, S. Lovejoy, and J.C. Marechal, "Universal Multifractals in earthquakes," *Eos*, vol. 72, 279, 1991.

[7] Benzi, R., G. Paladin, G. Parisi, and A. Vulpiani, "On the multifractal nature of fully developped turbulence," *J. Phys. A*, vol. 17, 3521-3531, 1984.

[8] Blanchard, D.C., "Raindrop size distribution in Hawaiian rains," *J. of Meteor.*, vol. 10, 457-473, 1953.

[9] Bouquillon, C. and R. Moussa, "Caractérisation fractale d' une série chronologique d' intensité de pluie," in *Compte rendu des Rencontres Hydrologiques Franco-Roumaines, 3-6 sept.*, Ecole des Mines, Paris, France,, 1991, pp. 35-36.

[10] Bras, R.L. and I. Rodriguez-Iturbe, *Random Functions and Hydrology*. Addison-Wesley Publishing Company, 1985.

[11] Brax, P. and R. Pechanski, "Levy stable law description on intermittent behaviour and quark-gluon plasma phase transitions," *Phys. Lett. B*, vol. 253, 225-230, 1991.

[12] Brenier, P., "Simulation dynamique multifractale des nuages," Master's thesis, Ecole Nationale supérieure de techniques avancées, Paris, France, 1990.

[13] Brenier, P., D. Schertzer, G. Sarma, J. Wilson, and S. Lovejoy, "Continuous Multiplicative cascade models of passive scalar clouds," *Annales Geophysicae*, vol. 8 (special Edition), 320, 1990.

[14] Cahalan, R.F., "Landsat observations of fractal cloud structure," in *Non-linear variability in geophysics: Scaling and Fratals*, Schertzer, D. and S. Lovejoy, Eds. Kluwer, 1991, pp. 281-297.

[15] Chabra, A.B. and K.R. Sreenivasan, "Negative dimensions: Theory, computation and experiments," *Phys. Rev. A*, vol. 34, 1114, 1991.

[16] Come, J.M., "Caractérisation fractale des relations périmètre/surface des précipitations en zone Soudano-Sahélienne," Master's thesis, Ecole Nationale Supérieure des Mines de Paris, Paris, France, 1988.

[17] Corrsin, S., "On the spectrum of Isotropic Temperature Fluctuations in an isotropic Turbulence," *J. Appl. Phys.*, vol. 22, 469-473, 1991.

[18] Crane, R.K., "Space-time structure of rain rate fields," *J. Geophys. Res.*, vol. 95, 2011-2020, 1990.

[19] Cressman, G.P., "An operational objective analysis system," *Mon. Wea. Rev.*, vol. 87, 367-374, 1959.

[20] Creutin, J.D. and C. Obled, "Objective Analyses and Mapping Techniques for Rainfall Fields: An Objective Comparison," *Wat. Resour. Res.*, vol. 18, no. 2, 413-431, 1982.

[21] Daley, R., *Atmospheric Data Analysis*. Cambridge University Press, 1991.

[22] Davenprot, W.B. and W.L. Root, *An introduction to the theory of random signal and noise*. New York: McGraw Hill, 1958.

[23] Davis, A., S. Lovejoy, and D. Schertzer, "Radiative transfer in multifractal media," in *SPIE proceedings*, vol. 15581991, pp. 37-59.

[24] Desurosne, I., P. Hubert, and G. Oberlin, "Analyses Fractales et multifractales: Une étape vers la formulation d' un modèle prédéterministe des précipitations d' altitude," *prepared for Hydro. Continent.*, .

[25] Diskin, M.H., "On the computer evaluation of Thiessen weights," *J. Hydrol.*, vol. 11, 69-78, 1970.

[26] Duchon, J., "Interpolation des fonctions de 2 variables suivant le principe de la flexion des plaques minces," *Rev. Automat. Inf. Rech. Oper.*, vol. 10, no. 12, 5-12, 1976.

[27] Duncan, M., S. Lovejoy, F. Fabry, and D. Schertzer, "The Fluctuating Radar Cross Section (RCS) of Multifractal Scaterers," in *Proceedings of the 11th ICCP conference*, vol. 21992, pp. 997-1000.

[28] Duncan, M., S. Lovejoy, F. Fabry, and D. Schertzer, "Fluctuating radar cross-section of a multifractal distribution of scaterers," 1992, in preparation.

[29] Endlich, R.M. and R.L. Mancuso, "Objective Analysis of environmental conditions associated with severe thunderstorms and tornadoes," *Mon. Wea. Rev.*, vol. 96, 342-350, 1968.

[30] Falconer, K., *Fractal Geometry: Mathematical Foundations and Applications*. J. Wiley and Sons, 1990.

[31] Fan, A.H., "Chaos additif et multiplicatif de Levy," *C.R. Acad Sci. Paris*, vol. I, no. 308, 151-154, 1989.

[32] Feder, J., *Fractals*. New York, NY: Plenum Press, 1988.

[33] Frisch, U.P., P.L. Sulem, and M. Nelkin, "A simple dynamical model of intermittency in fully develop turbulence," *J. Fluid Mech.*, vol. 87, 719-724, 1989.

[34] Gabriel, P., S. Lovejoy, D. Schertzer, and G. Austin, "Multifractal Analysis of resolution dependence in satellite imagery," *J. Geophys. Res.*, vol. 15, 1373-1376, 1988.

[35] Gage, K.S., "Evidence for k-5/3 law inertial range in meso-scale two dimensional turbulence," *J. Atmos. Sci.*, vol. 36, 1979, 1979.

[36] Gandin, L., *Objective analysis of meteorological fields (Leningrad, Gridromet)*, 1963, English Translation: Jerusalem, Israel Program for Scientific Translation, 1965, .

[37] Gilchrist, B. and G. Cressman, "An experiment in objective analysis," *Tellus*, vol. 6, 309-318, 1954.

[38] Gilman, C.S., "Rainfall, section 9," in *Handbook of applied hydrology*, Chow, V.T., Ed. Mc Graw Hill, 1964, pp. 9-1,9-68.

[39] Giraud, R., F. Montariol, D. Schertzer, and S. Lovejoy, "The codimension function of sparse surface networks and intermittent fields," in *abstract vol. Nonlinear Variability in geophysics*, McGill University, Montréal (Québec), Canada, 1986, pp. 35-36.

[40] Goodin, W.R., G.J. McRae, and J.H. Seinfeld, "A Comparison of Interpolation Methods for Sparse Data: Application to Wind and Concentration Fields," *J. Appl. Meteor.*, vol. 18, 761-771, 1979.

[41] Grassberger, P., "Generalized dimensions of strange attractors," *Phys. Rev. Lett.*, vol. A 97, 227, 1983.

[42] Halsey, T.C., M.H. Jensen, L.P. Kadanoff, I. Procaccia, and B. Shraiman, "Fractal measures and their singularities: the characterization of strange sets," *Phys. Rev. A*, vol. 33, 1141-1151, 1986.

[43] Hentschel, H.G.E. and I. Proccacia, "The infinite number of generalized dimensions of fractals and strange attractors," *Physica*, vol. 8D, 435-444, 1983.

[44] Hovland, D., D. Dartt, and K. Gage, "An Objective Analysis technique for the regional air pollution study, Part I," Tech. Rep., , Research Triangle Park NC, , NTIS PB 266255, 1977.

[45] Hubert, P. and J.P. Carbonnel, "Caracterisation fractale de la variabilité et de l' anisotropie des precipitations tropicales," *C. R. Acad. Sci. Paris*, vol. 2, no. 307, 909-914, 1988.

[46] Hubert, P. and J.P. Carbonnel, "Dimensions fractales de l' occurence de pluie en climat Soudano-Sahélien," *Hydro. Continent.*, vol. 4, 3-10, 1989.

[47] Hubert, P. and J.P. Carbonnel, "Fractal characterization of intertropical precipitations variability and anysotropy," in *Non-linear variability in geophysics: Scaling and Fratals*, Schertzer, D. and S. Lovejoy, Eds. Kluwer, 1991, pp. 209-213.

[48] Hubert, P., Y. Tessier, P. Ladaoy, S. Lovejoy, D. Schertzer, J.P. Carbonnel, S. Violette, I. Desurosne, and F. Schmitt, "Multifractals and extreme rainfall events," *Geophys. Res. Lett.*, vol. 20, no. 10, 931-934, 1993.

[49] Hunt, F. and F. Sullivan, "Efficient Algoritms for Computing Fractal Dimensions," in *Dimension and Entropies in Chaotic Systems*, G., M.K., Ed. Springer-Verlag, 1986, pp. 74-81.

[50] Hurst, H.E., "Long-term storage capacity of reservoirs," *Trans. of the Amer. Soc. of Civil Eng.*, vol. 116, 770-808, 1951.

[51] Jennings, A.H., "World's greatest observed point rainfall," *Monthly Weather Rev.*, vol. 78, 4-5, 1950.

[52] Kolesnikov, V.N. and A.S. Monin, "Spectra of meteorological field fluctuations," *Izv. Atmos. Oceanic Phys.*, vol. 1, 653-669, 1965.

[53] Kolmogorov, A.N., "Local structure of turbulence in an incompressible liquid for very large Raynolds numbers," *Proc. Acad. Sci. URSS., Geochem. Sect.*, vol. 30, 299-303, 1941.

[54] Kolmogorov, A.N., "A refinement of previous hypotheses concerning the local structure of turbulence in viscous incompressible fluid at high Raynolds number," *J. Fluid Mech.*, vol. 83, 349, 1962.

[55] Ladoy, P., S. Lovejoy, and D. Schertzer, "Extreme Variability of climatological data: Scaling and Intermittency," in *Non-linear variability in geophysics: Scaling and Fratals*, Schertzer, D. and S. Lovejoy, Eds. Kluwer, 1991, pp. 241-250.

[56] Lamperti, J., "Semi-stable stochastic processes," *Trans. Am. Math. Soc.*, vol. 104, 62-78, 1962.

[57] Larnder, C. and K. Fraedrich, "Multifractal Analysis of Rainfall over Germany," 1992, Private communication.

[58] Lavallée, D., "Multifractal techniques: Analysis and simulation of turbulent fields," Ph.D. thesis, McGill University, Montréal (Québec), Canada, 1991.

[59] Lavallée, D., S. Lovejoy, and D. Schertzer, "Nonlinear variability and landscape topography: analysis and simulation," in *Fractals in geography*, Cola, L.D. and N. Lam, Eds. , 1991, pp. in press.

[60] Lavallée, D., S. Lovejoy, and D. Schertzer, "On the determination of the codimension function," in *Non-linear variability in geophysics: Scaling and Fratals*, Schertzer, D. and S. Lovejoy, Eds. Kluwer, 1991, pp. 99-110.

[61] Lilly, D.K., "Meso-scale variability of the atmosphere," in *Meso-scale Meteorology -Theories, Observations and models*, Lilly, D.K. and T. Galchen, Eds. D. Reidel, 1983, pp. 13-24.

[62] Lovejoy, S., "Analysis of rain areas in terms of fractals," in *20th conference on radar meteorology, AMS Boston*, vol. 15581981, pp. 476-484.

[63] Lovejoy, S., "Area perimeter relations for rain and cloud areas," *Science*, vol. 187, 1035-1037, 1982.

[64] Lovejoy, S., J. Tardieu, and G. Monceau, "Etude d' une situation frontale: analyse météorologique et fractale," *La Météorologie*, vol. 6, 111-118, 1983.

[65] Lovejoy, S. and D. Schertzer, "Generalized scale invariance and fractal models of rain," *Wat. Resour. Res.*, vol. 21, no. 8, 1233-1250, 1985.

[66] Lovejoy, S. and B. Mandelbrot, "Fractal properties of rain and a fractal model," *Tellus*, vol. 37A, 209, 1985.

[67] Lovejoy, S., D. Schertzer, and P. Ladoy, "Brighter outlook for weather forecasts," *Nature*, vol. 320, 401, 1986.

[68] Lovejoy, S., D. Schertzer, and P. Ladoy, "Fractal characterisation of inhomogeneous measuring networks," *Nature*, vol. 319, 43-44, 1986.

[69] Lovejoy, S. and D. Schertzer, "Scale invariance in climatological temperatures and the spectral plateau," *Annales Geophys.*, vol. 4B, 401-410, 1986.

[70] Lovejoy, S., D. Schertzer, and A.A. Tsonis, "Functional Box-Counting and Multiple Dimensions in rain," *Science*, vol. 235, 1036-1038, 1987.

[71] Lovejoy, S. and D. Schertzer, "Multifractals, Universality classes and satellite and radar measurements of cloud and rain fields," *J. Geophys. Res.*, vol. 95, 2021, 1990.

[72] Lovejoy, S. and D. Schertzer, "Fractals, rain drops and resolution dependence of rain measurements," *J. Appl. Meteor.*, vol. 29, 1167-1170, 1990.

[73] Lovejoy, S. and D. Schertzer, "Multifractal analysis techniques and the rain and clouds fields from 10-1 to 106m," in *Non-linear variability in geophysics: Scaling and Fratals*, Schertzer, D. and S. Lovejoy, Eds. Kluwer, 1991, pp. 111-144.

[74] Lovejoy, S. and D. Schertzer, "Multifractals and Rain," in *New Uncertainty Conceps in Hydrology and Water Ressources*, Kunzewicz, Z.W., Ed. Cambridge University Press, 1992.

[75] Lovejoy, S., D. Schertzer, P. Silas, Y. Tessier, and D. Lavallée, "The unified scaling model of atmospheric dynamics and systematic analysis in cloud radiances," *Annales Geophysicae*, vol. (in press), .

[76] MacCracken, M.C. and G.D. Sauter, "Development of an air pollution model for the San Francisco Bay Area," Tech. Rep., , , UCRL-51920, 229-230 [NTIS UCRL-51920], 1975, Vol. 2, appendices.

[77] Mandelbrot, B. and J.W.V. Ness, "Fractional Brownian motions, fractional noises and applications," *SIAM Review*, vol. 10, 422-450, 1968.

[78] Mandelbrot, B., "Intermittent turbulence in self-similar cascades: divergence of high moments and dimension of the carrier," *J. Fluid Mech.*, vol. 62, 331-350, 1974.

[79] Mandelbrot, B., *Fractals, form, chance and dimension*. San Francisco: Freeman, 1977.

[80] Mandelbrot, B., *The Fractal Geometry of Nature*. San Francisco: Freeman, 1983.

[81] Matheron, G., "Random functions and their applications in geology," in *Geostatistics*, Merriam, D.F., Ed. New York: Plenum, 1970, pp. 79-87.

[82] Matheron, G., "Splines and Kriging: their formal equivalence," in *Syracuse Universiyty Geology Contribution 8*, Merriam, D.F., Ed. Departement of geology, Syracuse university, Syracuse, NY: , 1981.

[83] Meneveau, C. and K.R. Sreenevasan, "Simple multifractal cascade model for fully develop turbulence," *Phys. Rev. Lett.*, vol. 59, no. 13, 1424-1427, 1987.

[84] Monin, A.S., *Weather forecasting as a problem in physics*. Boston Ma: MIT press, 1972.

[85] Nastrom, G.D. and K.S. Gage, "A first look at wave number spectra from GASP data," *Tellus*, vol. 35, 383, 1983.

[86] Novikov, E.A. and R. Stewart, "Intermittency of turbulence and spectrum of fluctuations in energy-disspation," *Izv. Akad. Nauk. SSSR. Ser. Geofiz.*, vol. 3, 408-412, 1964.

[87] Obukhov, A., "Structure of the temperature field in a turbulent flow," *Izv. Akad. Nauk. SSSR. Ser. Geogr. I Geofiz*, vol. 13, 55-69, 1949.

[88] Obukhov, A., "The statistically orthogonal expansion of empirical functions," *Izv. Geofiz. ser. Atm. Ocean. Phys.*, vol. 60, 280-291, 1960.

[89] Obukhov, A., "Some specific features of atmospheric turbulence," *J. Geophys. Res.*, vol. 67, 3011, 1962.

[90] Olsson, J., J. Niemczynowicz, R. Berndtsson, and M. Larson, "Fractal properties of rainfall," *Annales Geophys.*, vol. special issue, 142, 1990.

[91] Paladin, G. and A. Vulpiani, "Anomalous scaling laws in multifractal objects," *Phys. reports*, vol. 156, 147-225, 1987.

[92] Panofsky, H., "Objective weather-map analysis," *J. Appl. Meteor.*, vol. 6, 386-392, 1949.

[93] Papoulis, A., *Probability, Random Variables and Stochastic Processes*. New York: McGraw Hill, 1965.

[94] Parisi, G. and U. Frisch, "A multifractal model of intermittency," in *Turbulence and predictability in geophysical fluid dynamics and climate dynamics*, Ghil, M., R. Benzi, and G. Parisi, Eds. North Holland, 1985, pp. 84-88.

[95] Paulhus, J.L.H., "Indian ocean and Taiwan rainfall set new records," *Monthly Weather Rev.*, vol. 93, 331-335, 1965.

[96] Pflug, K., S. Lovejoy, and D. Schertzer, "Generalized Scale Invariance, differential rotation and cloud texture," in *Nonlinar dynamics of Structures*, Sagdeev, R.Z., U. Frisch, A.S. Moiseev, and A. Erokhin, Eds. World Scientific, 1991, pp. 72-78.

[97] Pflug, K., S. Lovejoy, and D. Schertzer, "Generalized Scale Invariance, differential rotation and cloud texture," *J. Atmos. Sci.*, vol. 50, 538-553, 1993.

[98] Press, W.H., B.P. Flannery, S.A. Teukolsky, and W.T. Vetterling, *Numerical Recipes. The art of scientufic computing*. Cambridge University Press, 1986.

[99] Raudkivi, A.J., *Hydrology*. Oxford New York: Pergamon press, 1979.

[100] Remenieras, G., *L'hydrologie de l'ingenieur*. Paris: Eyrolles, 1976.

[101] Rhys, F.S. and A. Waldvogel, "Fractal shape of hail clouds," *Phys. Rev. Lett.*, vol. 56, 784-787, 1986.

[102] Ricardo, O.O., "Optimal contour mapping using universal Kriging," *J. Geophys. Res.*, vol. 79, 695-702, 1974.

[103] Richardson, L.F., *Weather prediction by numerical process*. Cambridge Univ. press (Republished by Dover, New York, 1965), 1922.

[104] Rodriguez-Iturbe, I., B.F.D. Power, and J.B. Valdés, "Chaos in rainfall," *Wat. Resour. Res.*, vol. 25, 1667-1675, 1989.

[105] Schertzer, D. and S. Lovejoy, "Elliptical turbulence in the atmosphere," in *proceedings of the forth symposium on turbulent shear flows 11.1-11.8*, Karlshule, West Germany, 1983.

[106] Schertzer, D. and S. Lovejoy, "On the Dimension of Atmospheric motions," in *Turbulence and Chaotic phenomena in Fluids, IUTAM*, Tatsumi, T., Ed. Elsevier Science Publishers B. V., 1984, pp. 505-512.

[107] Schertzer, D. and S. Lovejoy, "Generalized Scale Invariance, differential rotation and cloud texture," in *Turbulent Shear Flow 4*, Launder, B., Ed. Springer-Verlag, 1985, pp. 7-33.

[108] Schertzer, D. and S. Lovejoy, "Generalised scale invariance in turbulent phenomena," *Physico-Chemical Hydrodynamics Journal*, vol. 6, 623-635, 1985.

[109] Schertzer, D. and S. Lovejoy, "Physical modeling and Analysis of Rain and Clouds by Anysotropic Scaling of Multiplicative Processes," *J. Geophys. Res. D*, vol. 92, no. 8, 9693-9714, 1987.

[110] Schertzer, D. and S. Lovejoy, "Singularités anysotrope, divergence des moments en turbulence," *Ann Sc. math. du Québec*, vol. 11, no. 1, 139-181, 1987.

[111] Schertzer, D. and S. Lovejoy, "Meeting Reports: Scaling, Fractals and Nonlinear Variability in Geophysics," *Eos*, vol. 69, no. 10, 143-145, 1988.

[112] Schertzer, D., S. Lovejoy, R. Visvanathan, D. Lavalée, and J. Wilson, "Multifractal analysis techniques and rain and cloud fields," in *Fractal Aspects of Materials: Disordered Systems*, Weitz, D.A., L.M. Sander, and B.B. Mandelbrot, Eds. Materials Research Society, 1988, pp. 267-270.

[113] Schertzer, D. and S. Lovejoy, "Generalized Scale Invariance and multiplicative processes in the atmosphere," *Pageoph*, vol. 130, 57-81, 1989.

[114] Schertzer, D. and S. Lovejoy, "Nonlinear variability in geophysics: multifractal analysis and simulation," in *Fractals: Physical Origin and Consequences*, Pietronero, L., Ed. New-York: Plenum, 1989, pp. 49.

[115] Schertzer, D. and S. Lovejoy, "Nonlinear geodynamical variability: multiple singularities, universality and observables," in *Non-linear variability in geophysics: Scaling and Fratals*, Schertzer, D. and S. Lovejoy, Eds. Kluwer, 1991, pp. 41-82.

[116] Schertzer, D., S. Lovejoy, D. Lavallée, and F. Schmitt, "Universal hard multifractal turbulence: theory and observation," in *Nonlinar dynamics of Structures*, Sagdeev, R.Z., U. Frisch, A.S. Moiseev, and A. Erokhin, Eds. World Scientific, 1991, pp. 213-235.

[117] Schertzer, D., S. Lovejoy, and D. Lavallée, "First and Second Order Phase Transitions in Multifractal Processes," *submitted to Phys. Rev. Lett.*, .

[118] Schertzer, D. and S. Lovejoy, "From scalar to Lie cascades: joint multifractal analysis of rain and clouds processes," in *Space/Time Variability and Interdependance of Hydrological Processes*, Feddes, R.A., Ed. Cambridge University Press, 1993, pp. in press.

[119] Schmitt, F., S. Lovejoy, D. Schertzer, D. Lavallée, and C. Hooge, "First estimates of multifractal indices for velocity and temperature fields," *C. R. Acad. Sci. de Paris, Serie II*, vol. 314, 749-754, 1992.

[120] Schmitt, F., D.L.D. Schertzer, and S. Lovejoy, "Empirical Determination of Universal Multifractal Exponents in Turbulent Velocity Fields," *Phys. Rev. Lett.*, vol. 68, 305-308, 1992.

[121] Schmitt, F. and P. Ladoy, "Double Trace Moment Analysis of Nîmes Raifall," 1992, Private communication.

[122] Schuster, H.G., *Deterministic Chaos 2 rev. ed.*. New York: VCH, 1988.

[123] Seed, A., "Statistical problems in measuring convective rainfall," Ph.D. thesis, McGill University, Montréal (Québec), Canada, 1989.

[124] Segal, B., "High-Intensity rainfall statistics for Canada," Tech. Rep., , Ottawa (Ontario), Canada, , CRC 1329-E, 1979.

[125] Sen, Z., A.S. Bazuhair, and A.A. Gohani, "Fractal description of rainy and non rainy months in Saudi Arabia," *submitted to Atmos. Res.*, .

[126] *Systat users manual*, Systat inc., Evanston, Il., U.S.A., 1989.

[127] Tél, T., "," *Naturforsch*, vol. 43a, 1154-1174, 1988.

[128] Taylor, G.I., "The spectrum of turbulence," *Proc. Roy. Soc. A*, vol. 164, no. 919, 476-490, 1938.

[129] Tessier, Y., S. Lovejoy, and D. Schertzer, "Universal Multifractals: theory and observations for rain and clouds," *J. Appl. Meteor.*, vol. 32, no. 2, 223-250, 1992.

[130] Tessier, Y., S. Lovejoy, and D. Schertzer, "Universal Multifractal Indices For The Ocean Surface At Far Red Wavelengths," *Geophys. Res. Lett.*, vol. in press, .

[131] Thiébaux, H.J. and M.A. Pedder, *Spatial Objective Analysis with applications in atmospheric science*. Academic Press, 1987.

[132] Thiessen, A.H., "Precipitation averages for large areas," *Mon. Wea. Rev.*, vol. 39, 1082-1084, 1911.

[133] Vinnichenko, N.K., "The kinetic energy spectrum in the free atmosphere for 1 second to 5 years," *Tellus*, vol. 22, 158, 1969.

[134] Wahba, G., "Smoothing noisy data with spline functions," *Numer. Math.*, vol. 24, 383-393, 1975.

[135] Waymire, E., "Scaling limits and self-similarity in precipitation fields," *Wat. Resour. Res.*, vol. 21, 1271-1281, 1985.

[136] Welch, R.M., K.S. Kuo, B.A. Wielicki, S.K. Sengupta, and L. Parker, "Marine stratocumulus cloud fields off the coast of Southern California observed by LANDSAT imagery, part I: Structural characteristics," *J. Appl. Meteor.*, vol. 27, 341-362, 1988.

[137] Wilson, J., S. Lovejoy, and D. Schertzer, "An intermittent wave packet model of rain and clouds," in *2nd conf. on satellite meteor. and remote sensing*, AMS Boston, 1986, pp. 233-236.

[138] Wilson, J., D. Schertzer, and S. Lovejoy, "Physically based modelling by multiplicative cascade processes," in *Non-linear variability in geophysics: Scaling and Fratals*, Schertzer, D. and S. Lovejoy, Eds. Kluwer, 1991, pp. 185-208.

[139] Yaglom, A.M., "The influence on the fluctuation in energy dissipation on the shape of turbulent characteristics in the inertial interval," *Sov. Phys. Dokl.*, vol. 2, 26-30, 1966.

[140] Yano, J.I. and Y. Takeuchi, "Fractal dimension analysis of horizontal cloud pattern in the intertropical convergence zone," in *Non-linear variability in geophysics: Scaling and Fratals*, Schertzer, D. and S. Lovejoy, Eds. Kluwer, 1991, pp. 185-208.

[141] Zawadzki, I., "Statistical properties of precipitation patterns," *J. Appl. Meteor.*, vol. 12, 469-472, 1973.

[142] Zawadzki, I., "Fractal versus correlation structure in rain," *J. Geophys. Res.*, vol. 92, 469-472, 1987.